Master Thesis

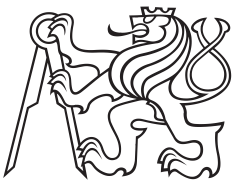

Czech
Technical
University
in Prague

F3

Faculty of Electrical Engineering
Department of Microelectronics

# Miniaturized Fluxgate Sensors

Jiří Maier

Supervisor: prof. Ing. Pavel Ripka, CSc.
Field of study: Electronics and Communications
January 2024

# MASTER‘S THESIS ASSIGNMENT

## I. Personal and study details

Student's name: **Maier Jiří** Personal ID number: **483896**

Faculty / Institute: **Faculty of Electrical Engineering**

Department / Institute: **Department of Microelectronics**

Study program: **Electronics and Communications**

Specialisation: **Electronics**

## II. Master’s thesis details

Master’s thesis title in English:

**Miniaturized Fluxgate Sensors**

Master’s thesis title in Czech:

**Miniaturní fluxgate senzor**

Guidelines:

Study literaure on fluxgate sensors. Design a fluxgate sensor with an oval core integrable on-chip. Based on simulations, optimize its sensitivity. Verify the simulation results experimentally.

Bibliography / sources:

J. Kubik, L. Pavel, and P. Ripka, “PCB racetrack fluxgate sensor with improved temperature stability,” Sensors and Actuators, A: Physical, vol. 130-131, pp. 184-188, 2006
J. Kubík: Printed Circuit Board Fluxgate Sensors, Shaker Verlag 2009
C. C. Lu, Y. C. Lin, Y. Z. Tian et al., “Hybrid Microfluxgate and Current Transformer Sensor,” IEEE Transactions on Magnetics, vol. 58, no. 8, Aug, 2022.

Name and workplace of master’s thesis supervisor:

**prof. Ing. Pavel Ripka, CSc. Department of Measurement FEE**

Name and workplace of second master’s thesis supervisor or consultant:

Date of master’s thesis assignment: **29.08.2023** Deadline for master's thesis submission: **09.01.2024**

Assignment valid until: **16.02.2025**

| prof. Ing. Pavel Ripka, CSc.<br>Supervisor’s signature | prof. Ing. Pavel Hazdra, CSc.<br>Head of department’s signature | prof. Mgr. Petr Páta, Ph.D.<br>Dean’s signature |
|---|---|---|

## III. Assignment receipt

The student acknowledges that the master’s thesis is an individual work. The student must produce his thesis without the assistance of others, with the exception of provided consultations. Within the master's thesis, the author must state the names of consultants and include a list of references.

. | Date of assignment receipt

Student’s signature

# Acknowledgements

I wrote this thesis during a double-degree study program between the Czech Technical University in Prague (CTU) and the National Taiwan University of Science and Technology in Taipei (NTUST). I want to thank my advisors from both universities, prof. Po-Ki Chen from NTUST and prof. Pavel Ripka from CTU, for their support and advice. I also thank my family for their support during my studies.

# Declaration

I declare that I elaborated this thesis on my own and that I mentioned all the information sources that have been used in accordance with the Guideline for adhering to ethical principles in the course of elaborating an academic final thesis.

In Prague, 8. January 2024

Jiří Maier

# Abstract

This thesis describes the design and fabrication of a miniaturized fluxgate sensor using CMOS technology. The fluxgate uses a "racetrack" shaped oval core made of an amorphous metal using chemical etching or laser-cutting. Solenoid coils, made using wire bonding, are used for both the excitation and sensing coils. The design uses 40 turns of excitation coil winding and 60 turns of the sensing coil. The sensor achieves an open-loop sensitivity of 4440 V/T at 1.3 MHz excitation. The optimal current for sinewave excitation is 110 mA RMS. Power dissipation at this current is approximately 340 mW. The coils heat up to around 80°C (60°C above ambient). Power consumption can be reduced using pulse excitation, which is examined in this thesis only briefly. The linear range in open-loop operation is ±200 $\mu$T with less than 0.5 % non-linearity. Noise characteristics and perming were not measured in this thesis; they will be measured and published later. The thesis also includes FEM (finite element method) simulations of fluxgate operation in order to optimize its sensitivity. Different dimensions of the racetrack core are investigated to optimize the demagnetization factor and layout of coils surrounding the core. Magnetic properties of the material used in simulations are also measured and processed as part of this thesis.

**Keywords:** fluxgate, micro-fluxgate, magnetic sensor, miniaturized fluxgate, CMOS microfluxgate

**Supervisor:** prof. Ing. Pavel Ripka, CSc.

# Abstrakt

Tato práce popisuje návrh a výrobu miniaturizovaného fluxgate senzoru s využitím technologie CMOS. Fluxgate využívá jádro oválného tvaru „racetrack“ vyrobené z amorfního kovu pomocí chemického leptání nebo laserového řezání. Budicí i snímací cívky jsou typu solenoid a jsou vytvořené s pomocí technologie wire-bonding. Finální design používá 40 závitů budicí cívky a 60 závitů snímací cívky. Sensor dosahuje citlivosti 4440 V/T při buzení 1,3 MHz. Optimální proud pro sinusové buzení je 110 mA RMS. Tepelný výkon při tomto proudu je přibližně 340 mW. Cívky se zahřívají na teplotu okolo 80°C (60°C nad teplotu okolního prostředí). Spotřebu energie lze snížit použitím pulzního buzení, to je však v této práci zkoumáno jen velmi stručně. Lineární rozsah při provozu v otevřené smyčce je ±200 $\mu$T s nelinearitou menší než 0,5 %. V této práci nebyly měřeny šumové charakteristiky; budou změřeny a publikovány později. Součástí práce jsou také simulace metodou konečných prvků (FEM) s cílem optimalizovat citlivost fluxgate sensoru. Zkoumají se různé rozměry jádra „racetrack“ s cílem optimalizovat demagnetizační činitel a uspořádání cívek obklopujících jádro. V rámci této práce jsou také změřeny magnetické vlastnosti použitého materiálu pro účely simulací.

**Klíčová slova:** fluxgate, micro-fluxgate, magnetický sensor, miniaturní fluxgate, CMOS microfluxgate

**Překlad názvu:** Miniaturní fluxgate senzor

# Contents

# Figures

# Tables

# Chapter 1

# Introduction

Fluxgate is a type of vectorial magnetic field sensor. Among other type of magnetometers, the fluxgate mainly benefits from room temperature operation, tiny zero-point drift, and significant linearity. It allows for measuring low fields down to 0.1 nT[1][2]. The applications of fluxgate sensors include electronic compasses, non-contact current probes, bioimaging, and space exploration [3][4]. Despite its advantages, the traditional fluxgate is unsuitable for miniaturized systems because of its large size and high power consumption.

## 1.1 Objectives

This project aims to develop a miniaturized fluxgate sensor on a CMOS chip. An oval shape (referred to as a "racetrack") will be used for the core, as it is expected to be superior to the dual rod type. The material for the core (amorphous metal) can be purchased as a thin sheet end wet-etched or laser-cut into the shape. The Sensor will use a 3D structure (made using bonding wires) for both sensing and excitation coils. The conceptual structure is shown in figure 1.1. Sensor operation will be simulated using FEM software and compared with measurements. The simulation model will be used to optimize the sensor's sensitivity.

The proposed design is not intended for mass production. The wire bonding of the coil is complex and would be difficult to automatize. The core etched from amorphous metal has an advantage over sputtered materials due to higher permeability. However, placing the core on top of the chip is also unsuitable for automatized production. This research aims to prove the concept of using a "racetrack" core and 3D coil structure for possible future fabrication in MEMS technology.

## 1.2 Fluxgate Sensor Structure Types

Fluxgate device is composed of a core made of soft magnetic material and two sets of coils. Fluxgate sensors can be divided by the type of core they use. One of the most common structures is the

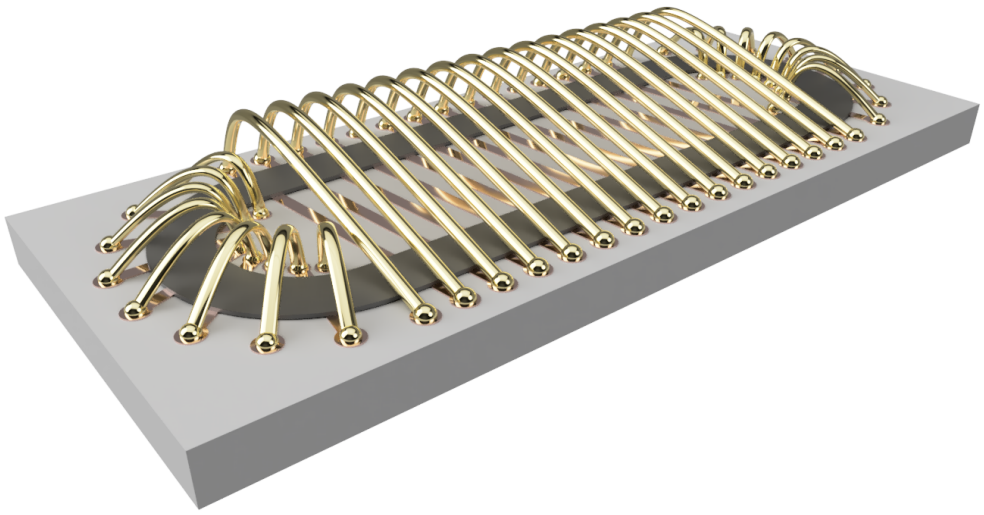

**Figure 1.1:** Micro-fluxgate design concept

Vacquier-type, depicted in figure 1.2. The oval (racetrack) shape is similar to the dual rod, with the difference that the flux is mostly contained in the material. Ring core [5] can also be used. There are also single-rod fluxgates [6], but they are rarely used due to large spurious voltage on the excitation frequency. Our sensor belongs to parallel fluxgates, as the excitation field has the same direction as the sensed field and the output field. There is also an orthogonal fluxgate[7], which is outside the scope of this work.

## 1.3 Fluxgate Sensor Working Principle

The basic structure of a fluxgate sensor is shown in figure 1.2. The core consists of two parallel segments that go through the sensing coil. Excitation coils induce magnetic flux in the core, alternating between the clockwise and counter-clockwise directions.

Flux in the top and bottom part of the core has the same magnitude but different directions, meaning that the sum of flux through the sensing coil is zero, and no voltage is induced. The excitation current must be large enough to saturate the core (the excitation is sine-wave, but flux gets "clipped" at a certain maximum value). If an external DC magnetic field is present (in the direction parallel to the core segment enclosed by the sensing coil), it causes a DC component in the flux inside the core. This means that one side will get saturated at a lower excitation current than the other.

As a result of this asymmetry, there will be a difference in flux in the two segments, creating non-zero flux in the sensing coil around zero-transition of the excitation signal, as shown in figure 1.3. These abrupt changes in flux induce a voltage in the sensing coil. This happens two times per one period of the excitation signal, meaning that the induced voltage can be observed at multiples of $2^{\text{nd}}$ harmonic of the base excitation frequency. This is useful to separate the output signal from the excitation signal that may leak into the sensing coil.

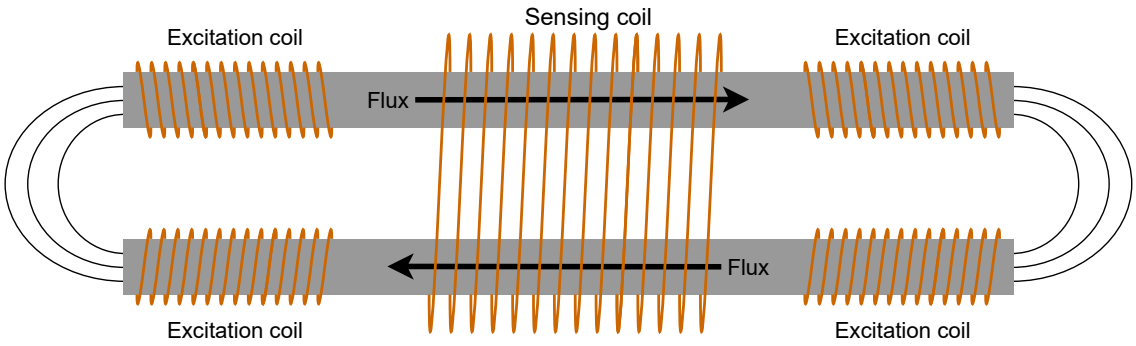


**Figure 1.2:** Dual-rod fluxgate sensor

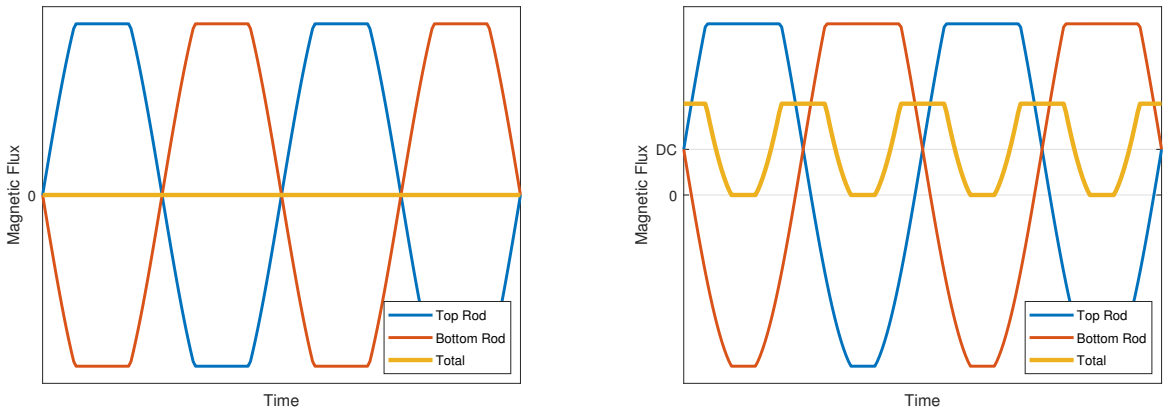


**(a) :** No external field

**(b) :** DC external field

**Figure 1.3:** Flux in the sensing coil

### 1.3.1 Mathematical description

Faraday's law of magnetic induction says that a change in magnetic flux through an open area $S$ induces an electric field along the area's boundary.

$$\oint_{\partial S} E \cdot dl = -\frac{d}{dt} \iint_{S} B \cdot dA \tag{1.1}$$

By doing the following substitutions, we get the equation 1.4, which describes voltage induced in a coil with $N$ turns when magnetic flux through the coil is changing in time.

$$V_i = \oint_{\partial S} E \cdot dl \tag{1.2}$$

$$N\frac{d\Phi(t)}{dt} = \frac{d}{dt} \iint_{S} B \cdot dA \tag{1.3}$$

$$V_i = -N\frac{d\Phi(t)}{dt} \tag{1.4}$$

The magnetic flux $\Phi$ can be rewritten using coil cross-section area $S$ and the magnitude of the magnetic field $H$ projected into the direction normal to surface $S$.

$$\Phi = \mu_r \mu_0 H S \tag{1.5}$$

Now we can write the time derivative of Induced voltage $V_i$ using time derivatives of variables:

$$V_i = -N\mu_0(\mu_r S\frac{dH}{dt} + \mu_r H\frac{dS}{dt} + SH\frac{d\mu_r}{dt}) \tag{1.6}$$

Equation 1.6 shows that voltage can be induced by three different means:

1. Changing magnetic field $H$, which is not useful for measuring DC fields.
2. Changing effective area $S$ (either physical dimensions or angle of the coil relative to H field), which is unlikely to be practical for sensor application.
3. Changing relative permeability $\mu_r$, which is exactly what we do by bringing the core into and out off saturation.

## 1.4 State of the Art

The process of miniaturizing fluxgate sensors began with PCB fluxgates. These use multilayer PCBs to form the coils; an etched core is inserted between the layers. One notable work of this kind is the dissertation thesis of Jan Kubík at CTU Prague[8][9]. In 2014, Lu [10] proposed a PCB-based "flip-chip" design with planar sensing coils.

### 1.4.1 Micro-Fluxgate Sensors

The first fluxgate sensor utilizing micromachined solenoid coils appeared in 1994 [11]. The device used a 2 mm long rod core and had 30 and 20 turns of excitation and a sensing coil, respectively. The maximum sensitivity was 5.8 V/T at 100 kHz excitation of 130 mA. In 1996, Kawahito et al. proposed Si-integrate fluxgate with an electrodeposited core made of NiFeIn alloy [12]

A new structure of integrated fluxgate was proposed by Ripka et al. in [13]. The structure consists of planar coils. Pulse excitation with a 20% duty cycle was introduced in [14] to solve problems with heat generation in the coils.

#### Hybrid Microfluxgate and Current Transformer Sensor by Prof. Lu

Professor Lu et al. designed a dual-rod micro-fluxgate sensor with 3D excitation coil structure in [15]. In 2022, they developed a hybrid current sensor, which combines a fluxgate and a current

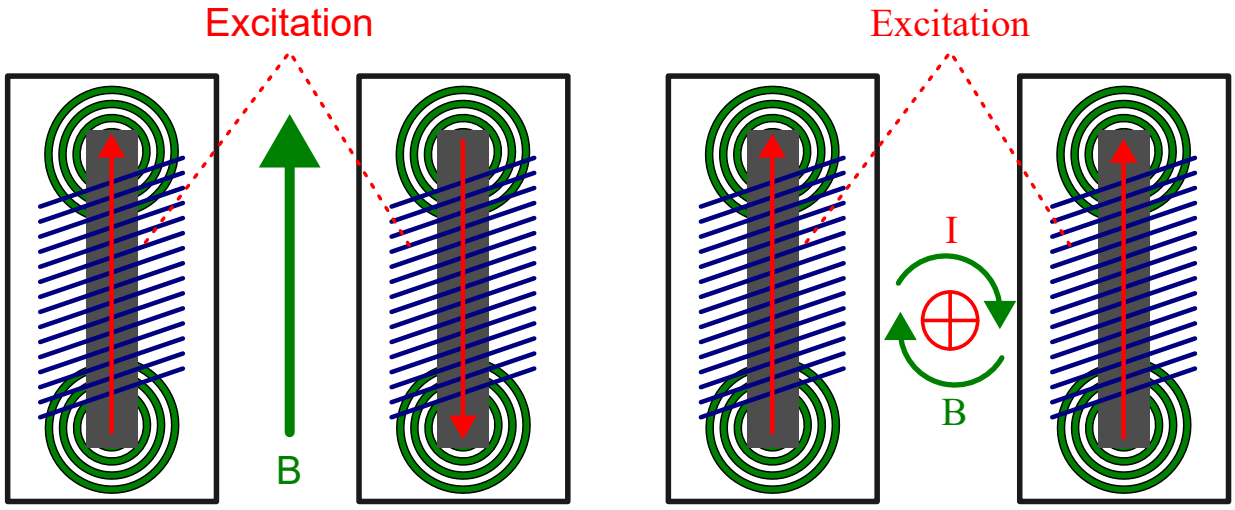


**(a) :** Magnetic Field Sensor **(b) :** Current Sensor

**Figure 1.4:** Applications of prof. Lu's hybrid micro-fluxgate sensor

transformer [16]. The chip is made using a standard Complementary Metal-Oxide Semiconductor MicroElectroMechanical Systems (CMOS-MEMS) 0.35 $\mu$m process. The top excitation coil utilizes wire-bonding (aluminum). The core is made of an amorphous magnetic-soft metal patterned using photolithography and wet etching techniques. Sensing coils are planar. The device consists of two chips, each measuring 3.5 mm × 1.75 mm. Those two chips are placed parallel or antiparallel depending on the application (magnetic field sensing or current sensing).

In the current sensing application, the sensor demonstrated a spectral current noise of 0.4 mA/$\sqrt{\text{Hz}}$ at 1 Hz and a maximum sensing range of ±10 A, boasting less than 2% non-linearity within the ±4.6 A range. It exhibited a flat bandwidth from DC to 100 kHz.

### Fully Integrated Micro-Fluxgate by Texas Instruments

Texas Instruments developed a micro-fluxgate sensor in 2015 [17]. The fluxgate inside the chip is Förster design, with two rod-cores and three interwound solenoid coils for excitation, sensing, and compensation. The device is fully integrated with the signal-processing circuitry. The feedback loop is connected internally and cannot be modified externally, which may be a limitation for certain applications. To my knowledge, this is the only commercial micro-fluxgate product.

The sensor's specifications [17] include an offset of ±8 µT (max), offset drift of ±5 nT/°C (typical), gain error of 0.04% (typical), and gain drift of ±7 ppm/°C (typical). The linearity of the sensor is ±0.1% (in closed loop), and it has a typical noise level of 1.5 nT/$\sqrt{\text{Hz}}$. The datasheet specifications were verified in [18]. This article points out a problem with offset stability in 10 %–20 % of tested devices. Applications of the DRV425 sensor for current sensing are examined in [19] and [20]. Open-loop parameters are difficult to find, as the fluxgate element is not directly accessible. Article [21] mentions open-loop gain 250 V/T and excitation frequency 500 kHz.

### MEMS micro-fluxgate by Lei Guo and Chong Lei

Article [22] reports a micro-fluxgate sensor based on a double-layer magnetic core of a Fe–Co–B-based amorphous ribbon. The sensor was fabricated using MEMS technology combined with wet etching. The sensor has a sensitivity of 1985 V/T, a linear range of ±1 mT, and a perming error below 0.4 µT. The optimal excitation current is 70 mA at 500 kHz frequency. Another article by Chong Lei [23] shows a dual-axis version of a micro-fluxgate using planar coils.

### MEMS micro-fluxgate by Jian Lei

Article [24] presents a few variants of MEMS-base micro-fluxgate. Those designs are compared at 100 kHz excitation. The sensitivity ranges from 140 V/T to 380 V/T, and the linear range is 300 $\mu$T to 700 $\mu$T. Power consumption is 34 mW to 73 mW.

## 1.4.2 Commonly Used Structures

Figure 1.5 shows three commonly used structures of fluxgate sensors. Vacquier and Förster are most suitable for macro-sized devices with wire-wound coils. The excitation and sensing coils are both solenoids. In the case of Förster, the sensing coil is physically split into two halves connected in series. The behavior is then the same as in the case of Vacquier.

The planar sensing coil is popular in miniaturized versions (for example [16]). The planar coil is much easier to integrate than a solenoid coil. The disadvantage is that only a small portion of the magnetic flux goes through the sensing coils. This results in much lower sensitivity compared to the solenoid coil.

The cores used can be split into two categories. Open cores (dual-rod), where the excitation field closes through the air. And closed cores (ring, racetrack), where the field is fully contained inside the core. The air gap in open-cores results in a higher current needed for proper saturation. It also causes higher magnetic field leakage, which can interfere with surrounding devices.

**(a) :** Vacquier **(b) :** Förster **(c) :** Planar sensing coil

**Figure 1.5:** Common structures of fluxgate sensors

# Chapter 2

# Design of Micro-Fluxgate Version 1

The device consists of a racetrack-shaped core surrounded by coils. Coils consist of a lower part, made in the topmost layer of a CMOS chip, and an upper part, made using bonding wires. The excitation coil is placed along the rounded ends of the core, while the sensing coil spans along the straight part. This is visualized in figures 1.1 (page 2) and 2.1.

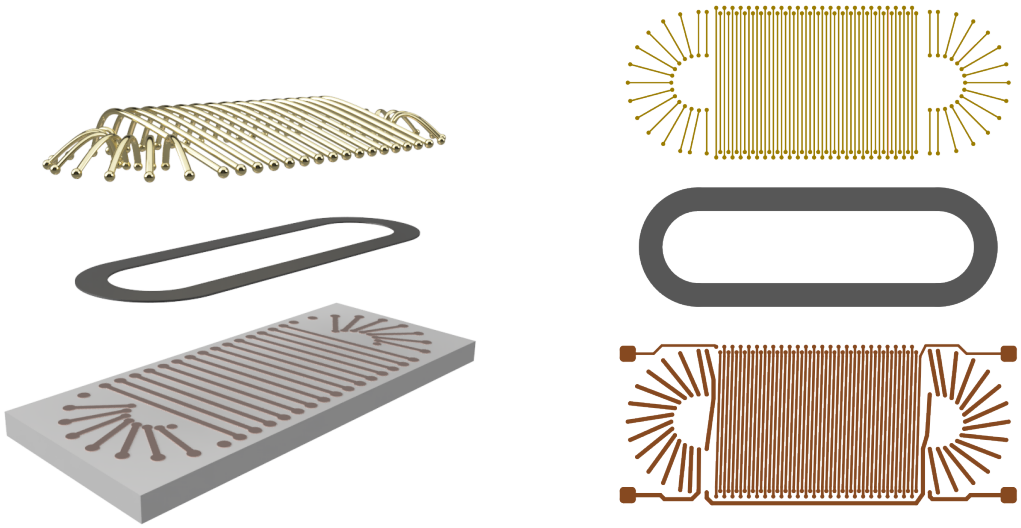

**(a) :** 3D visualization **(b) :** Layout of the first version

**Figure 2.1:** Micro-fluxgate assembly components

## 2.1 Core Used for the First Version of Micro-Fluxgate

The first design is based on a scaled-down version of the core that was used in the past for PCB-based fluxgate sensors. The macro-sized core can be used to assemble an upscaled model micro-fluxgate's structure, which can be used to verify simulation results. The dimensions of that core are (meaning

of the parameters is shown in figure 2.2):

$$l = 30 \text{ mm}$$
$$d = 10 \text{ mm}$$
$$T = 2 \text{ mm}$$
$$thickness = 25 \ \mu\text{m}$$

The micro version of the core will be linearly scaled in all dimensions (except thickness, which is already the minimum we can achieve technologically). The scaling is selected such that it meets the following constraints:

1. Area of chip should be 25 $\text{mm}^2$
$$a \cdot b \leq 25 \text{ mm}^2$$
2. There should be at least 0.5 mm padding between core and chip outline
$$a = l + 1 \text{ mm}, b = d + 1 \text{ mm}$$
3. There should be at least 0.5 mm space inside core
$$d - 2T \geq 0.5 \text{ mm}$$

Using those constraints, we can describe scaling factor $x$ by the following equation:

$$(30x + 1) \cdot (10x + 1) = 25 \implies 300x^2 + 40x - 24 = 0 \tag{2.1}$$

This quadratic equation has roots 0.22 and $-0.36$. Therefore, the scaling factor is 0.22, and the dimensions of the proposed micro-sized core are:

$$\mathbf{l = 6.6} \text{ mm}$$
$$\mathbf{d = 2.2} \text{ mm}$$
$$\mathbf{T = 0.44} \text{ mm}$$

## 2.2 Micro-Fluxgate Sensor Chip Design

I worked on the design while I was still at Czech Technical University. The fabrication was planned in cooperation with the National Taiwan University of Science and Technology (NTUST). The university has access to various fabrication technologies by UMS and TSMC, provided by the Taiwan Semiconductor Research Institute (TSRI).

While chips are designed in specialized software like Cadence or Laker, the fluxgate chip only uses paths in the metal layer and no transistors at all. For this reason, I chose to draft the layout in KiCAD (software for PCB design). PCB design software seems to be more user-friendly for this task, which mainly involves positioning pads and routing conductor traces. Dimensions of this design are much smaller than PCBs, which KiCAD is typically used for. That caused some difficulties, but I was able to design the layout without any significant issues.

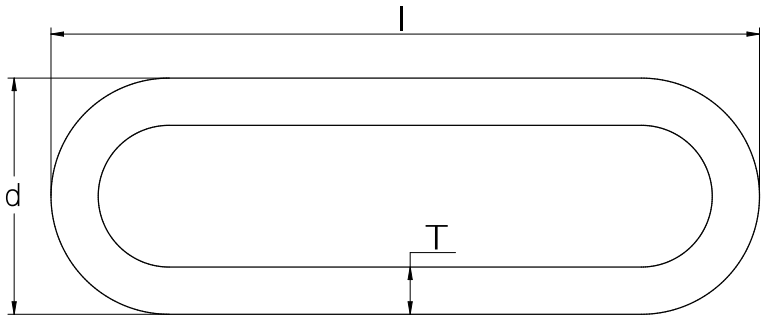


**Figure 2.2:** Racetrack dimensions

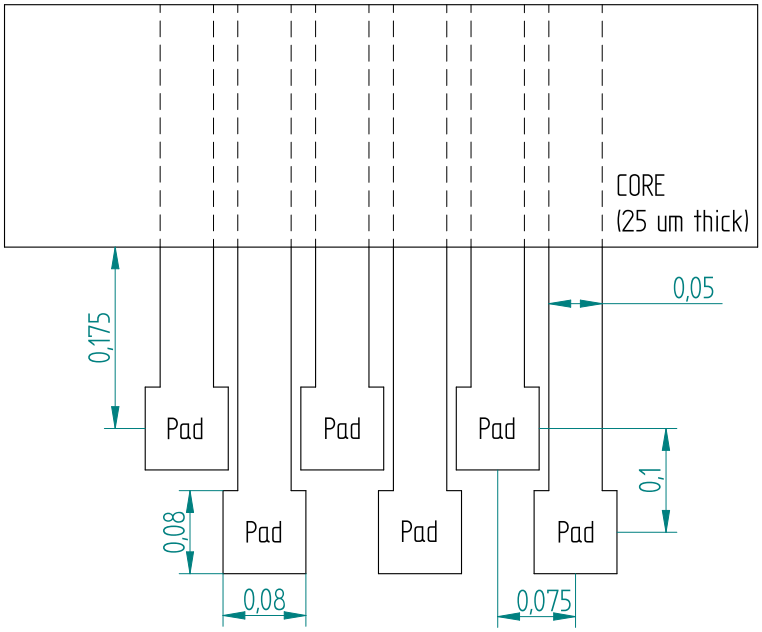


**Figure 2.3:** Bonding pads dimensions and spacing

### 2.2.1 Design Rules

The UMC 18 process has been chosen for the first version of the fluxgate chip because NTUST students use it commonly. According to process documentation, the minimum track width and spacing in the top (Metal 6) layer is 1.2 $\mu$m. The recommended size of pads for wire bonding is $80 \times 80$ $\mu$m. The spacing of the pads is supposedly not a big concern, as the bonding wires are very thin, and the width of the pads will provide enough clearance. A two-row layout of pads is used for the sensing coil, as shown in figure 2.3. The excitation coil has higher clearances, especially along the outer side.

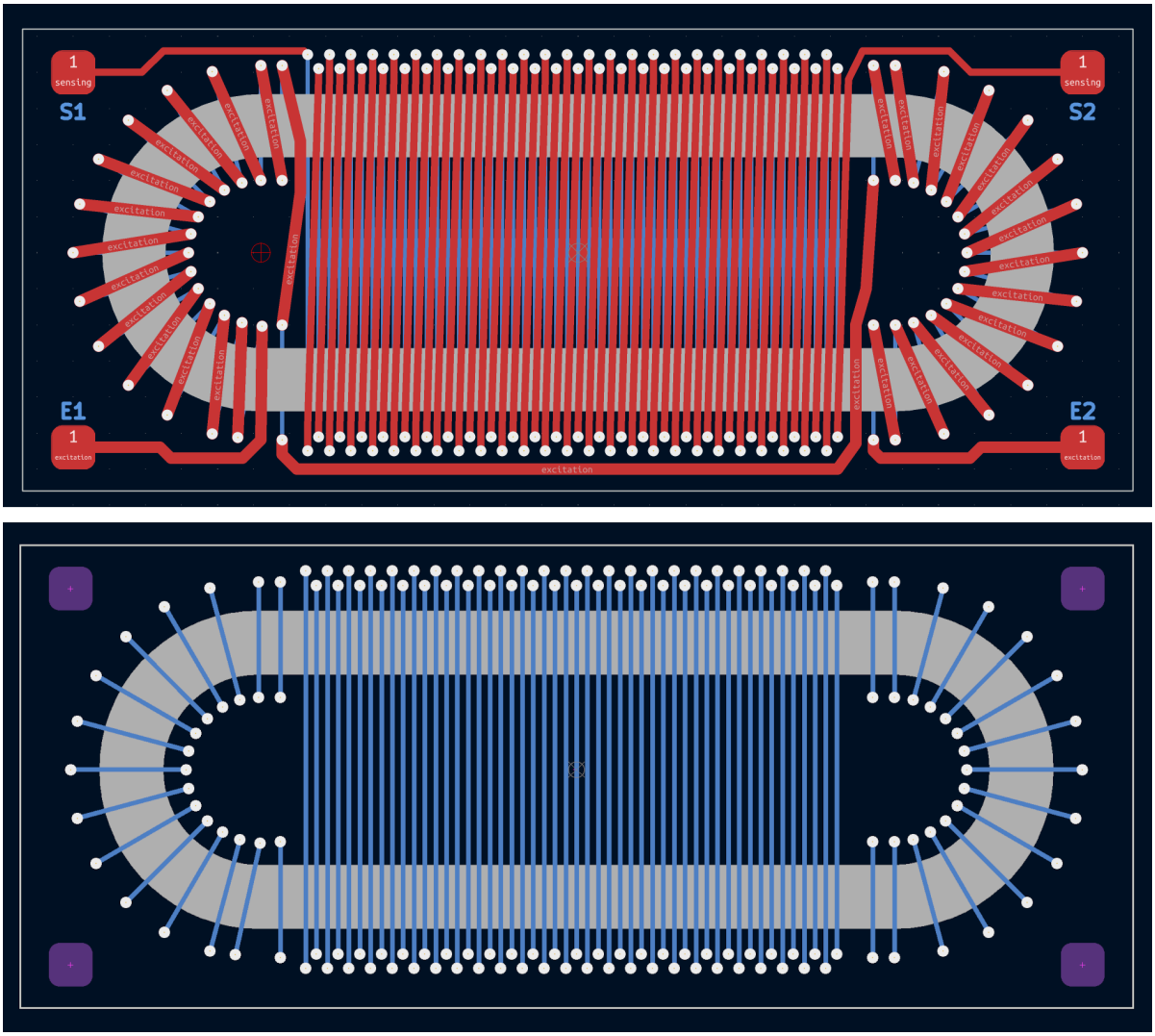


**Figure 2.4:** First version of layout

## 2.3 Layout of the First Micro-Fluxgate Version

Figure 2.4 shows the layout of the first version of the chip. The red color (top image) represents the M6 metal layer, and the blue color (bottom image) is the wire bonding.

There are 50 turns of the sensing coil and 30 turns of the excitation coil (15 at each end). The excitation coil is positioned only along the round ends of the racetrack. This is not typical (in the case of the PCB fluxgates in [8], a significant part of the excitation coil is placed on the straight segments). However, this layout is most efficient in terms of the number of turns of the sensing coil. Only the topmost metal (M6) is used for the connections, as it is significantly thicker than other metal layers (20.6 kÅ vs 5.8 kÅ). Bonding pads are $80 \times 80\mu$m squares. The coils are accessed using the pads in the corners (S1 S2 for sensing, E1 E2 for excitation).

# Chapter 3

# Demagnetization Factor of the Racetrack Core

The demagnetization factor of the core is important for the sensitivity of the sensor. A higher demagnetization factor means a lower sensitivity. We expect that the factor will remain constant for uniformly downscaled core. However, when the thickness of the core stays fixed at a value of 25 $\mu$m (which is the minimum thickness of the material we can use), the demagnetization factor will increase. The main purpose of this chapter is to get insight into how much the factor increases (linearly or more) and to develop a simulation model that can be later used to optimize the core for next version of micro-fluxgate.

## 3.1 Simulation Setup

To determine the demagnetization factor of the core, FEM simulation software Ansys Electronics Maxwell 3D[25] was used. The software allows creating a parametrized model and then varying its dimensions in parametric simulation. This is useful for optimization tasks and for finding trends in physical behavior.

### 3.1.1 Bounding Region

Apart from the modeled object itself, the simulation also needs boundary conditions (known field values at some distance from the simulated model). The boundaries define the DC magnetic field in which the object is placed by having a tangential field vector assigned to them. When creating the bounding box, we have to avoid these edge conditions:

- Too small boundary region will influence the field in simulated objects too much, leading to incorrect results
- Too big boundary region will lead to either an extremely high computational workload (in case of fine mesh in the whole region) or meshing errors when using adaptive meshing.

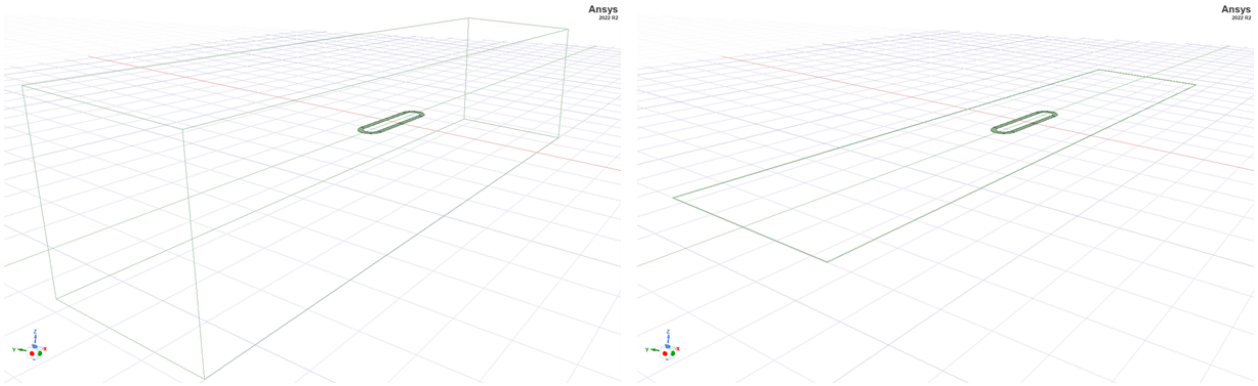

**(a) :** Height same as width **(b) :** Height in the same ratio to model thickness

**Figure 3.1:** Boundary region

### 3.1.2 Influence of Boundary Region Size on Simulation Results

Intuition suggests that the boundary region should be about 5 to 10 times larger than the model. Parametric simulation with different ratios of region size to model size was done to ensure the assumption was correct.

Our core also brings another problem: the Z size (thickness) is orders of magnitude lower than the sizes in XY directions. If the bounding region ratio is the same in all directions, it is very flat. Simulation of varying bounding box sizes was done for two different styles of the bounding box, as shown in figure 3.1:

- Region size equal to some multiple of model size in all directions
- Region size equal to some multiple of model size in X and Y directions, but Z direction equal to the Y direction

Results are shown in figure 3.2. While the "uniform proportions" (3.2a) case is giving steady results for multiples higher than about 5, the "thin" (3.2b) version is obviously useless. Simulations for higher ratios were also done. However, warnings regarding mesh problems occurred frequently for values above 100. It is also worth noting that the simulation of the "thin" case took a very long time, as it had trouble converging. For more strict convergence criteria, it may not have converged at all.

#### Conclusions of Boundary Conditions Setup

These experiments led to the following conclusions:

- Height of bounding region must be comparable to size in other directions.
- It is enough to have a box about 10 to 20 times larger than the model.

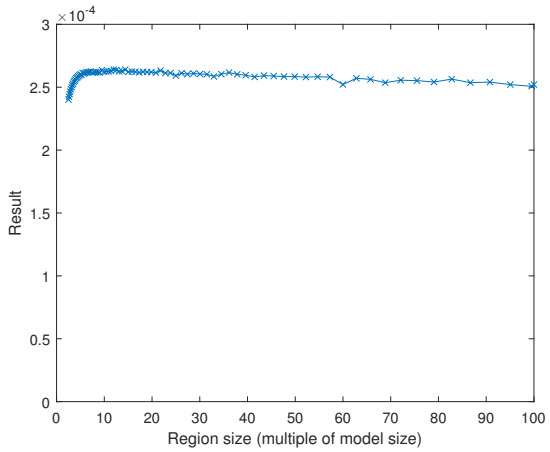


**(a) :** Height same as width

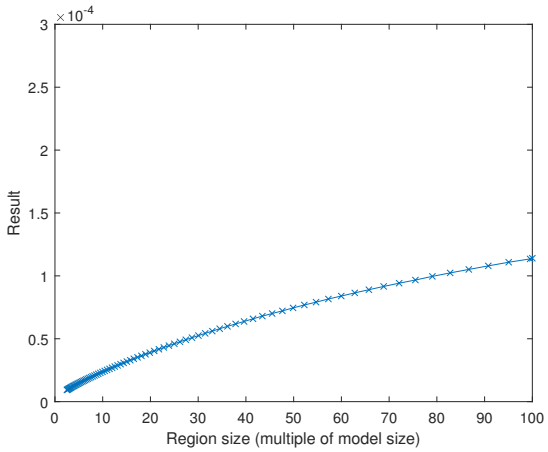


**(b) :** Height in the same ratio to model thickness

**Figure 3.2:** Change of result depending on bounding region size

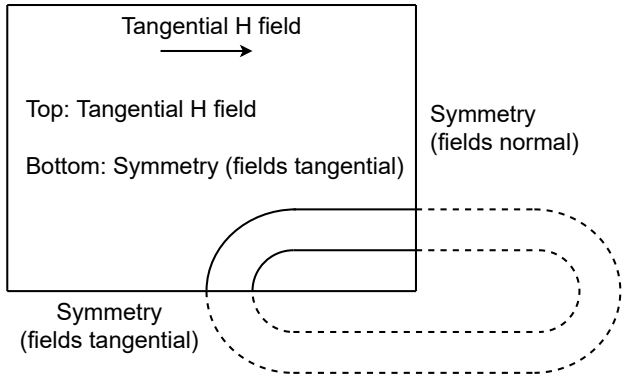


**(a) :** Boundary conditions setup

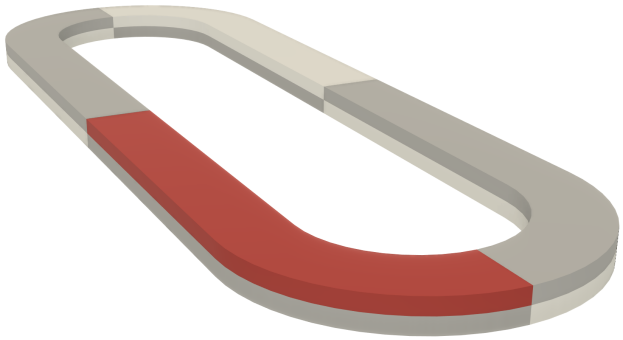

**(b) :** Basic part of the shape

**Figure 3.3:** Symmetry of racetrack core model

### 3.1.3 Model Symmetry

The racetrack shape has three planes of symmetry and thus can be split into eight parts. This can reduce simulation time to 1/8. The setup of boundary conditions to exploit the symmetry is shown in figure 3.3. The setup was verified by comparing it with the results of a setup that did not use symmetry. They matched exactly.

## 3.2 Calculating Demagnetization Factor

Formulas provided in the paper by Kubík[8] were used to calculate the demagnetization factor. There are two possible ways of calculation. The first one is better suited for computer simulation, as it avoids unnecessary computations. The second one is analogous to a way of physical measurement. Both approaches were compared to ensure that they led to the same results.

### 3.2.1 Computation of the Demagnetization Factor using Simulated Fields

Following equation comes from [8]:

$$D_{avg} = \frac{H_{C_{avg}} - H_{ext}}{H_{C_{avg}} - \frac{B_{C_{avg}}}{\mu_0}} \tag{3.1}$$

$H_{C_{avg}}$ and $B_{C_{avg}}$ are mean magnitudes of fields inside core's volume. $H_{ext}$ is the external field given by boundary condition (which should not affect the result and so can be arbitrary, 1000 A/m in following simulations). $\mu_0$ is a well known constant equal to $4\pi \cdot 10^{-7}$ H/m.

### 3.2.2 Alternative Method of Computing Demagnetization Factor

The demagnetization factor can be calculated using apparent permeability $\mu_A$.

$$D = \frac{\frac{\mu_r}{\mu_A} - 1}{\mu_r - 1} \tag{3.2}$$

Apparent permeability can be measured by comparing the inductance of a coil with the core inserted and not inserted (air core).

$$\mu_A = \frac{L_{core} - L_{air}}{L_{air}} \frac{A_{coil}}{A_{core}} + 1 \tag{3.3}$$

As $L_{air}$ is expected to be orders of magnitude smaller than $L_{core}$, this can be simplified to

$$\mu_A = \frac{L_{core}}{L_{air}} \frac{A_{coil}}{A_{core}} \tag{3.4}$$

In the simulation, we do not have any coil or inductance. The most useful value we can get is an integral of $B$ in the volume of the core. This value itself does not have much meaning, but when it is calculated for core with actual permeability and for core with $\mu_r = 1$, the ratio is equal to $\mu_A$. The resulting formula for $D$ is as follows:

$$D = \frac{\frac{\mu_r}{\mu_A} - 1}{\mu_r - 1}, \quad \mu_A = \frac{\iiint_{core} |B(\mu = \mu_r \mu_0)| \cdot dV}{\iiint_{core} |B(\mu = \mu_0)| \cdot dV} \tag{3.5}$$

This method requires simulating twice for each size variation: once for actual $\mu_r$ and once for $\mu_r = 1$. The second simulation isn't really useful, as the only thing that has changed is the volume of the core, while fields remain the same ($B = \mu_0 H_{ext}$). In essence, the denominator is only there to account for core volume. This is solved in (3.1) by calculating the mean, which is, in fact, the same integral divided by volume.

### 3.2.3 Comparison and Verification of the Methods

The first approach seems much cleaner, while the second one seems more like a brute-force way of calculation. Further computations will use the (3.1) method. Here, the second one is also used to compare the results.

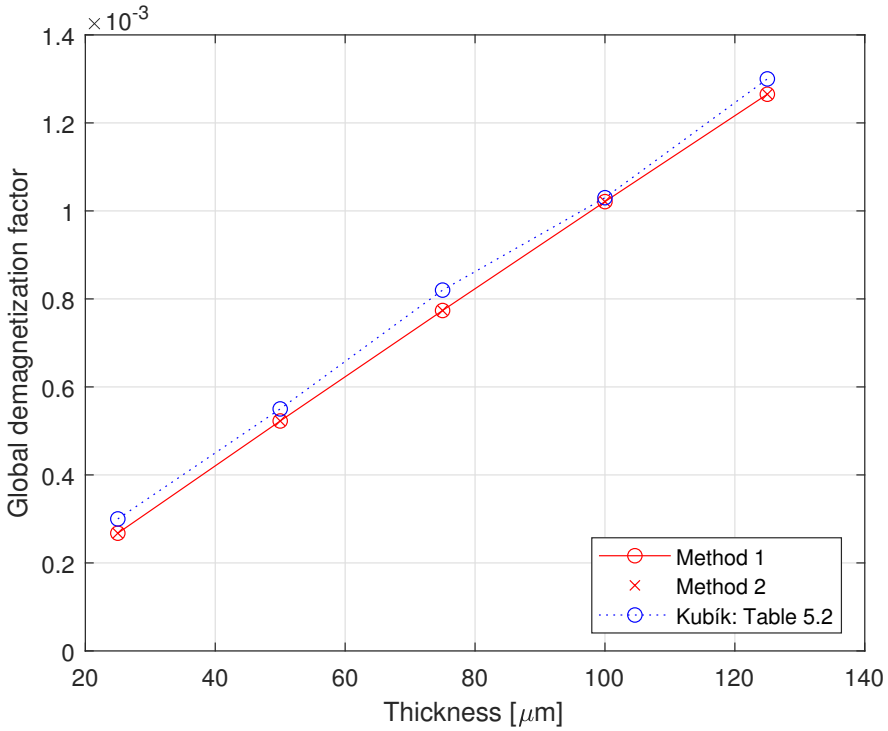


**Figure 3.4:** Comparing results of methods (3.1) and (3.5) with results from Kubík [8]

The results are also compared with those provided by Mr Kubík [8]. He published both FEM results and measurements for his core with the following dimensions

$$l = 30\text{mm}, d = 8\text{mm}, T = 1.55\text{mm}$$

for thicknesses from 25 $\mu$m to 125 $\mu$m by 25 $\mu$m step. Results are shown in figure 3.4. Results from both methods are nearly identical. There is only a 5% difference between my and Kubík's values, which confirms the correctness of my simulation setup.

### Verification Using Ring-Core

Kubík[8] also made a comparison of results for ring-shaped cores. He used measurement results provided by [26]. However, the original results are measured as local demagnetization and recalculated to global by empiric formula.

While I was able to replicate the local demagnetization factor, the global demagnetization factor that I simulated was about 25 % lower than the empirical estimation. This can be considered a limitation of the empirical formula for converting between local and global values.

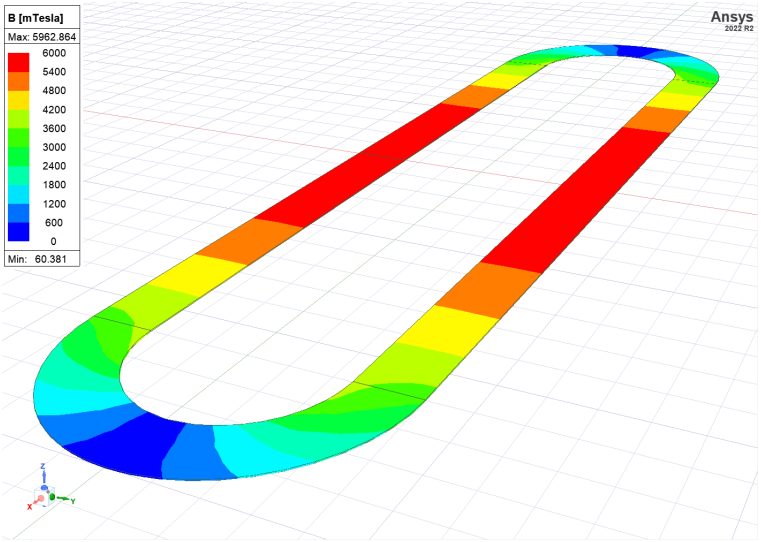


**Figure 3.5:** Visualization of magnetic flux density in racetrack core ($H_{ext} = 1000$ A/m)

### 3.2.4 Local Demagnetization Factor

So far, the demagnetization factor calculated was averaged over the whole core volume. However, the sensing coil will only be wrapped around the central (straight) part of the racetrack. It is more valuable to calculate the demagnetization only in the straight part. Computation is straightforward; use formula 3.5 but only integrate over the straight part's volume. Results are shown in figure 3.6. Local values are significantly lower than global, which is expected and positively impacts the sensor's performance.

## 3.3 Effect of Downscaling the Core on the Demagnetization Factor

Uniformly downscaling the core should have no effect on the demagnetization factor. This is implied by the fact that the demagnetization factor is a dimensionless number. I also verified it by simulation.

Scaling the core down while keeping the same thickness should have the same effect as increasing thickness while keeping other dimensions constant. Figure 3.7 shows how the demagnetization factor changes when the core is downscaled from the "Macro" size to the "Micro" size. The scaling factor is 0.22. When assuming linear dependency of demagnetization factor of thickness (as observed in figure 3.4), the demagnetization factor should increase by

$$\frac{1}{0.22} \doteq 4.5$$

and the simulated value matches this prediction. This concludes that the linear dependency holds at smaller sizes as well, and thus, there would be no extra gain from attempting to decrease the thickness. That is because decreasing the thickness would also mean decreasing the cross-sectional area by the same amount, which would decrease sensitivity to mitigate the improvement of the demagnetization factor.

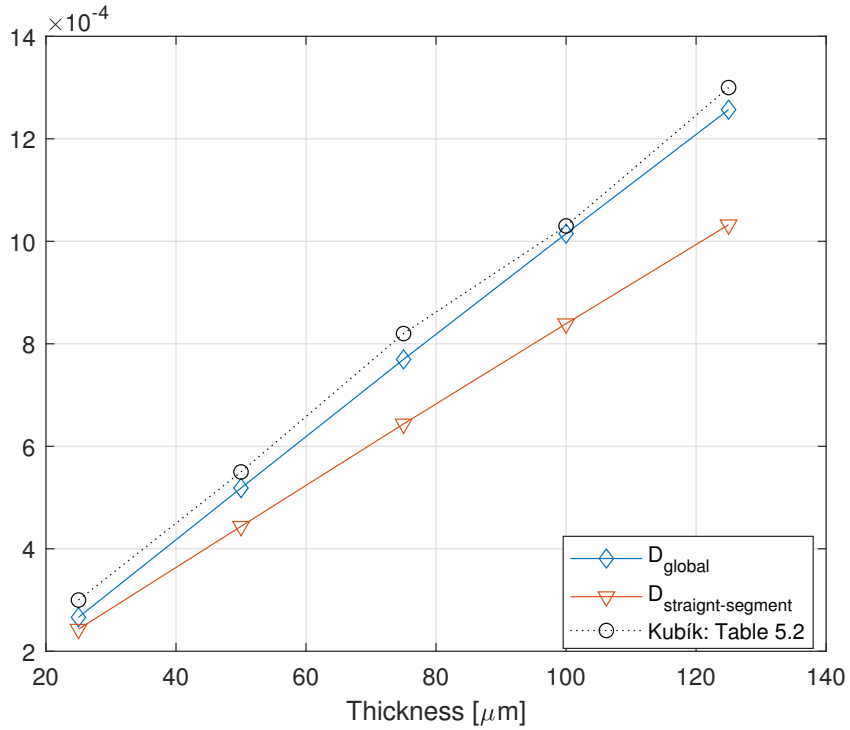


**Figure 3.6:** Local and global demagnetization factor

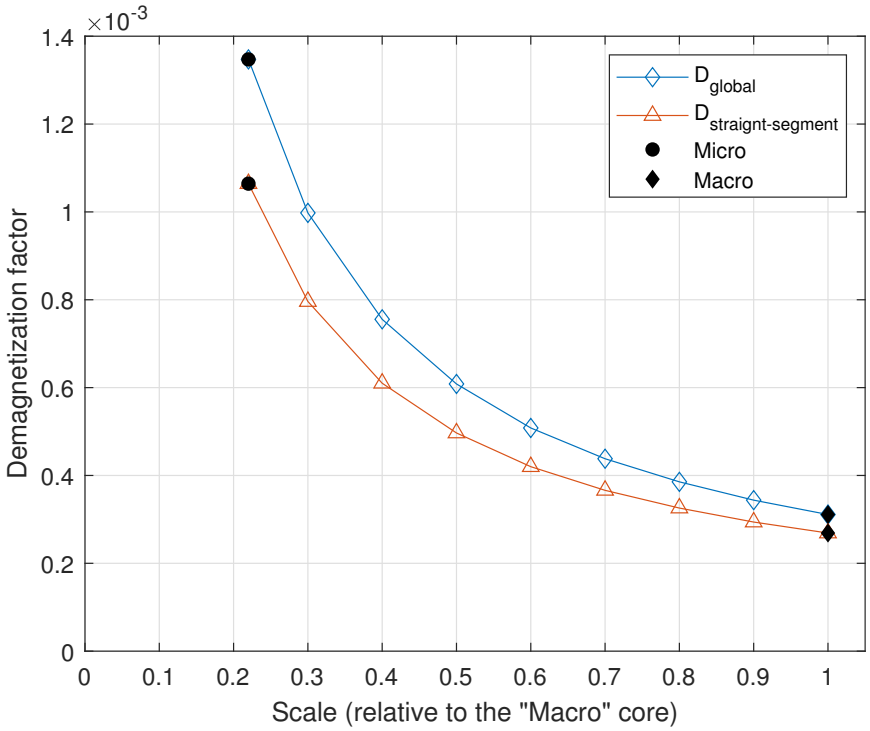


**Figure 3.7:** Effect of downscaling the core at constant thickness

# Chapter 4

# Macroscopic Model of the Micro-Fluxgate Device

An upscaled model of the micro-fluxgate device was created using a printed circuit board (PCB) instead of a chip. The core used has dimensions mentioned earlier in this work (30 mm length). Excitation coils were made by hand-soldering wires onto the PCB, which resembles the proposed micro fluxgate structure perfectly. The pickup coil is too dense to use the PCB traces for the bottom part (due to minimum width and separation). The sensing coil is thus made of a single wire winded through holes in the PCB. The model is depicted in figure 4.1

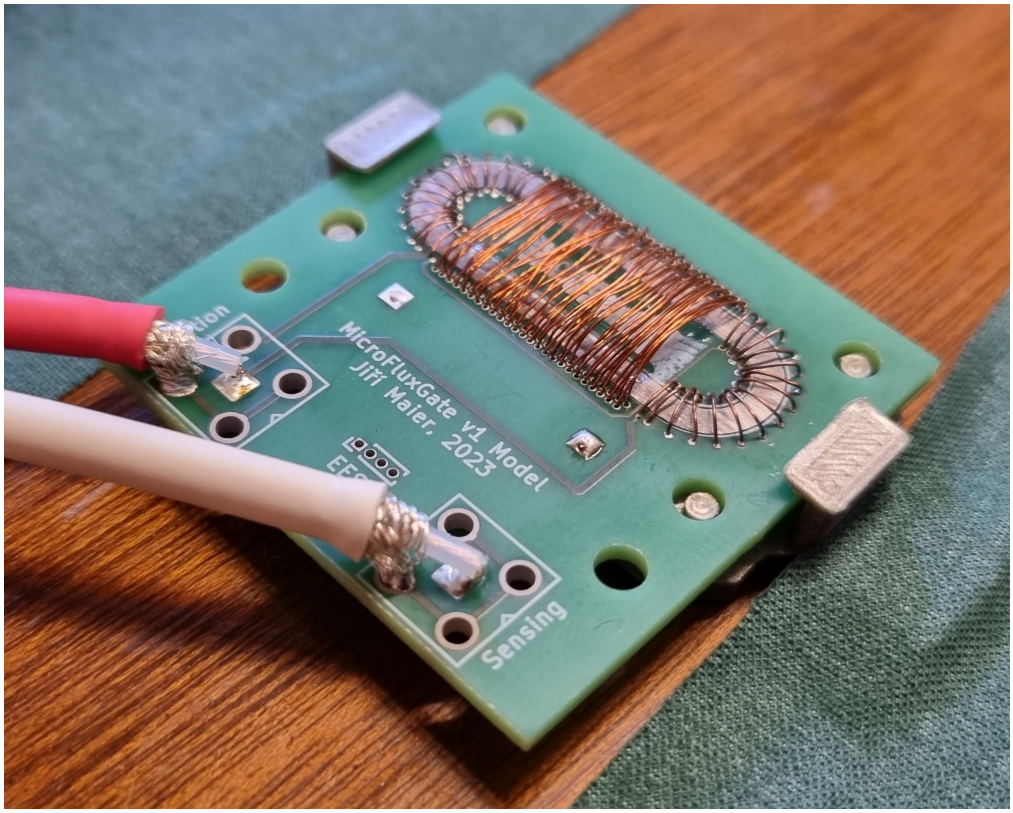


**Figure 4.1:** Upscaled model of the first version of micro fluxgate (Length 30 mm)

## 4.1 Measurement

The following characteristics of the sensor were measured and calculated:

- Induced voltage waveform at various excitation currents
- Relationship between excitation current and sensitivity

The sensor was placed inside Helmholtz coils, perpendicularly to Earth's magnetic field. The current through the Helmholtz coils was set so that the magnetic field produced by the coils is similar to the magnitude of Earth's magnetic field (Around 50 $\mu$T at the location[27]). The exact strength of the field produced by coils evaluates to 58.8 $\mu$T.

An arbitrary waveform generator was used to supply the excitation signal (sinewave). The frequency used was 100 kHz. Both channels of the generator were synchronized and connected in parallel to increase current output. However, at the maximum voltage setting, the excitation current was still not high enough (reached just slightly beneath the maximum sensitivity). An amplifier was used to get a higher current. However, the amplified signal was significantly distorted. A parallel capacitor and series inductor were placed on the amplifier's output to reduce the distortion. A 10 m long wire was used as the inductance, and a decade capacitor box was set to 170 nF by trial and error approach.

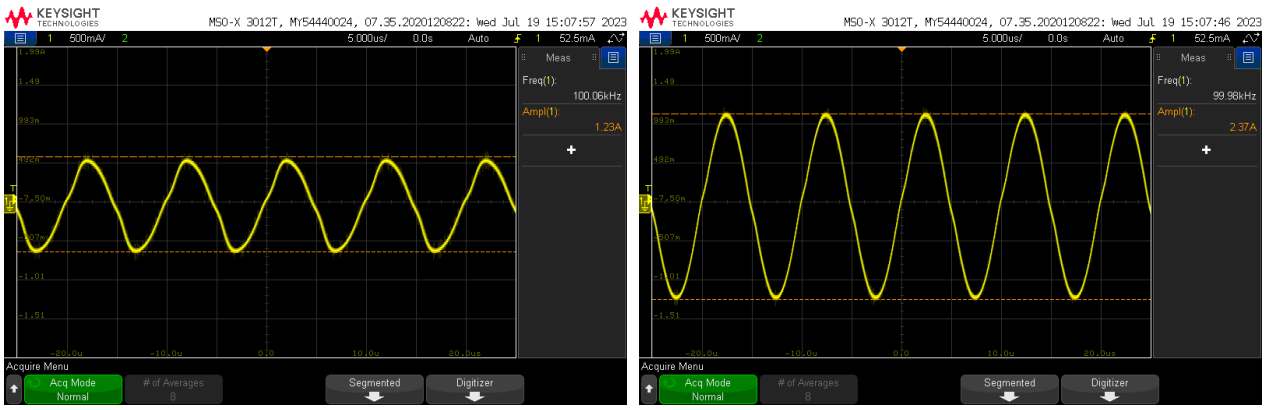


**(a) :** No filtering **(b) :** Filtered

**Figure 4.2:** Current through excitation coil, supplied by the amplifier

### 4.1.1 Sensitivity Evaluation

It can be generally stated that the useful signal is at the even harmonics of the excitation frequency. The second harmonic is typically the most sensitive. Measuring the output of a fluxgate typically involves a lock-in amplifier. However, in this measurement, only a digital oscilloscope was used. Waveforms were captured and digitally processed in Matlab.

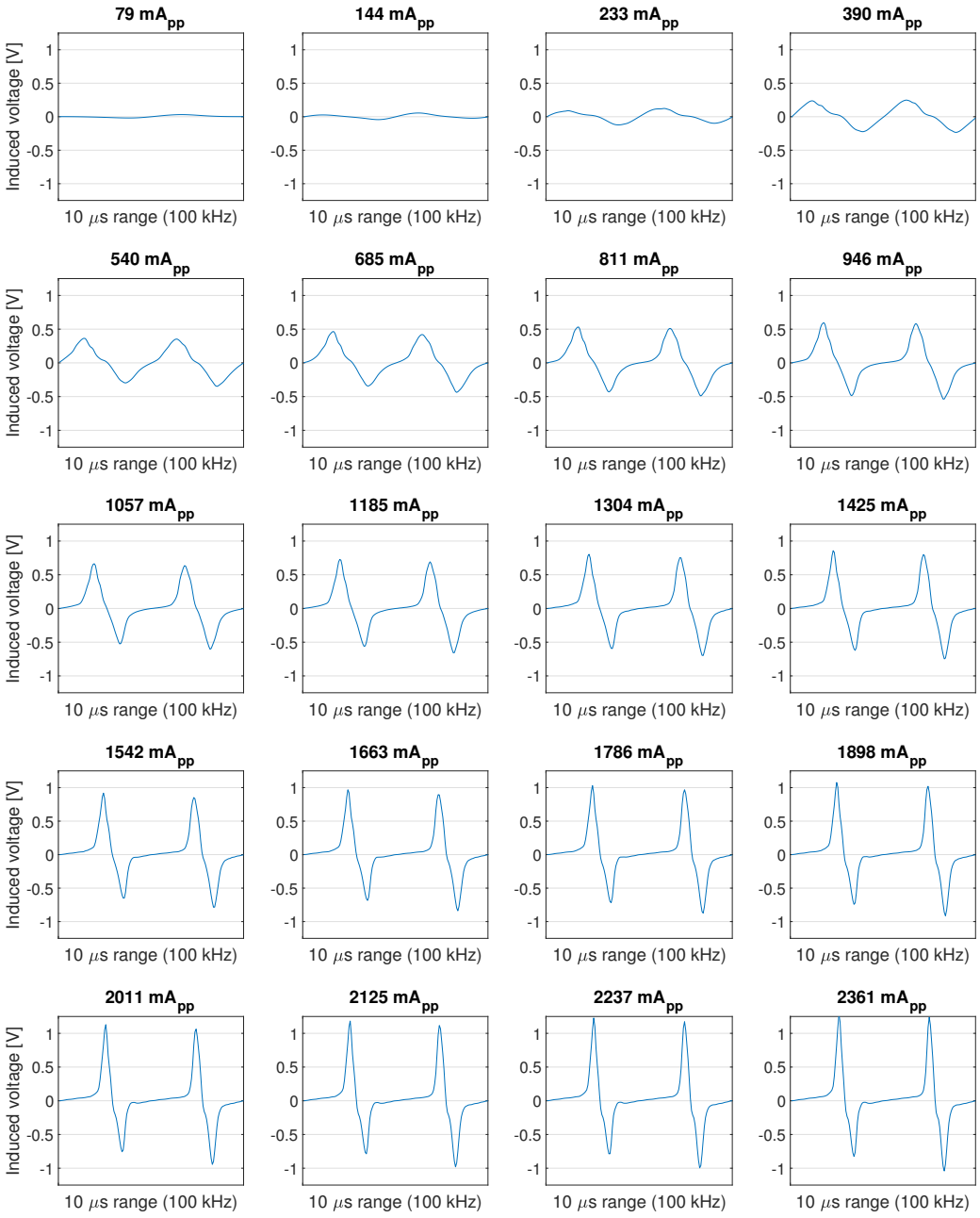


**Figure 4.3:** Measured induced voltage waveforms for various excitation currents (sinusoidal), external field 59 $\mu$T

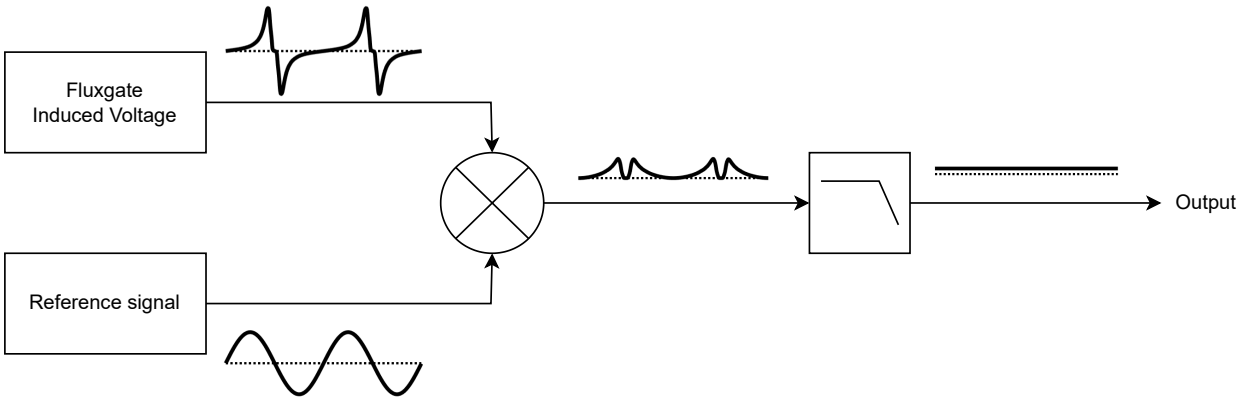


**Figure 4.4:** Processing of fluxgate output signal

## Algorithm For Processing the Output Voltage

The induced voltage signal is mixed (multiplied) with the reference signal. The reference signal has a frequency corresponding to the second harmonic of the excitation signal and amplitude 1. The phase of the reference signal is selected to maximize cross-correlation with the induced voltage signal. This shifts the spectrum so that the second harmonic is now positioned at DC. The resulting signal is then filtered by a low-pass filter (averaged) to extract the DC component.

```
fs;  % Sampling frequency
fex; % Excitation frequency
iv;  % Induced voltage waveform

% Generate reference signal (twice the excitation frequency)
tt = ((0:1:length(iv)-1)/fs)';
ref = sin(2*pi*fex*tt*2);

% Shift the reference signal to maximize cross-correlation
% with the induced voltage
[R, lags] = xcorr(iv, ref, 'biased');
[~, idx] = max(abs(R));
lag = lags(idx);
ref = circshift(ref, [lag 0]);

% Mix induced voltage with the reference signal and get DC
Vout = mean(ref .* iv);
```

## Results

There is quite a noticeable difference between results taken with and without the excitation amplifier. The maximum sensitivity for 100 kHz excitation is around, or slightly above, 3000 V/T at around 800 $mA_{pp}$ excitation current. These results will be later compared to simulation results to verify the simulation model accuracy.

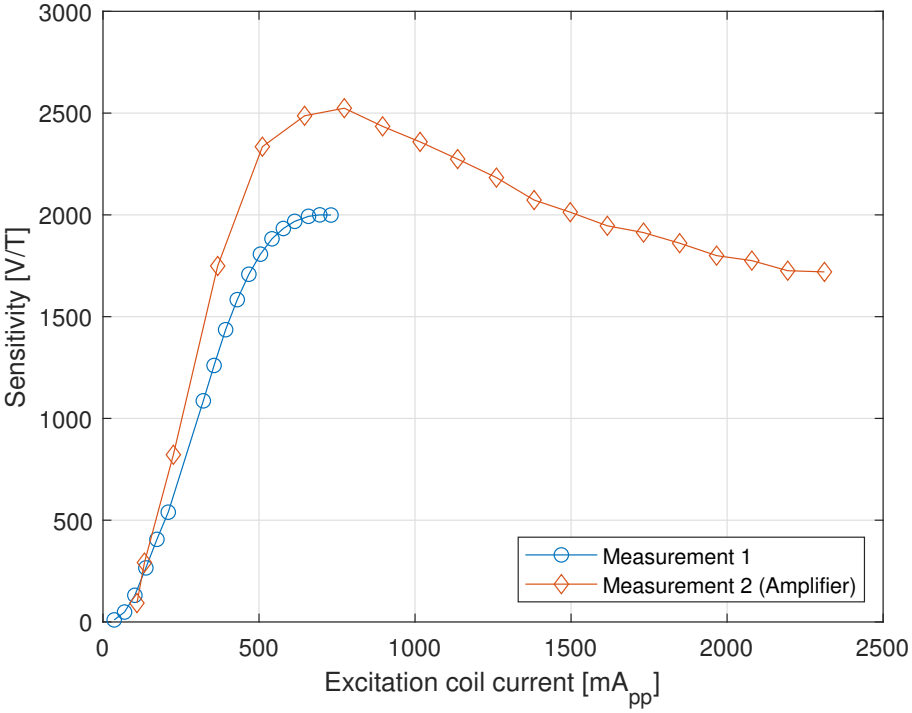


**Figure 4.5:** Measured sensitivity at 100 kHz

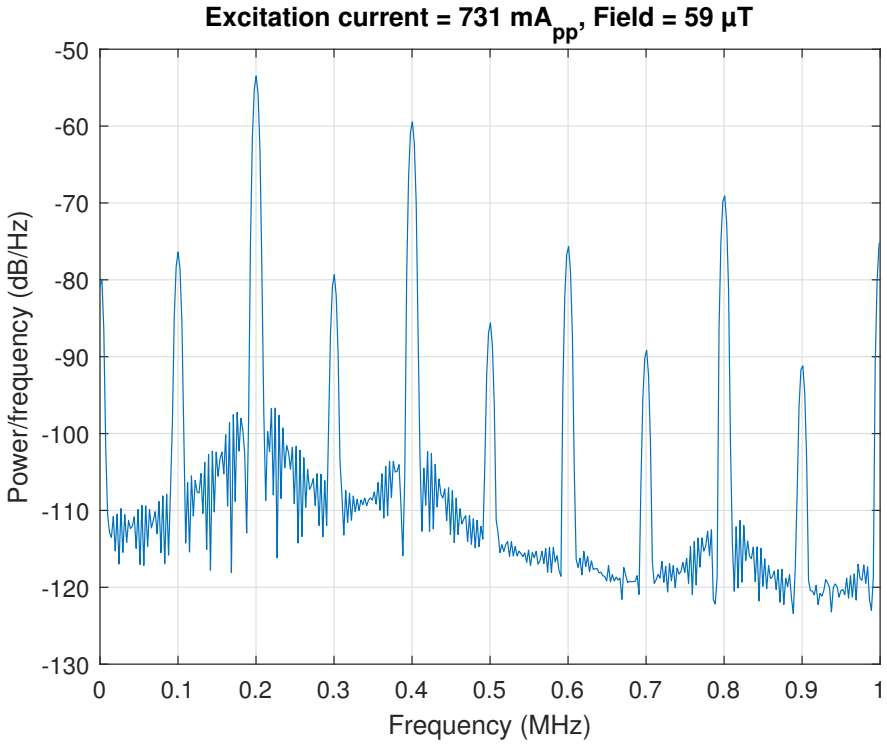


**Figure 4.6:** Spectrum of induce voltage

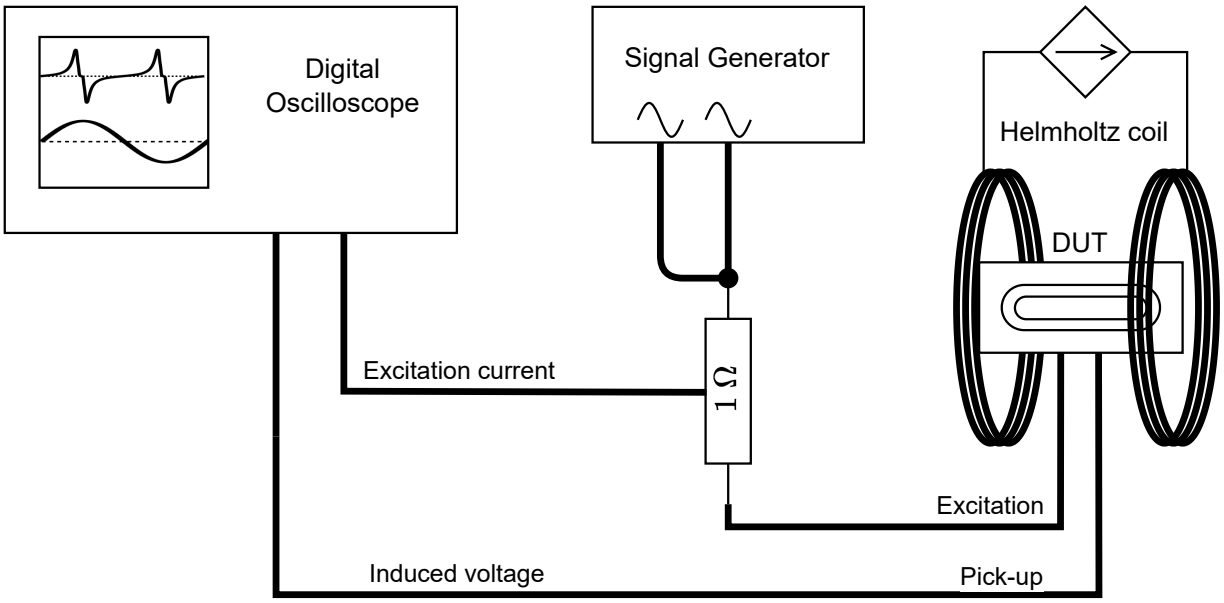


**Figure 4.7:** Setup for measuring the sensitivity of a fluxgate sensor

# Chapter 5

# Modeling Fluxgate Behavior

I began by creating a simple computational model of fluxgate behavior. The main goal of this is to get a general insight into the shapes of waveforms. This knowledge will be then utilized to interpret the results of measurements and FEM simulations.

The excitation signal creates a sinusoidal $H$ field in the core. The magnetic field in the two straight segments of the core can then be described as

$$H_1 = H + H_{ext} \tag{5.1}$$

$$H_2 = -H + H_{ext} \tag{5.2}$$

where $H_{ext}$ is external DC magnetic field.

The resulting $B_1$ and $B_2$ fields can be calculated from $H_1$ and $H_2$ using BH curve. The flux through the pickup coil is proportional to the sum of $B_1$ and $B_2$ (they are defined in the same direction; one of them is negative). The induced voltage then depends on the change of that flux in time. This model ignores constant parameters (physical dimensions, coil turns, etc.), so the induced voltage is expressed as being proportional to the derivative of $(B_1 + B_2)$.

## 5.1 Modeling the Relation Between $H$ and $B$ in the Core

The simplest way to model this relation would be a function consisting of three segments: two saturation regions, where $\mu_r = 1$, and a linear region of material's permeability. This introduces a sudden change of permeability at the point where the linear segment changes to saturation. This is unrealistic. To smooth out the curve, PCHIP[28] method was used, giving the result shown in figure 5.1. It is worth noting that the values in the plots are not to scale when the axis is not labeled; only the shape of the waveforms is relevant.

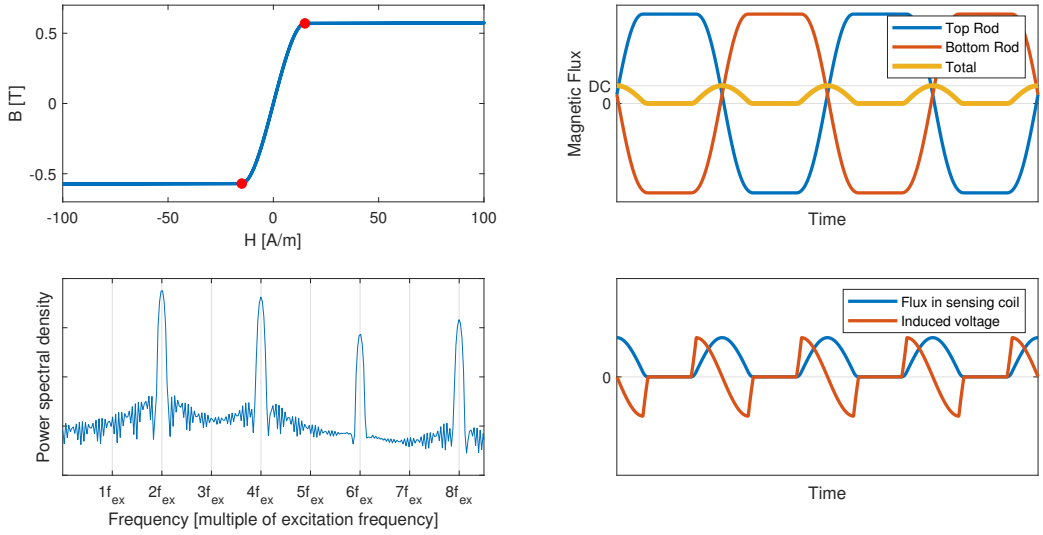


**Figure 5.1:** Results using the simplified model with simplified BH curve

### 5.1.1 Using BH Curve of VITROVAC 6025 X

To get more realistic results, BH-loop measurement of a real material can be used. Kubík measured the B-H loop of VITROVAC 6025 X material for 30mm core in his thesis[8]. The Ansys material definition allows to set data table of nonlinear B-H curve, but not the whole hysteresis loop. For this reason, Kubik measured what he calls the "BH Curve for FEM Modelling". His thesis does not describe the exact procedure of obtaining values of this curve. It seems that it was created by measuring hysteresis loops for different amplitudes and using the "corners" of the loops. This corresponds to amplitude permeability or the initial magnetization curve.

**Table 5.1:** B-H curve points of VITROVAC 6025 X by Kubik[8]

| $H$[A/m] | 0 | 0.9 | 1.89 | 3 | 4.43 | 6.35 | 17 | 58 | 30000 |
|---|---|---|---|---|---|---|---|---|---|
| $B$[T] | 0 | 0.027 | 0.077 | 0.18 | 0.35 | 0.44 | 0.54 | 0.57 | 1 |

#### Issues with the Usage of Real BH curve

Results obtained using this are shown in figure 5.3. The result differs quite dramatically from the measured waveform. The induced voltage has two pairs of up-down peaks instead of one. The reason for this discrepancy is the shape of the BH curve.

In figure 5.2, it can be seen that the slope of the curve starts with a low slope that gradually increases. This, however, does not correspond to the actual B-H loop, which crosses zero with maximum slope. The consequence of this is, that the total flux drops to zero when the excitation changes direction. There are two peaks in the flux instead of one, and thus, two pairs of up-down spikes in induced voltage.

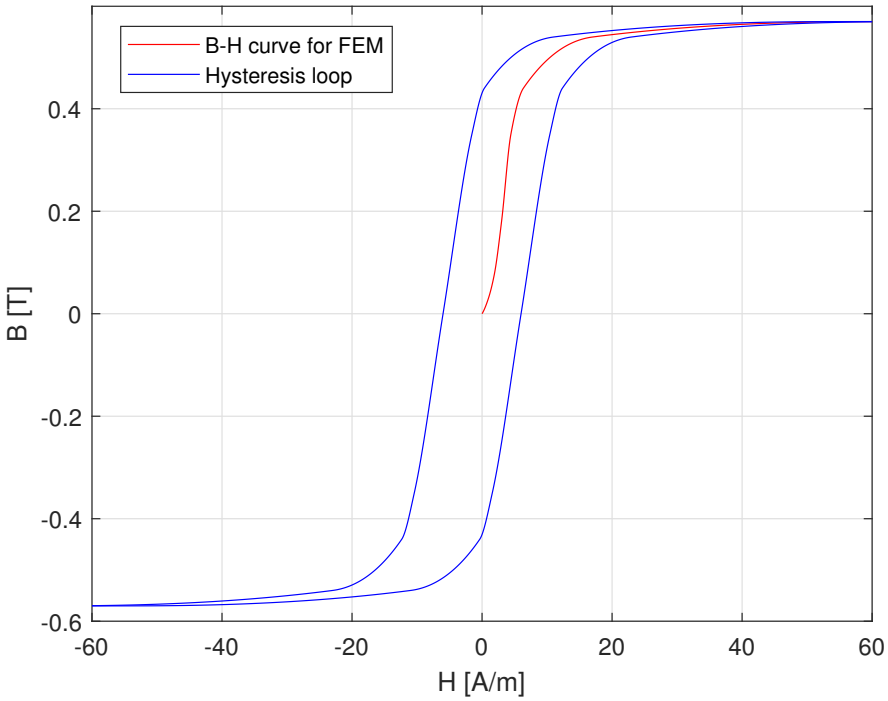


**Figure 5.2:** Hysteresis loop of 30mm VITROVAC 6025 X racetrack by Kubik[8]

This observation can be generalized into the following statement: The BH curve used for simulation must be strictly concave (negative $2^{\text{nd}}$ derivative) in the positive half (and vice versa). Any convexity would result in additional spikes in the induced voltage, which does not correspond to experimental data.

The solution for this is to remove samples near zero from the BH curve data (which seems to be a common practice). The result in figure 5.4 is significantly improved but still contains minor unwanted spikes. Further improvements must be made when preparing the BH curve for FEM simulation. This will be discussed in the next chapter.

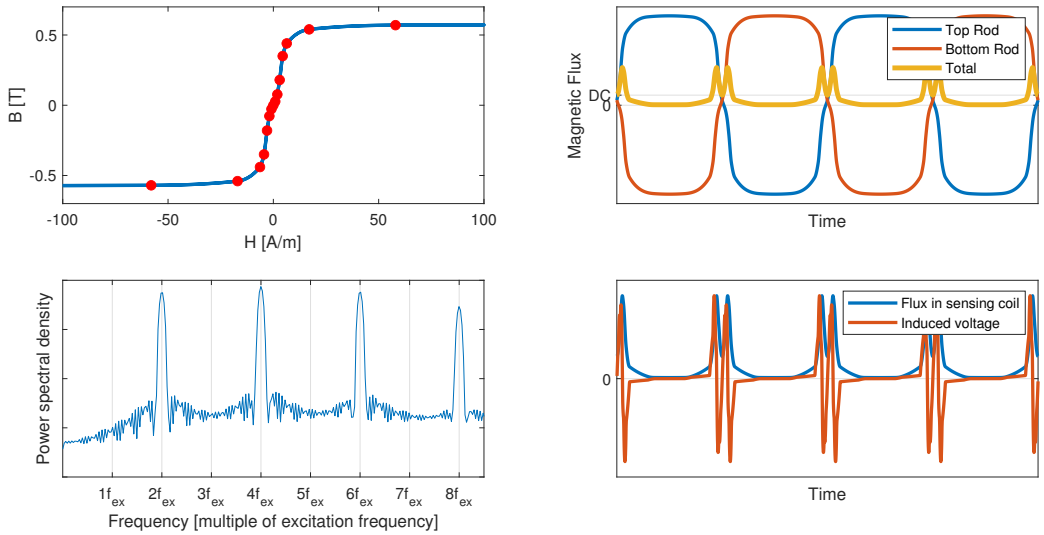


**Figure 5.3:** Results using the simplified model with Kubík's BH curve

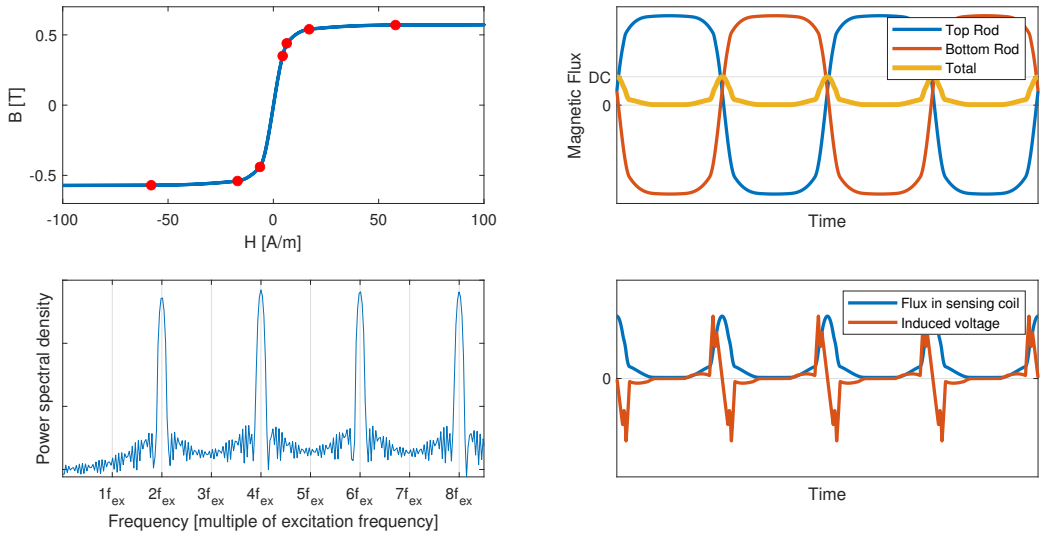


**Figure 5.4:** Results using the simplified model with modified Kubík's BH curve

# Chapter 6

# Material Properties

The material used for the core is named VITROVAC 6025 F. I measured its magnetic properties myself. Core with the following dimensions was used:

$$l = 30 \text{ mm}$$

$$d = 10 \text{ mm}$$

$$T = 2 \text{ mm}$$

$$t = 25 \ \mu\text{m}$$

## 6.1 Measurement Setup

The core was placed inside a 3D printed holder and coils were wound around it. Excitation coil ($N_1 = 30$ turns) on both straight segments and sensing coil ($N_2 = 15$ turns) on one side only. Measurement was performed at 1 kHz, 10 kHz, and 100 kHz.

The excitation coil is powered by an arbitrary waveform generator. Both channels of the generator are synchronized and connected in parallel to increase output power. Maximum output voltage (20 $V_{pp}$) corresponds to about 750 $mA_{pp}$. Current is measured as a voltage drop across 1Ω resistor. A current probe was also used, but it proved to be worse than the resistor, as it caused a slight phase shift of the measured signal, which led to significant distortion of the BH loop.

## 6.2 Measurement Evaluation

By measuring the current through the excitation winding, we can calculate the magnetic field intensity $H$ as follows:

$$H = \frac{IN_1}{l} \tag{6.1}$$

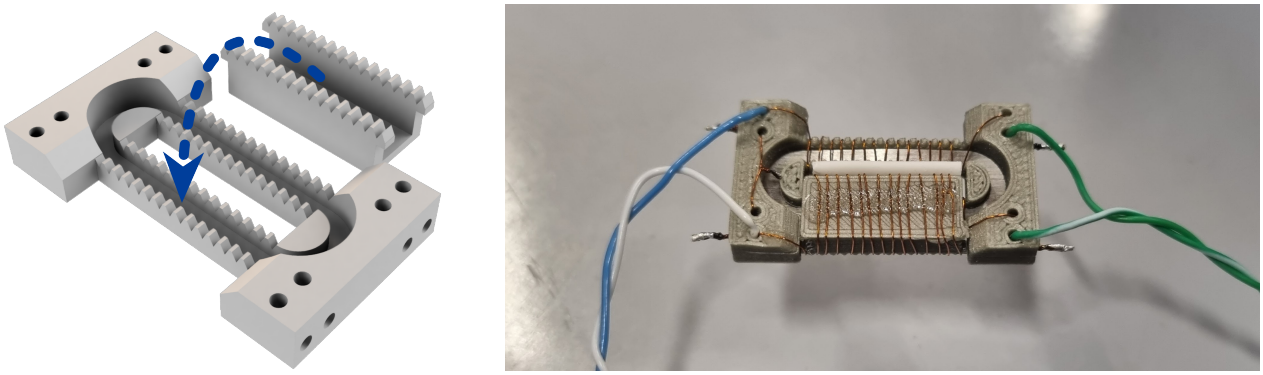

**Figure 6.1:** Core holder with coils

The number of coil windings $N_1$ is 30, $l$ denotes the mean length of a path around the core, which can be evaluated as

$$2 \cdot 20 \text{ mm} + \pi \cdot 8 \text{ mm} \doteq 65 \text{ mm} \tag{6.2}$$

To calculate the magnetic flux density $B$, we first need to calculate the flux in the sensing coil by integrating the induced voltage that we measure.

$$\Phi = \int V_i \, dt + \Phi_0 \tag{6.3}$$

Integration was performed numerically on the digitally measured data. To determine the constant term, we can assume that the mean flux is zero over one period of the signal (the BH loop is symmetric around zero).

Flux through the coil consists of flux in the material and flux in the air inside the excitation coil, as shown in figure 6.2 (we assume that the field outside the excitation coil is zero). Flux in the air can be calculated using

$$\Phi_{air} = \mu_0 H N_2 (S_a - S_m) \tag{6.4}$$

and subtracted from the total flux. From that, we can calculate the flux density $B$ in the material.

$$B = \frac{\Phi - \Phi_{air}}{N S_m} \tag{6.5}$$

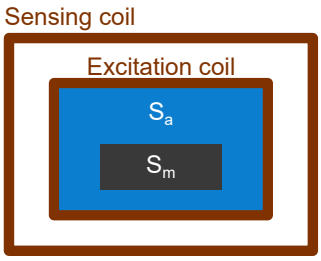


**Figure 6.2:** Cross-section of coils wound around the core

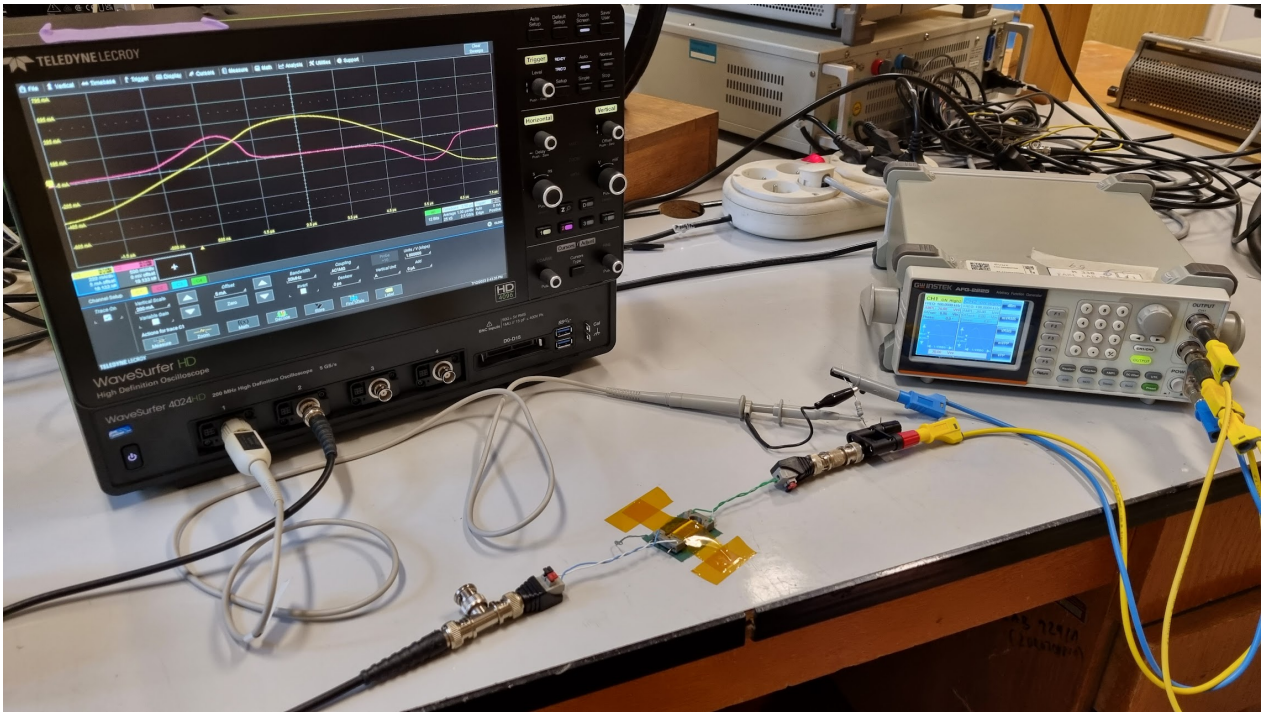


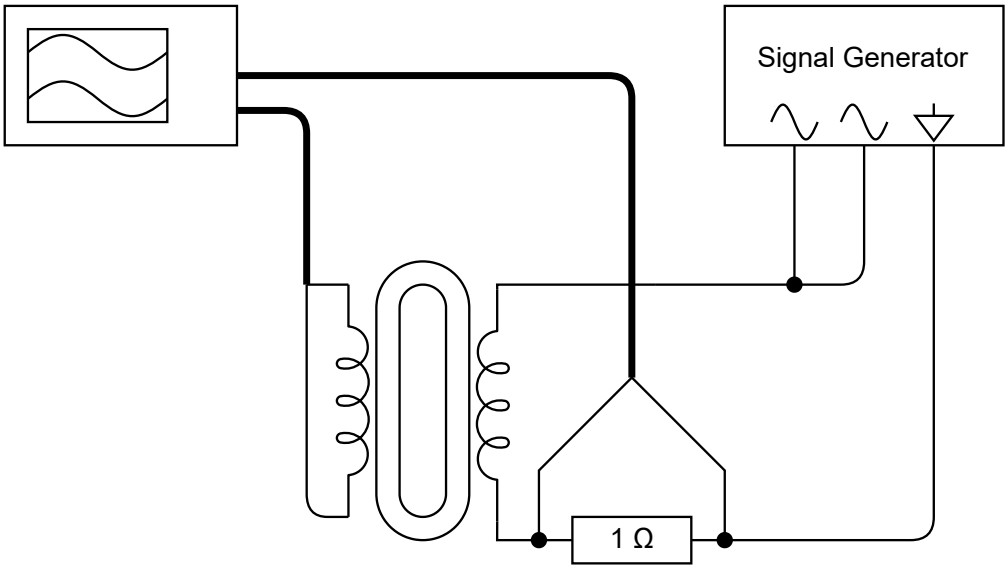


**Figure 6.3:** Setup for BH loop measurement

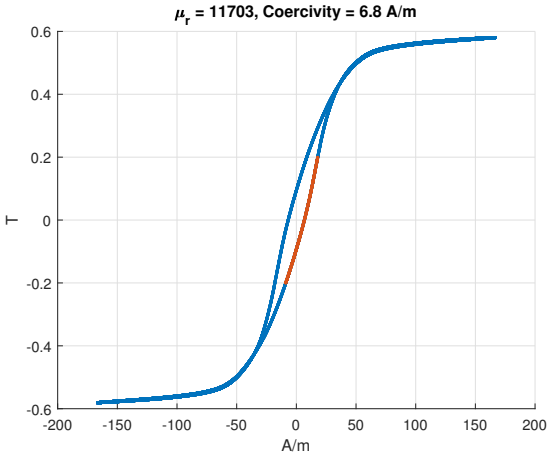


**(a) :** 1 kHz

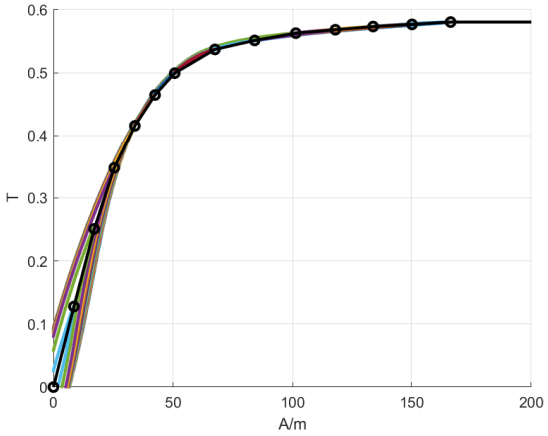


**(b) :** 1 kHz

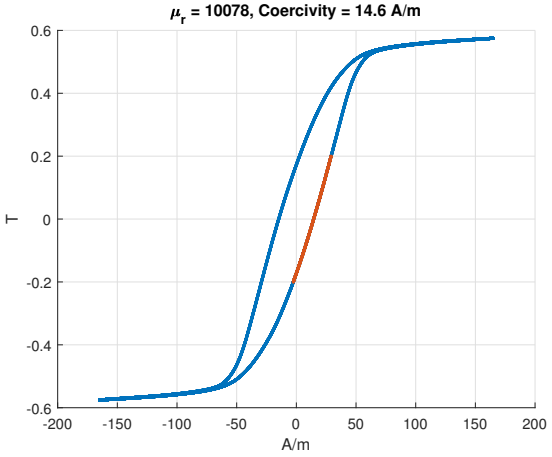


**(c) :** 10 kHz

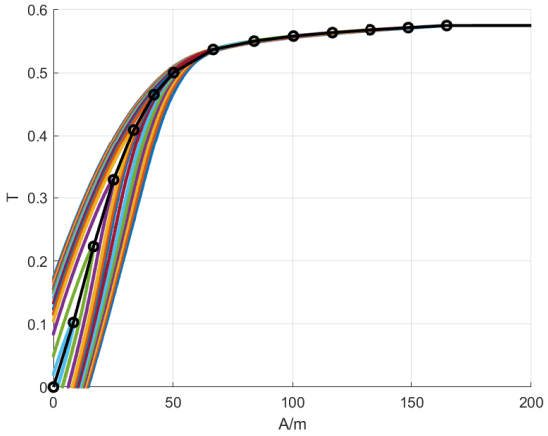


**(d) :** 10 kHz

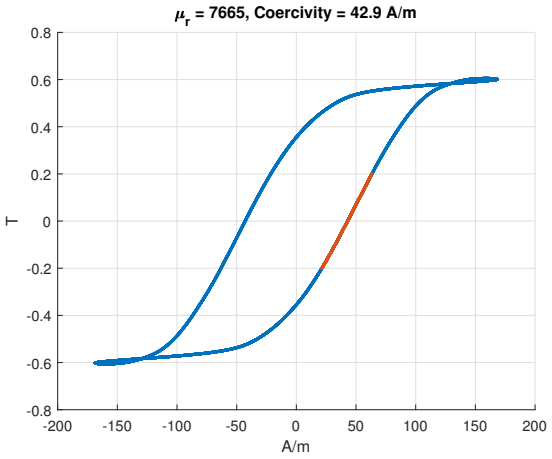


**(e) :** 100 kHz

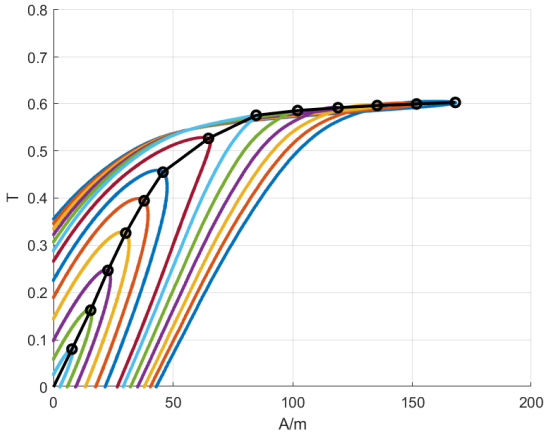


**(f) :** 100 kHz

**Figure 6.4:** Measured BH characteristics of VITROVAC 6025 F

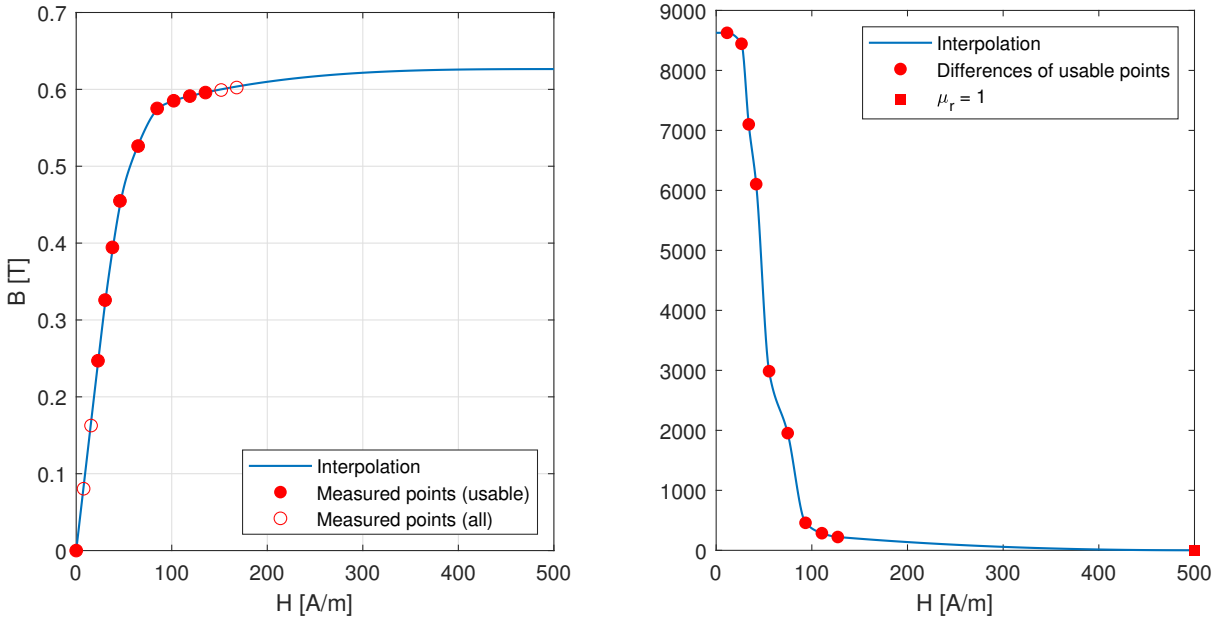


**(a) :** B-H curve

**(b) :** Differential permeability (relative to $\mu_0$)

**Figure 6.5:** Interpolation of measured B-H curve of VITROVAC 6025 F at 100 kHz

## 6.3 BH Curve for FEM simulation

The shape of the BH curve has a severe impact on simulation results (as discussed in 5.1.1). It must be ensured that the permeability is monotonously decreasing with increasing H. The interpolation was performed by the following method:

1. Calculate differential permeability
2. Remove points that would cause a positive slope of the relative permeability
3. Add $\mu_0$ as the last point of the relative permeability at a high value of H
4. Interpolate the relative permeability using the PCHIP method
5. Integrate the relative permeability to obtain the B-H curve
6. Tweak the scale of the B-H curve to fit the last measured point (saturation $B$)

This procedure is described in detail by Matlab code on the next page. Measure data points used for this are in Appendix A.

```
% BHCurvePoints contains pairs of H and B values of the amplitude permeability measurement

% Remove samples that would result in a positive slope of the relative permeability
BHCurvePoints = BHCurvePoints(4:end-2,:);

% Create a symmetrical B-H curve by mirroring and appending the original curve data
BHCurvePoints = [-flip(BHCurvePoints,1);[0,0];BHCurvePoints];

% Define H values for which the resulting curve will be calculated
step = 1;
BH_H = [0:step:500];

% Extract B and H values from the curve data
raw_b = BHCurvePoints(:,2);
raw_h = BHCurvePoints(:,1);

% Midpoints between consecutive H values are used as H coordinates of the derivatives
raw_diff_h = (raw_h(1:end-1) + raw_h(2:end)) / 2;

% Calculate the derivative of B with respect to H using finite differences
raw_diff = diff(raw_b)./diff(raw_h);

% Set the last point of the derivative to the vacuum permeability
raw_diff_h = [raw_diff_h; BH_H(end)];
raw_diff   = [raw_diff  ;        mu0];

% Interpolate the derivative values using PCHIP method
smooth_diff = interp1(raw_diff_h,raw_diff,0:step:raw_diff_h(end),'pchip');

% Remove any NaN values that might occur during derivation and interpolation
smooth_diff = smooth_diff(~isnan(smooth_diff));

% Integrate the smoothed derivative values to obtain the B-H curve
BH_B = cumtrapz(BH_H,smooth_diff);

% Adjust the scale of the resulting B-H curve to match the top value from the raw data
top_raw = raw_b(end);
top_fine =  BH_B(round(BH_H) == round(raw_h(end)));
BH_B = BH_B * top_raw / top_fine;

% BH_H and BH_B are the result
```

# Chapter 7

# Transient simulations

Transient analysis has been done to evaluate the sensor's sensitivity and optimal excitation current. This analysis was done in Ansys Electromatics Maxwell 3D software. Sinewave signal at 100 kHz frequency is used in the simulations. The sensitivity would increase linearly with increasing frequency (it is proportional to $\frac{dV}{dt}$) until the output becomes attenuated by parasitic effects. Effects like parasitic capacitances are not included in the simulation model. The 100 kHz is selected as a baseline for comparing different structures. Sensitivity at various frequencies will be evaluated by measurement of the fabricated micro-fluxgate device.

## 7.1 Model and Setup

The excitation coil is modeled in detail, with each turn as a separate object. The sensing coil is modeled as a single solid structure. The model is parametric (controlled by the dimensions of the core) and is used for both macro-version (to compare with measurements) and the micro-version.

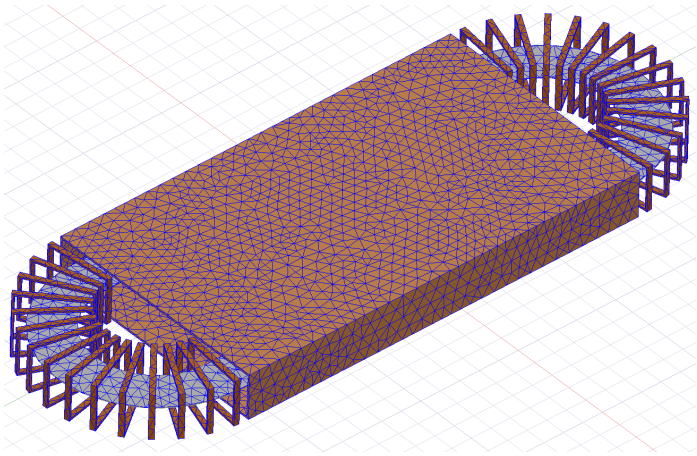

**Figure 7.1:** Fluxgate model with mesh

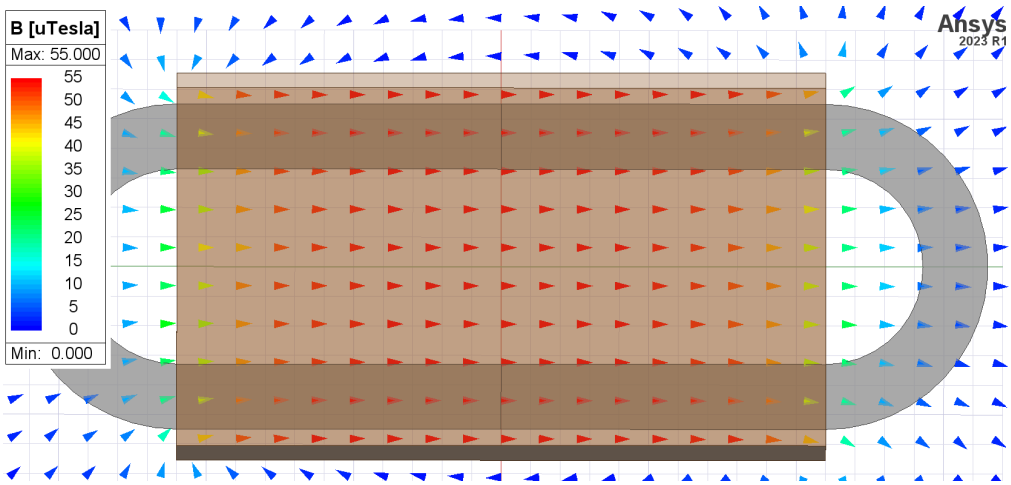


**Figure 7.2:** Simulated magnetic field produced by DC current in the sensing coil

### 7.1.1 External Magnetic Field

The transient analysis does not allow directly setting an external field using boundary conditions (this was possible in the magnetostatic simulation used in chapter 3). One possible way to create the DC field is by modeling Helmholtz coils around the fluxgate model. Another way would be to apply DC current to the sensing coil of the fluxgate to create the field. This is similar to the feedback current in a closed-loop configuration. The advantage of this approach over the Helmholtz coil approach is that it does not add any additional structures to the model. On the other hand, the Helmholtz coil model adds more mesh elements, leading to increased computation time (it may not be a significant increase).

#### Generating External Field using sensing coil

The current was selected such that the magnetic field created by the coil is around 50 $\mu$T. That is similar to the Earth's magnetic field, which ranges from 25 to 65 $\mu$T[27]. The current needed was obtained using the approximation of the magnetic field inside a solenoid:

$$B = \frac{\mu_0 N I}{l} \tag{7.1}$$

where $N$ is number of coil turns, $I$ is the current, and $l$ is length of the coil. The exact value was obtained by magnetostatic simulation. A suitable integer value was selected to get near the 50 $\mu$T. It should be noted that (7.1) estimates the magnetic field in the middle of the solenoid. Without a ferromagnetic core, the field at the end of the solenoid is half of that value.

**Table 7.1:** sensing coil DC current settings for simulation

| Model | Coil turns | Coil length [mm] | Current [mA] | Theoretical [$\mu$T] | Simulated [$\mu$T] |
|---|---|---|---|---|---|
| Macro | 50 | 16.7 | 18 | 67.7 | 51.0 |
| Micro | 50 | 3.67 | 4 | 68.4 | 51.2 |

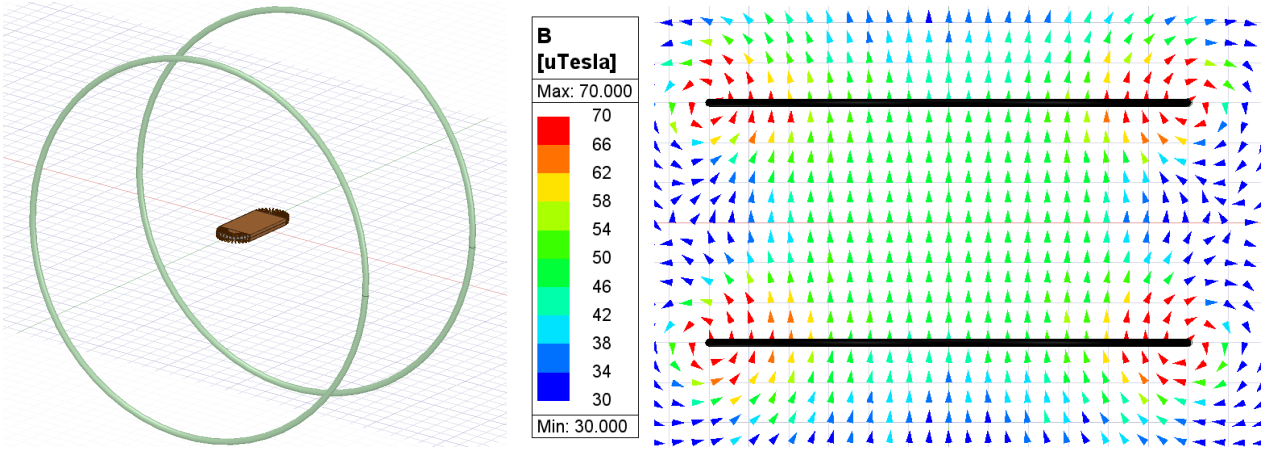


**(a) :** Model **(b) :** Simulated field

**Figure 7.3:** Modeled Helmholtz coil around the fluxgate

### Generating External Field using Helmholtz coil

Helmholtz coil consists of two circular coils placed coaxially at a distance equal to their radius. The magnetic field at the midpoint between the two coils can be calculated using the following equation:

$$B = \left(\frac{4}{5}\right)^{\frac{3}{2}} \frac{\mu_0 NI}{R} \approx 0.71554 \cdot \frac{\mu_0 NI}{R} \tag{7.2}$$

where $\mu_0$ is the permeability of free space, $N$ is the number of turns in each coil, $I$ is the current flowing through the coils, and $r$ is the radius of the coil. This equation was used to calculate the current needed for a 50 $\mu$T field. Compared to a solenoid, the homogeneity of the Helmholtz coil magnetic field is much better.

## 7.1.2 Mesh

The minimum length of mesh elements is set relative to the length of the core (to scale with the model automatically). The fluxgate has a mesh resolution of $l/40$, surrounded by a box about twice its size with mesh $l/10$, and the whole bounding region has a minimum mesh step equal to $l$. The mesh consists of around $10^5$ tetrahedra.

## 7.1.3 Analysis Setup

The simulation stops at time 12.5 $\mu$s, which is one and a quater period. The first 2.5 $\mu$s section is not saved as it may be affected by rapid changes at time 0. The time step is set uniformly to a value of 0.01 $\mu$s, meaning 1000 samples per period. Convergence criteria are Nonlinear Residual = 0.001 and a minimum of 10 nonlinear iterations. The Smooth BH Curve option is not enabled because the BH curve data were manually interpolated in Matlab as described before.

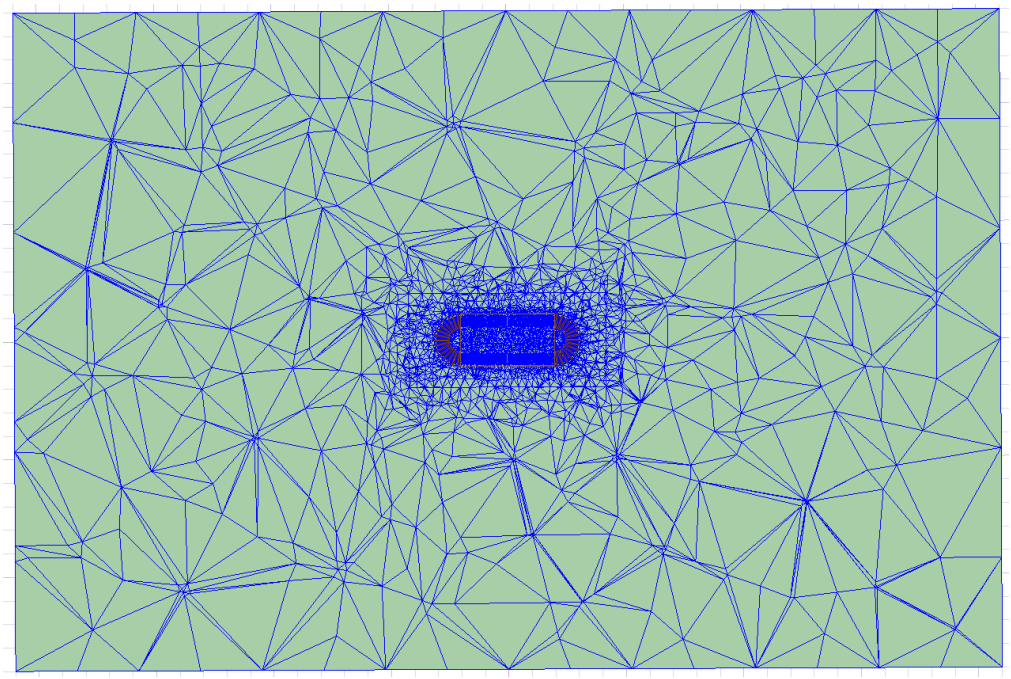

**Figure 7.4:** Fluxgate model mesh

## 7.2 Performance

Simulation has been run on a computer with an Intel Core i7-9700K 8-core processor clocked at 4.7 GHz with 32 GB memory. Simulating over one period of excitation signal takes around 30 hours. Four variations could be computed in parallel. The usage of the Helmholtz coil model for the external field only had a minor impact on the performance.

## 7.3 Results for Macroscopic Model of Micro-fluxgate Structure

Figure 7.5 compares measured and simulated results. The measurement 1 (Without amplifier) corresponds to simulation 2 (with external field created by Helmholtz coil) very well. The second measurement (using an amplifier for excitation signal) gives higher values, but this is deemed less reliable than the first measurement.

Comparison of time-domain signal in figure 7.6 shows that the measured and simulated signals are reasonably similar. The measured waveform is noticeably smoother, which can be explained by assuming that higher frequency components of the signal are suppressed by parasitic capacitances, which are not accounted for in the simulation. Spectra in 7.7 are also similar. The simulated spectrum does not contain any odd harmonics (because the simulation model is perfectly symmetric). The measured spectrum contains some signal on odd harmonics, but it is 25 dB lower than the even harmonics.

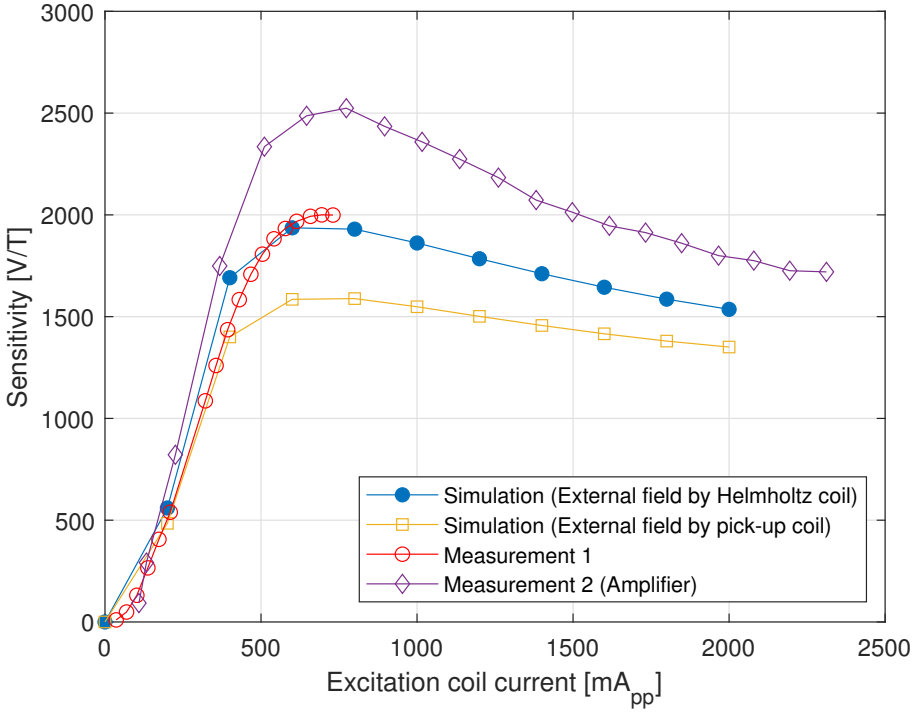


**Figure 7.5:** Comparsion of simulated and measured sensitivity (Macro-model; 100 kHz)

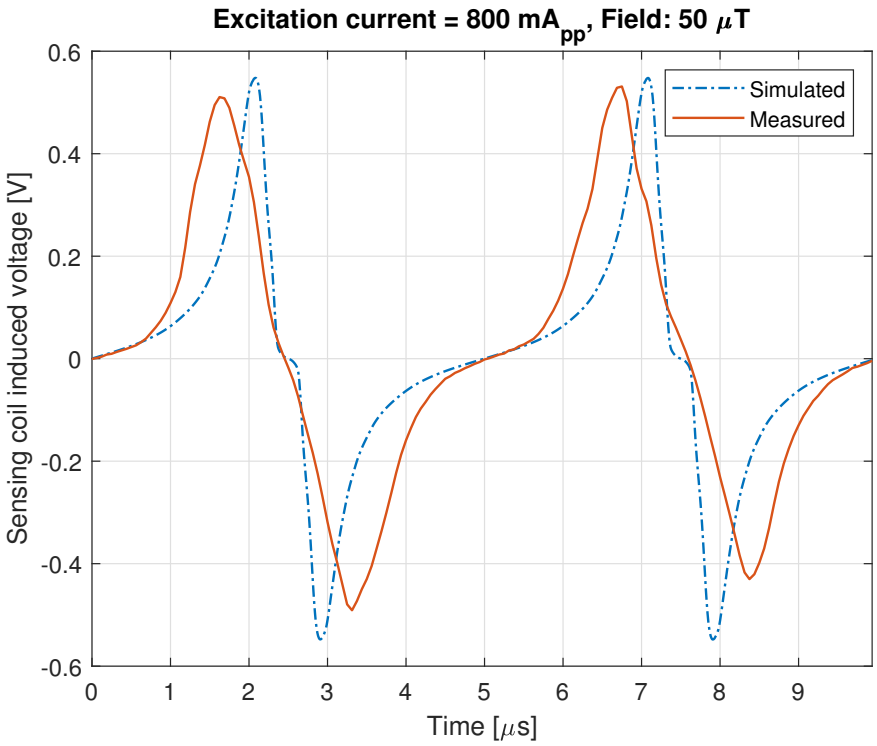


**Figure 7.6:** Comparsion of simulated and measured induced voltage (Macro-model; 100 kHz)

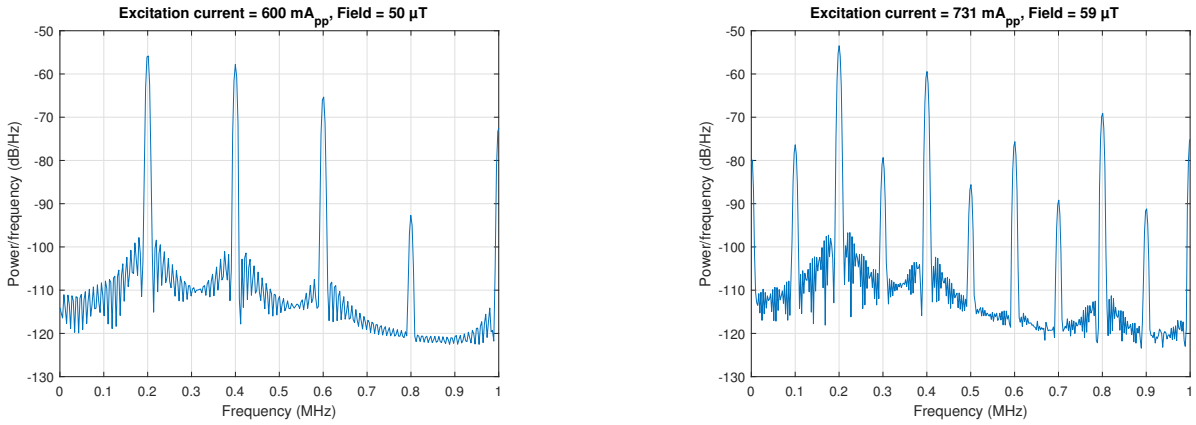


**(a) :** Simulated

**(b) :** Measured

**Figure 7.7:** Comparsion of simulated and measured spectrum of induced voltage (Macro-model; 100 kHz)

## 7.4 Results for Micro-Fluxgate Version 1

The induced voltage waveform is similar to the macro version, which is expected. The maximum sensitivity occurs at 200 $mA_pp$ excitation current compared to the 800 mA in the macro case. The scaling factor of physical dimensions is 0.22, and the excitation coil field should decrease linearly with that (by 7.1). Therefore, the 200 $mA_pp$ is slightly higher than expected. Maximum sensitivity is only around 8 % of the macro version.

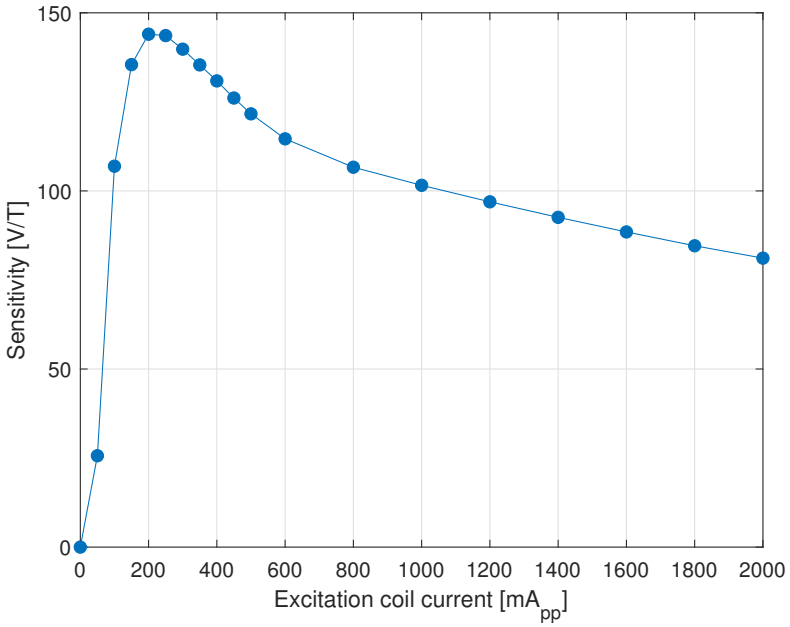


**Figure 7.8:** Simulated sensitivity at (Micro-fluxgate version 1; 100 kHz)

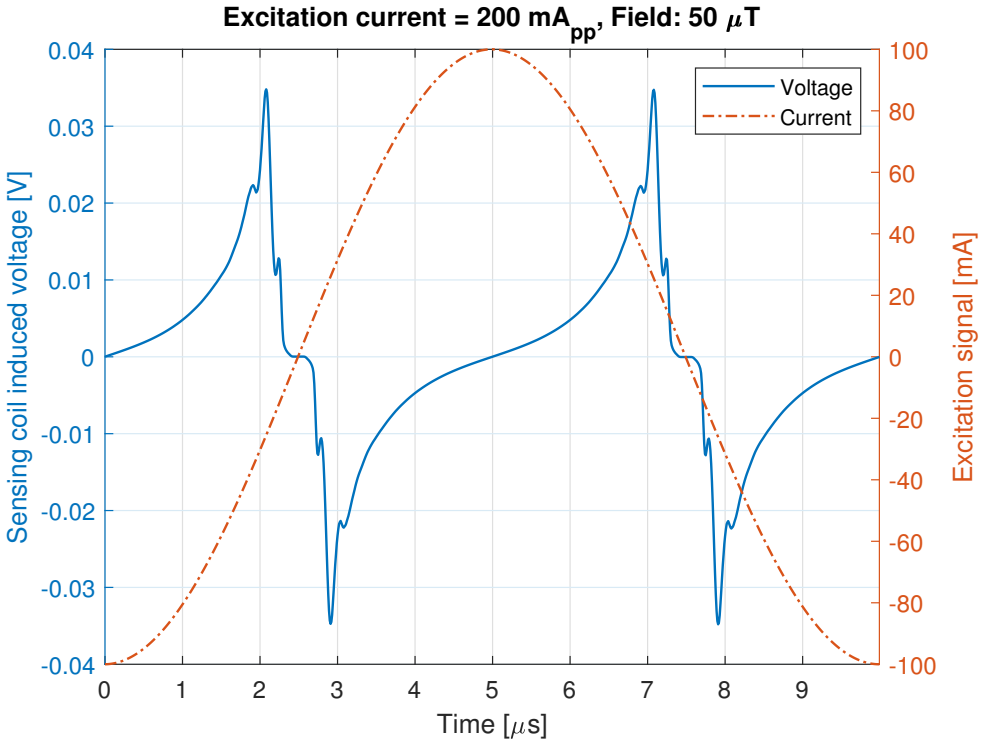


**Figure 7.9:** Simulated induced voltage (Micro-fluxgate version 1; 100 kHz)

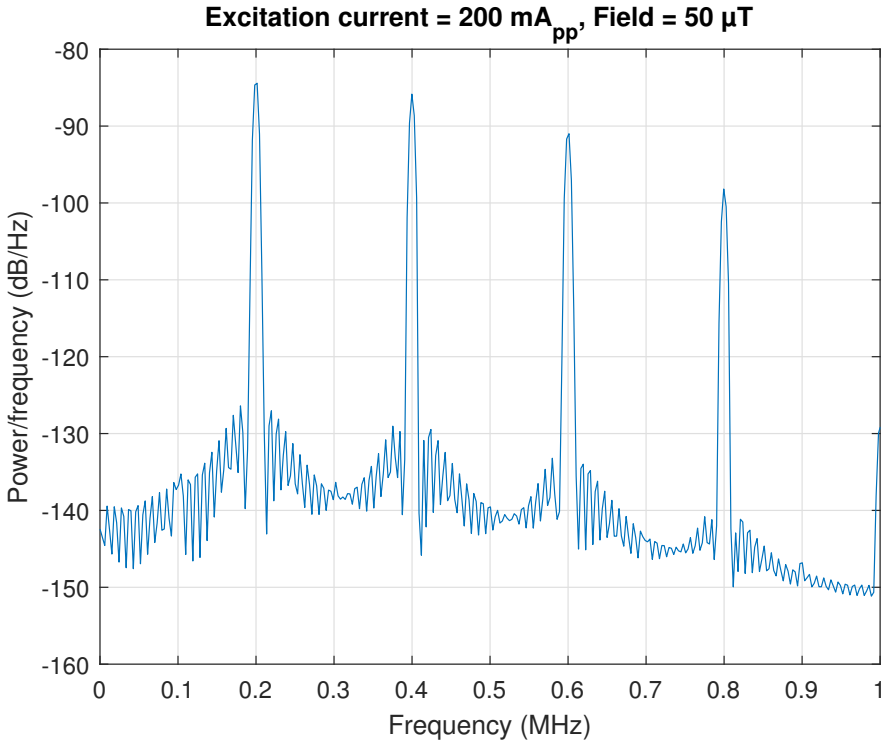


**Figure 7.10:** Simulated induced voltage spectrum (Micro-fluxgate version 1; 100 kHz)

# Chapter 8

# Micro-Fluxgate Version 1 Fabrication and Results

Fabricating the micro-fluxgate involves multiple steps. The most important step is the fabrication of the chip. The core of the fluxgate, made of amorphous metal, was also fabricated. The device is then assembled by gluing the core in place on top of the chip and creating the coil structure by wire bonding. The chip is placed and bonded directly to a PCB without being packaged (COB).

## 8.1 Chip Layout and Fabrication

The technology of choice is UMC 0.18$\mu$m process. As mentioned in chapter 2, my part of the design was concluded by drawing the metal layer layout in KiCAD. The layout was exported in DXF format and forwarded to NTUST to convert the layout into proper EDA tools and apply for fabrication at TSRI. The conversion of my DXF layout into chip layout in Cadence software was handled by one of the NTUST students (I was at CTU in Prague at the time). Apart from simply converting file formats and assigning correct layers of the technology, the student also needed to do additional refactoring of the design:

- Each of the metal layers has a specified minimum area covered by metal (30 %); this meant that some empty areas in the fluxgate layout (M6) and in the unused layers (M1 to M5) had to be partially filled. According to my instructions, the filling was supposed to be done in such a way that no conductive loops would be created (to minimize the chance of causing interference with the sensor's operation).
- There must not be a continuous square of metal larger than 30 $\times$ 30 $\mu$m. All areas larger than that have to be split into segments by creating gaps, as shown in figure 8.2 (they call it "punching holes"). This not only applies to filled areas but also the coil traces because they are wider than the aforementioned 30 $\mu$m.
- Bonding pads need to have vias to metal below for higher sturdiness; also, passivation windows have to be defined above the pads.

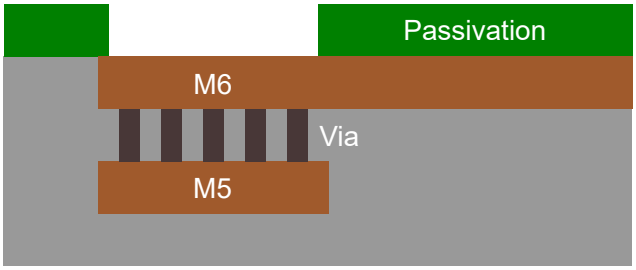


**Figure 8.1:** Typical structure of a bonding pad

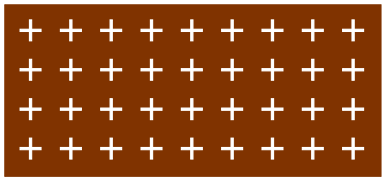

**Figure 8.2:** Splitting large metal areas to pass DRC

## 8.2 Core Fabrication

The core is made of VITROVAC 6025 F, an amorphous metal, is magnetically soft, and has a very high permeability. It comes in the form of a sheet with a minimum thickness of 25 $\mu$m. [29]

### 8.2.1 Fabrication at CTU

At first, the fabrication of the core was attempted in a laboratory at the Czech Technical University (CTU). This attempt was not successful at all. The process went as follows:

1. Cut a small rectangular piece of the metal sheet
2. Glue the piece on a glass plane to ensure a flat and even surface and better handling (negative photoresist was used as glue)
3. Apply negative photoresist on the top side of the metal rectangle using a spin-coater.
4. Project the motive using direct exposure (without mask) lithograph
5. Develop the exposed photoresist
6. Chemical etching

The main issue was that the photoresist did not work well as a glue. It only hardened around the edges and not in the whole area between the metal and glass (it stayed liquid and probably could not dry because of no access to air). As a result, the metal peeled off the glass in the etching solution. Apart from that, the etching was also too slow.

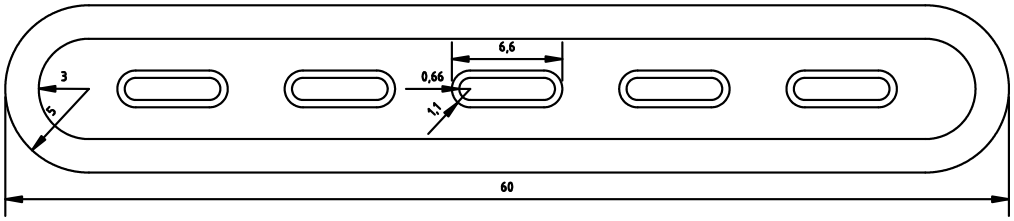


**Figure 8.3:** Small cores inside big core for fabrication in Semach

**Figure 8.4:** Cores manufactured by Semach in Feb 2023

### 8.2.2 Fabrication by Semach

Fabrication of the core was outsourced to a Czech company named Semach s.r.o. This company previously manufactured racetrack cores for macro-sized fluxgates for Prof. Ripka. Professor Ripka ordered some new macro-sized cores from the company, and we also included micro-cores in the order. The small cores were embedded inside the large ones in the design, as shown in figure 8.3, to save material.

The cores were produced by wet etching from both sides. For technical reasons, there had to be bridges between the cores and the frame around them (so they would not get lost in the etching bath). Early versions were not good, but the process was improved eventually. Figure 8.4 shows one of the acceptable results. I had to cut these bridges manually. I did that using a high-quality knife under a microscope. Cutting the bridges without leaving stubs was challenging but possible.

## 8.3 Results

Unfortunately, the modifications mentioned in section 8.1 were not discussed carefully enough, leading to errors in the layout. It was not possible for me to review the final design before the tape-out. As a result, the fabricated chip has two major flaws:

- The passivation windows were drawn in an incorrect layer. This led to all pads being covered by the passivation layer. Such a mistake can be explained by the fact that in typical IC design, the designers use standard cell libraries for the IO pads and are unfamiliar with manually drawing the pad.
- The "hole punching" (adding gaps into too-large metal areas) was done in an arbitrary manner. Gaps were often placed in a way that unnecessarily decreased the effective width of the traces, thus increasing their resistance.

The missing passivation windows were a problem that could not be overcome. Despite an extensive effort by the bonding company, they were not able to punch the bonding wires through the passivation layer and bond to the metal beneath. Therefore, this attempt is considered unsuccessful.

### 8.3.1 Improved Workflow for Next Version

To prevent such errors in the next version, I decided to make changes in the design workflow. The KiCAD software will still be used to lay out the coils around the core. However, instead of attempting to convert the whole design, only the positions of the pads will be exported. Layout of the chip will then be made "from scratch" using Virtuoso EDA. Metal paths will be routed manually (with a systematic approach to metal area limitations), and IO pads from a library will be used for the pads.

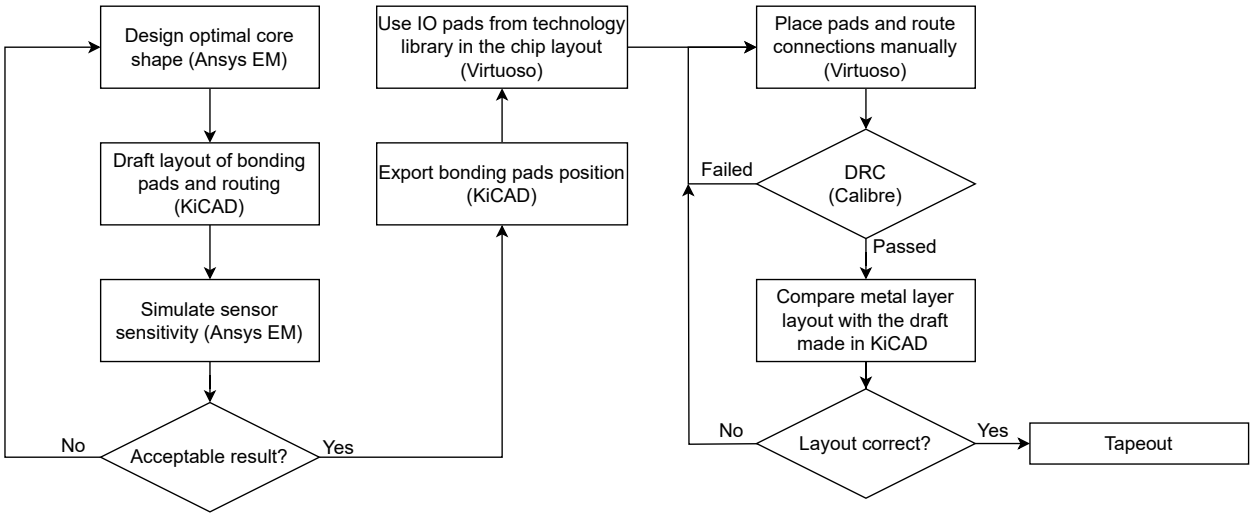


**Figure 8.5:** Workflow for designing next micro-fluxgate version

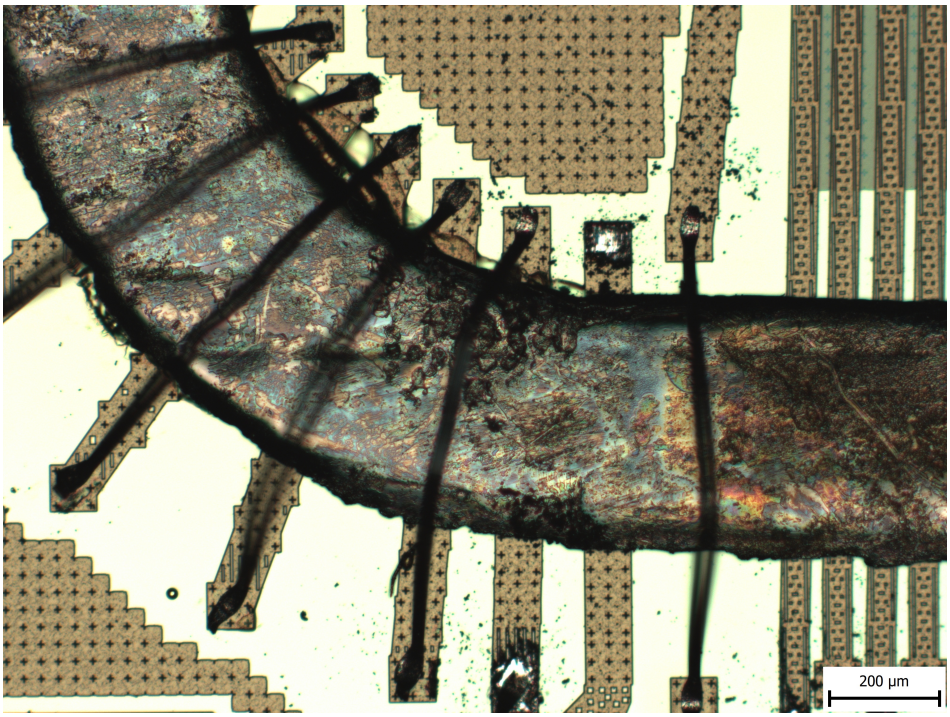


**(a) :** Attempted bonding on the pads covered with passivation

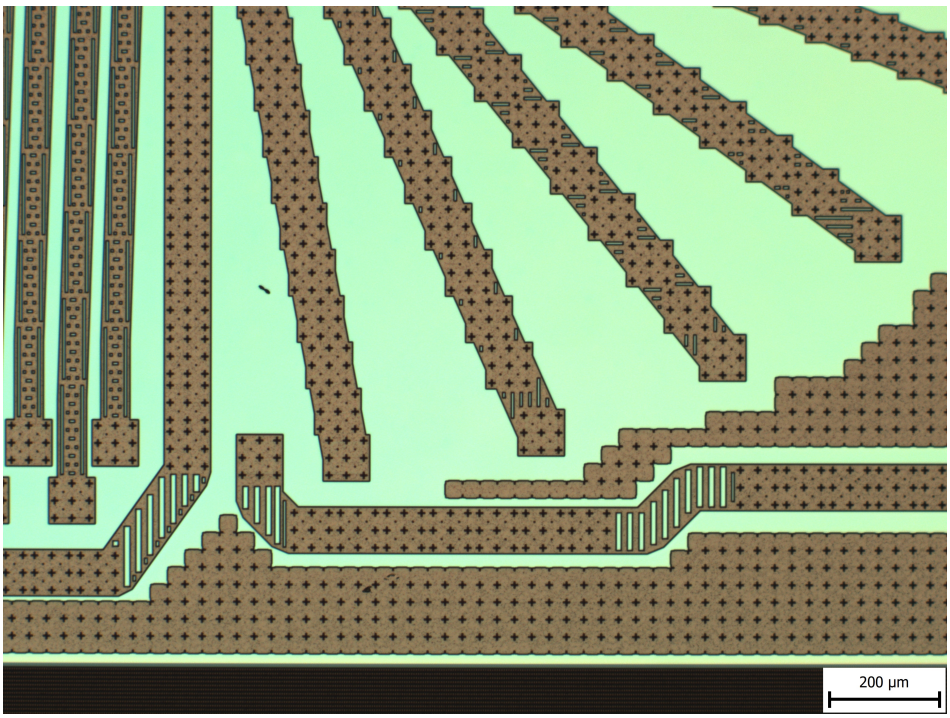


**(b) :** Unsystematic solution of metal area restrictions

**Figure 8.6:** Errors in the first version of micro-fluxgate

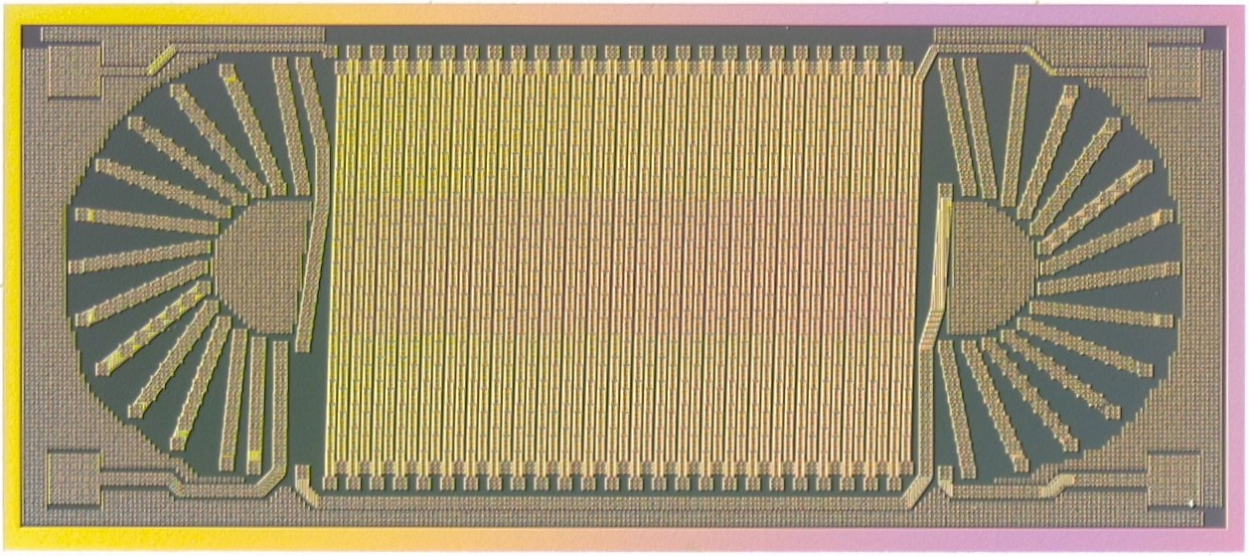

**(a) :** Chip

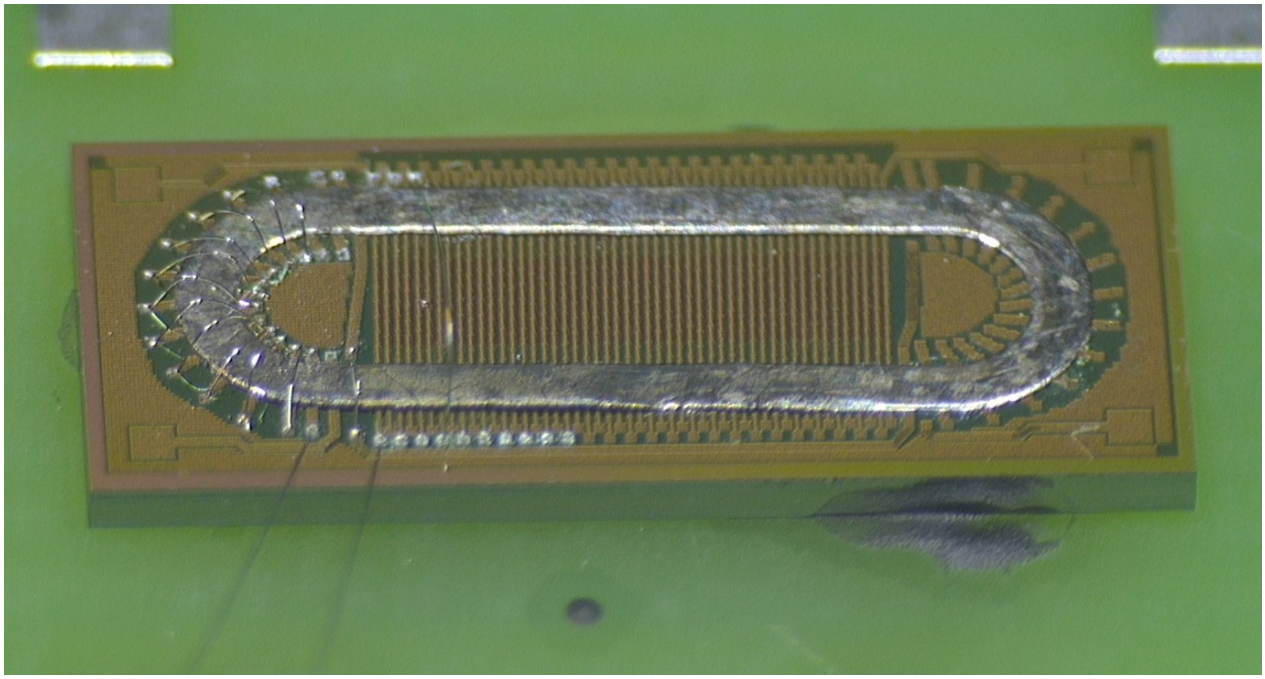

**(b) :** Partially assembled device placed on PCB

**Figure 8.7:** Micro-fluxgate version 1

# Chapter 9

# Optimizing Core Size for the Second Version of Micro-Fluxgate

An optimized shape of the core is used for the second version of the micro-fluxgate. Parametric simulation is done to determine the optimal shape. There are three degrees of freedom in shaping the core: $l$, $d$, and $T$. Doing a detailed parametric simulation of all three together would lead to a large number of variations, meaning unreasonably long computation time. Also, it would not be possible to visualize results in any practical way.

## 9.1 Length versus Width

As a first step, I simulated the dependence on $l$ and $d$ with $T = 0.44$ mm.

The demagnetization factor is decreasing when both $l$ and $d$ are increased. That is expected, as it is equivalent to decreasing thickness while keeping the same size. If we limit ourselves to the maximum area, it is favorable to increase $l$, while decreasing $d$ to fit the maximum area.

## 9.2 Effect of Track-width

Now it's time to evaluate the effects of changing $T$ as well. Figure 9.1 clearly shows that a larger total area leads to lower demagnetization. Therefore, it is possible to shrink the problem in two dimensions by slicing the $l$-$d$ plane along the curve of the maximum allowed area. The following simulation is set up in this way:

- $l$ is swept in the same range and step as before (5 to 10 by 0.1 mm)
- $d$ is calculated to satisfy constraints:

$$d = \frac{25 \text{ mm}^2}{l + 1 \text{ mm}} - 1 \text{ mm}$$

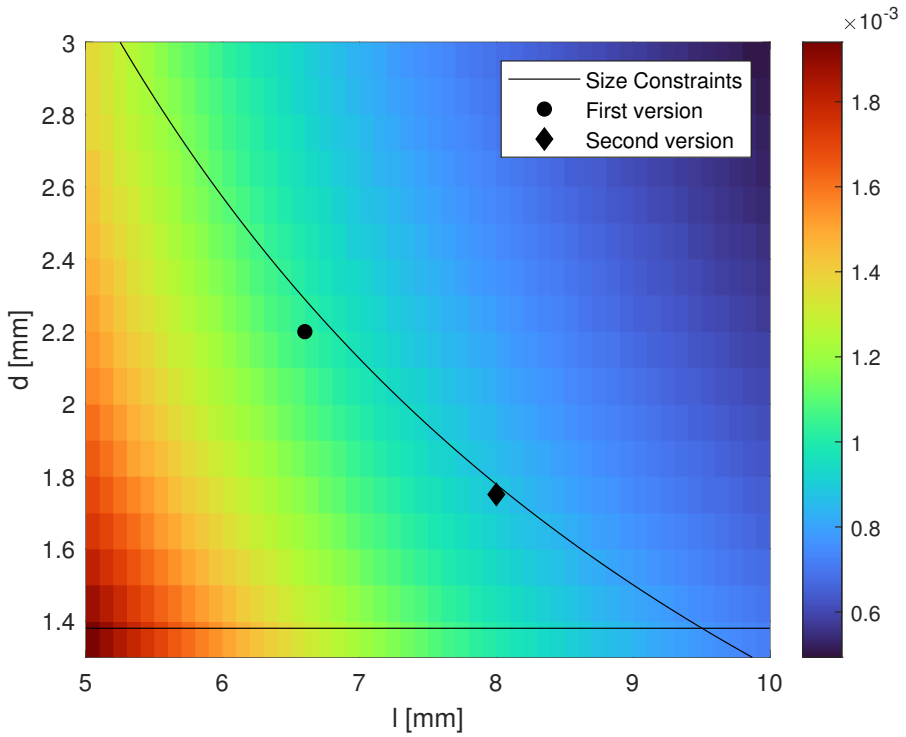


**Figure 9.1:** Demagnetization factor of straight segment, $T = 0.44$ mm

A range of $T$ values is swept for each $l$-$d$ pair. To set up a parametric simulation for these points, I used the 'Parametric From File' option in Ansys. To create the file (CSV table), I used the following Python script:

```
import numpy as np

A_max = 25
padding = 0.5

ll = np.arange(5,10,0.1)
TT = np.arange(0.22,0.66,0.02)
dd = []
for l in ll:
    dd.append((A_max/(l+2*padding))-2*padding)

f = open("parametricSetup.csv","w")
f.write("*,l,d,T\n")
row = 1
for T in TT:
    for i in range(0, len(ll)):
        f.write('%d,%.6fmm,%.6fmm,%.6fmm\n' % (row, ll[i], dd[i], T))
        row=row+1
f.close()
```

Results are in figure 9.2. The "Constraints" line marks the area in which there is not enough space between tracks ($d - 2T < 0.5$ mm)

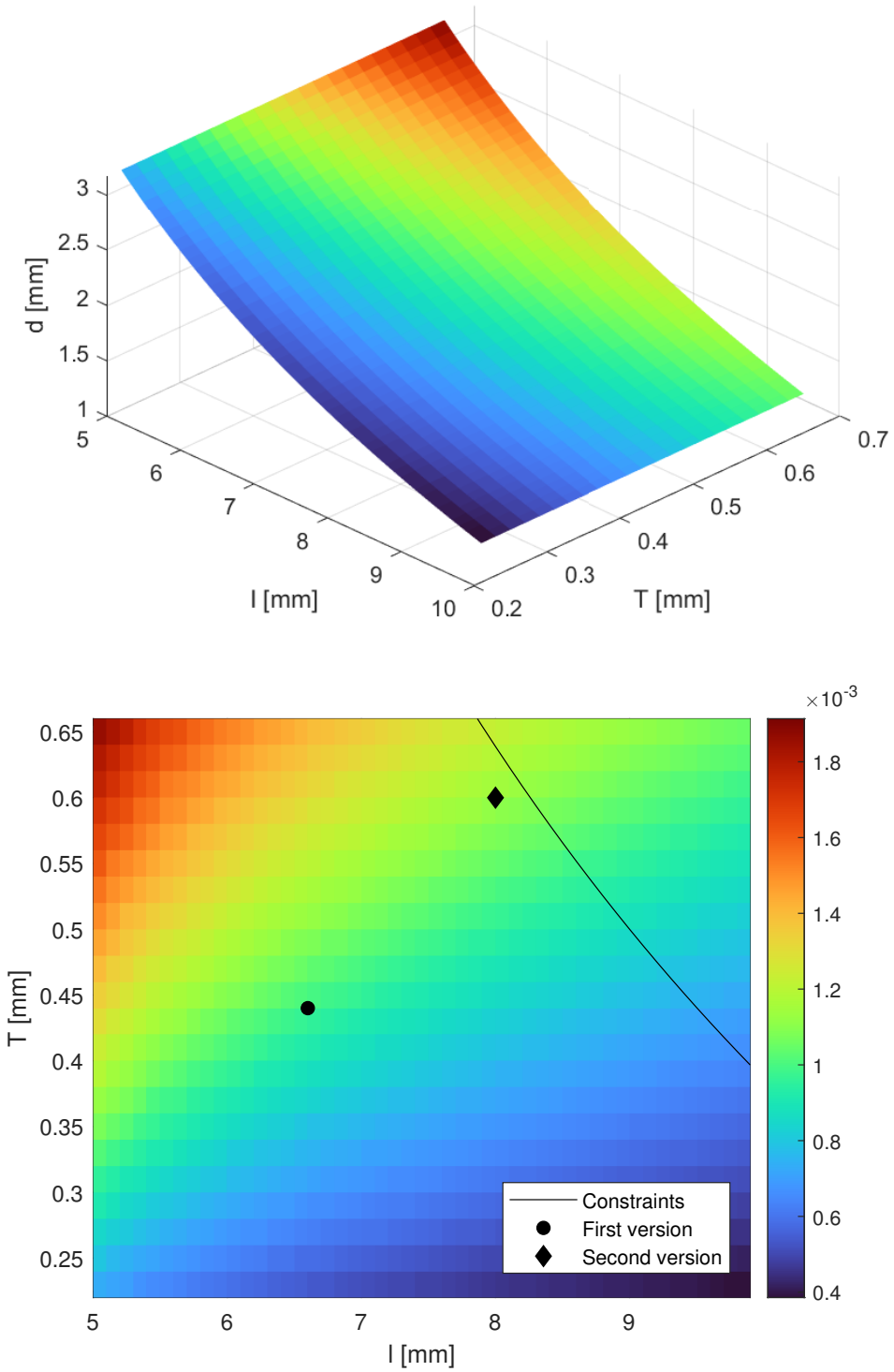


**Figure 9.2:** Demagnetization factor of straight segment

## 9.3 Relation between Core Dimensions and Sensitivity

So far, we have been investigating the demagnetization factor of the racetrack core. However, the final goal is to optimize the sensor's sensitivity, which depends not only on demagnetization but also on the cross-sectional area of the track. To determine the effect on sensitivity, I used the following equation from a book by Ripka [30, p. 60]:

$$V_i = NA\mu_0 H_{ext} \frac{1-D}{(1+D(\mu_r(t)-1))^2} \frac{d\mu_r(t)}{dt} \tag{9.1}$$

Parameters $N$, $\mu_0$ and $H_{ext}$ are constant and thus can be omitted. The area can be expressed as $A = T \cdot thickness$, where thickness can also be omitted.

$$V_i \cong T \cdot \frac{1-D}{(1+D(\mu_r(t)-1))^2} \frac{d\mu_r(t)}{dt} \tag{9.2}$$

While there is a clear linear dependency on $T$, the $D$ cannot be factored out. The $\frac{d\mu_r(t)}{dt}$ is nonzero only when the core is reaching saturation ($\mu$ is changing from material's permeability to $\mu_0$). For this reason, $\mu_r(t)$ cannot be considered a constant in the expression.

### 9.3.1 Average Permeability Method

The book by Ripka [30, p. 61] suggests using $\mu_r(t) = 1000$ as some kind of effective value for the calculation. However, this selection is not justified in any way and seems to be arbitrary. According to computations shown in figure 9.4, the behavior of the system changes dramatically around that particular value. Therefore, the value of 1000 is not useful at all. Kubik, in his thesis[8], did a simulation with sine-wave excitation and got an average value of 10 000. This could suggest that it is safe to assume that the relevant value of $\mu_r(t)$ is above 5000, and the trend is not changing much in that range.

A transient simulation was used to understand the effect of the track-width on sensitivity. Results (using the microfluxgate version 1 structure, 400 $mA_{pp}$, 100 kHz) are shown in figure 9.3. Sensitivity for $T = 0.54$ mm is about 40 % higher than at $T = 0.24$ mm. This contradicts the results for $\mu_r(t) > 5000$, which have an opposite trend. Therefore, this method should be deemed unreliable, and more complex solutions must be used instead of this simplification.

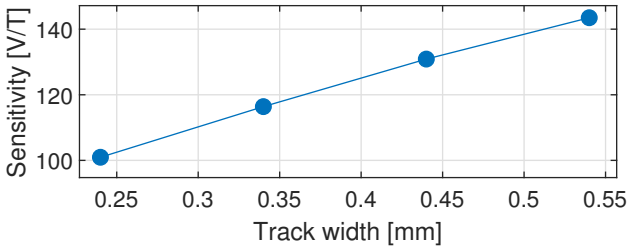


**Figure 9.3:** Effect of variable track-width on sensitivity

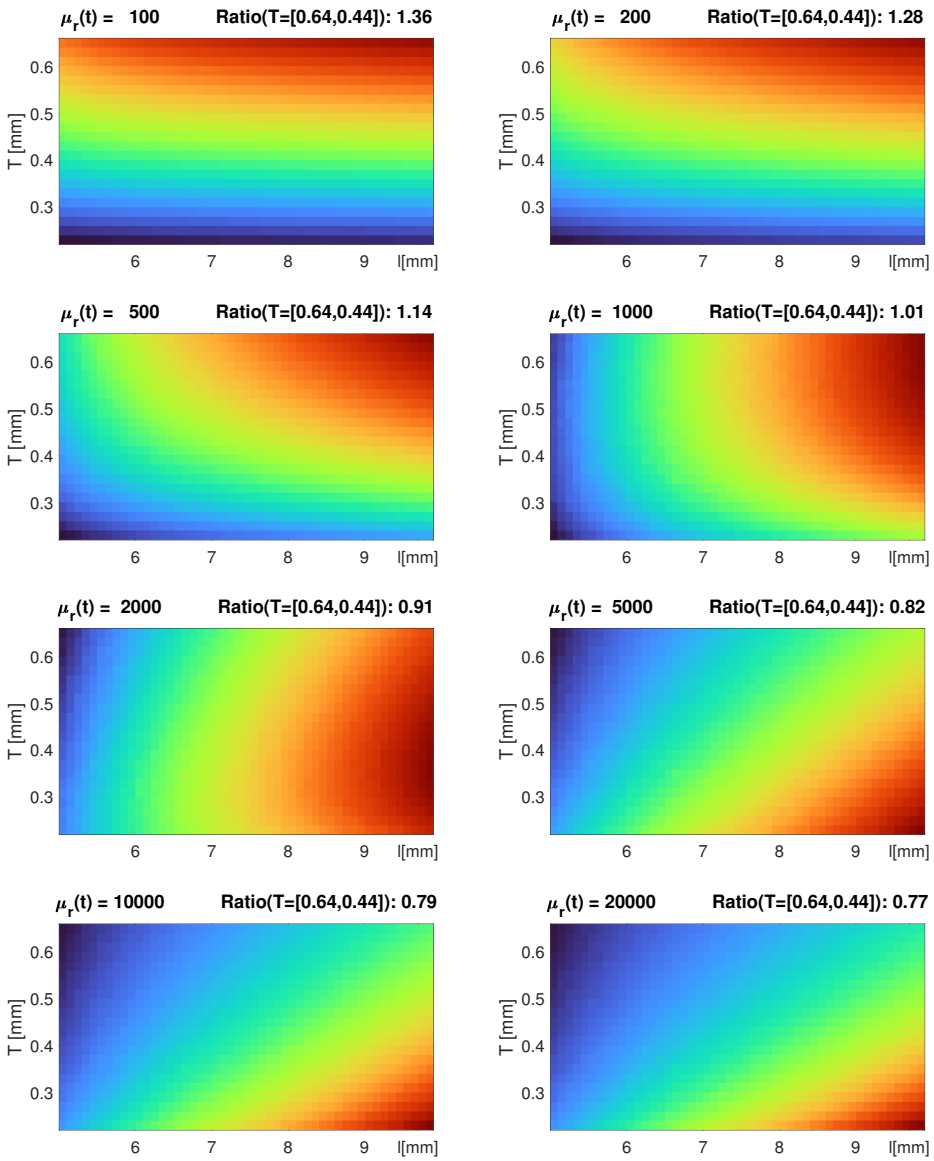


**Figure 9.4:** Prediction of sensitivity based on computation used in the book by Ripka[30, p. 61].

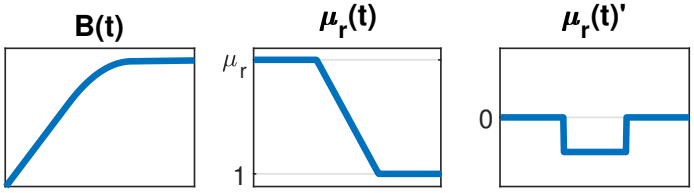


**Figure 9.5:** Model of material saturation used for analyzing sensitivity

### 9.3.2 Predicting Sensitivity Based on Evaluating RMS of Induced Voltage

For evaluating sensitivity, we are interested in a RMS value of (9.2). The derivative $\frac{\mu_r(t)}{dt}$ is only nonzero is small range where $\mu_r(t)$ changes from $\mu_{r_{mat}}$ (permeability of the non-saturated material) to zero. If we assume the most simplified variant of B-H curve, this change happens at a single point, which is useless for this computation. Instead, we can assume linear change as shown in figure 9.5. For simplicity, let us assume that this change happens in a range $t = [0, 1]$:

$$\mu_r(t) = \mu_{r_{mat}} - (\mu_{r_{mat}} - 1)t \tag{9.3}$$

$$\frac{\mu_r(t)}{dt} = -(\mu_{r_{mat}} - 1) \tag{9.4}$$

By substituting (9.3) and (9.4) into (9.2), we can evaluate the RMS value:

$$S \cong \sqrt{\int_0^1 V_i^2 \, dt} = T \cdot \sqrt{\frac{(\mu_{r_{mat}} - 1)^2(-1 + D)^2(3 + (\mu_{r_{mat}} - 1)^2 D^2 + (3\mu_{r_{mat}} - 3)D)}{3(1 + (\mu_{r_{mat}} - 1)D)^3}} \tag{9.5}$$

$\mu_{r_{mat}}$ is the $\mu_r$ of the material, which is constant. Therefore, this equation can be easily evaluated. Result are shown in figure 9.6 on page 55. The trend is almost independent of $\mu_{r_{mat}}$ value (for sensible choice of the value) and is well aligned with the results of the transient simulation (figure 9.3 on page 52). Final results, shown in 9.7 on page 56, are calculated using $\mu_{r_{mat}} = 20\,000$, which is a reasonable choice for the material we use.

### 9.3.3 Optimal Core Dimensions Conclusion

Based on simulations, the following statements can be made about the optimal shape of the core:

- Demagnetization factor decreases with increasing $l$ faster than with increasing $d$. This means that, for a fixed area, it is favourable to increase $l$ over $d$.
- Increasing track width $T$ leads to a higher demagnetization factor, but due to the increase of cross-sectional area, the sensitivity increases.

As the maximum $T$ depends on $d$, It may actually be beneficial to increase $d$ at the cost of lower $l$. However, technological considerations must also be applied to this decision, as discussed in the next section.

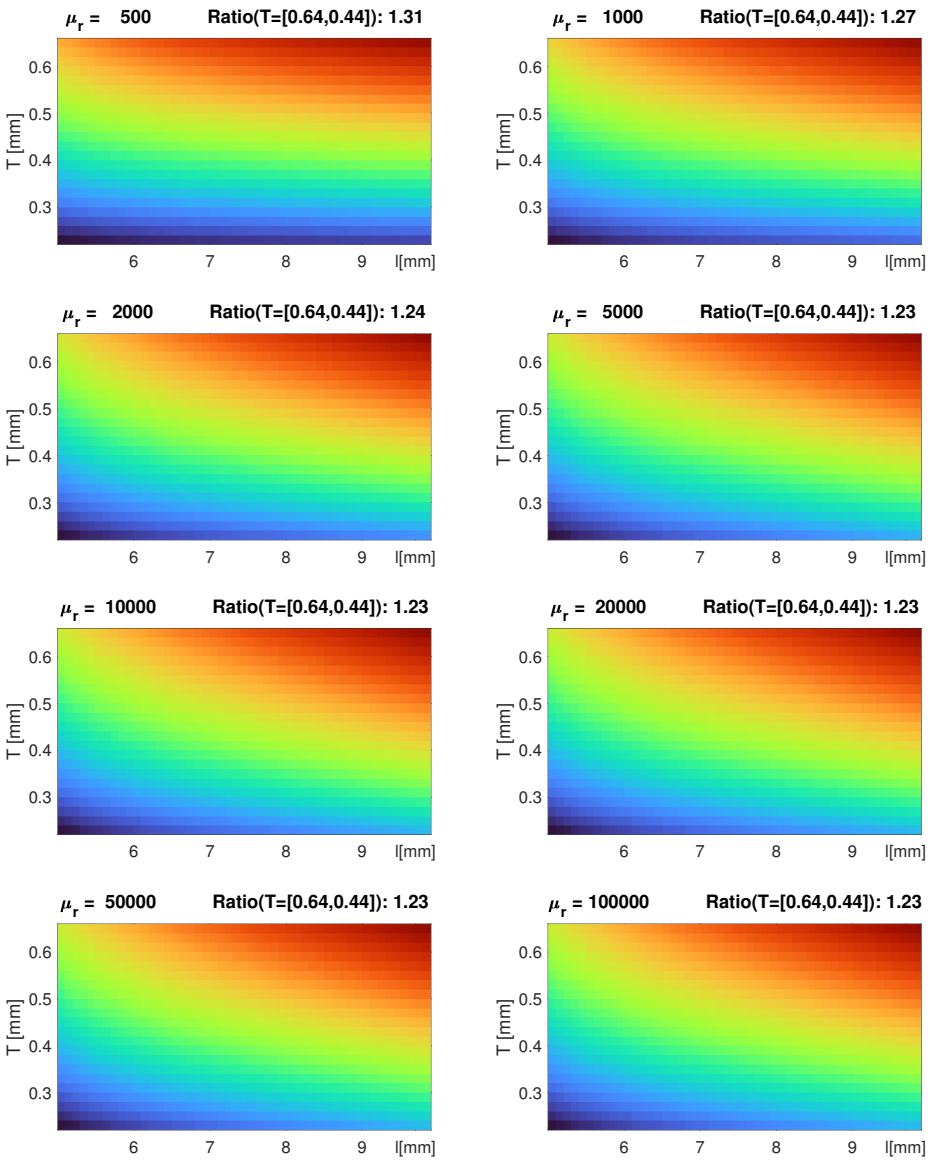


**Figure 9.6:** Prediction of sensitivity based evaluating RMS of induced voltage (section 9.3.2)

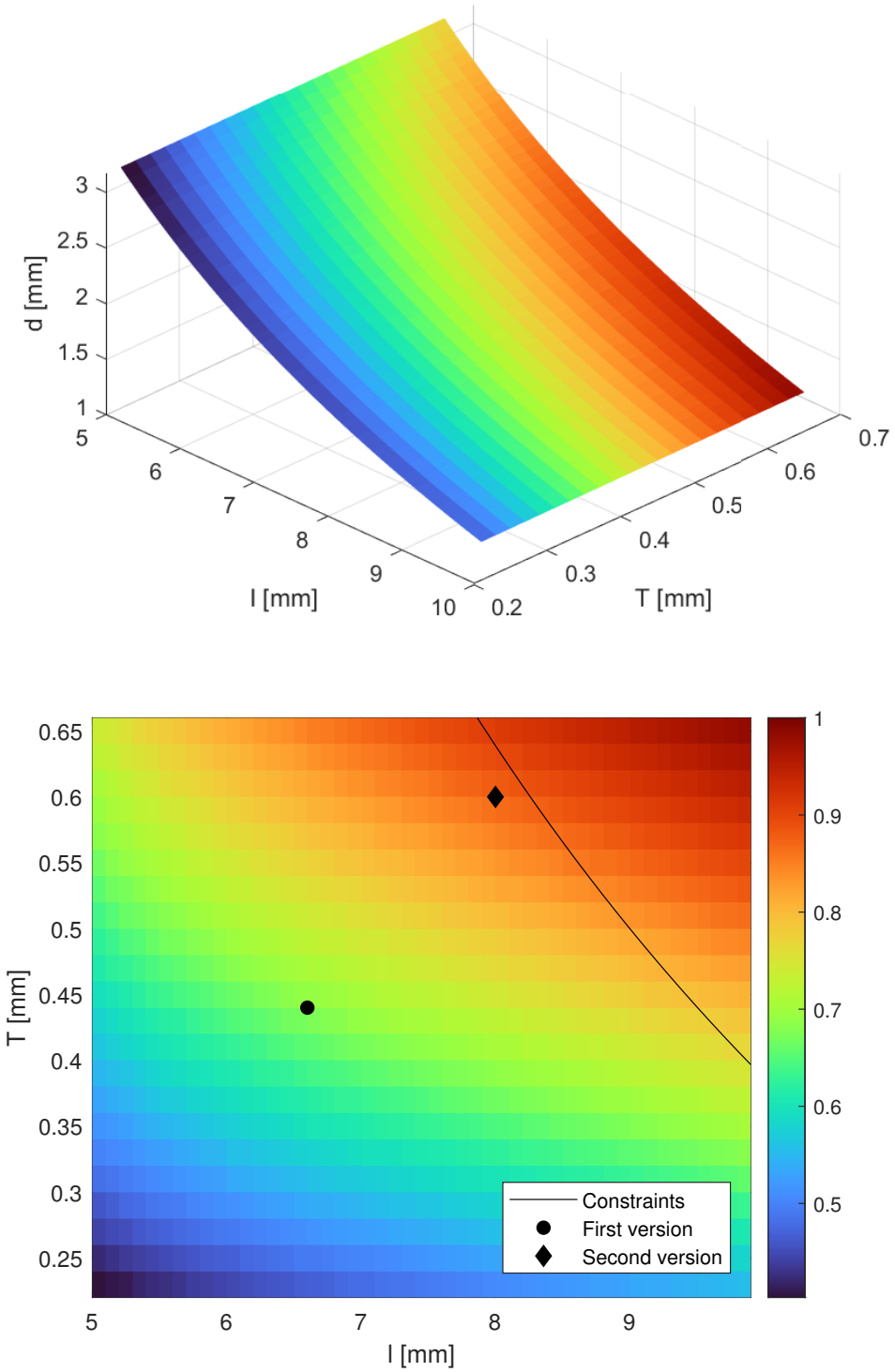


**Figure 9.7:** Predicted sensitivity (relative to highest)

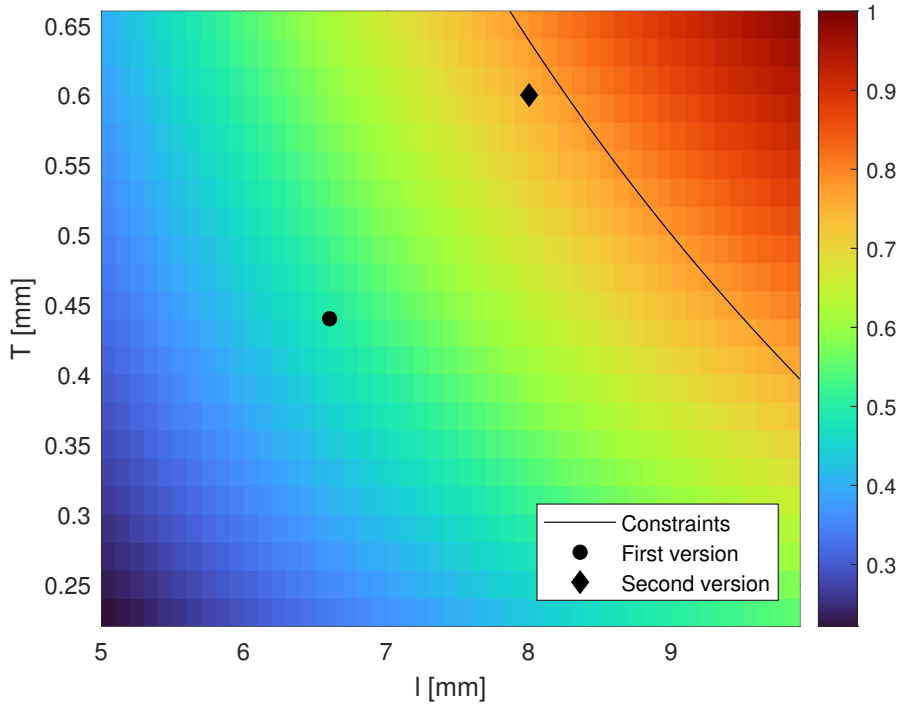


**Figure 9.8:** Predicted sensitivity (relative to highest), including sensing coil turn number linearly proportional to length

## 9.4 Technological Considerations for the Optimization

To optimize the core shape, we should also consider the sensing coil windings. The number of turns of this coil, $N$ in (9.1), is determined by the minimum spacing between the wires and thus is proportional to the length of the straight section of the core. Sensitivity is linearly proportional to this length, as seen from (9.1). In terms of dimension defined for this design, the straight section length equals $l - d$. Using (9.5), we get figure9.8. A Matlab code for this calculation is shown on the next page. This basically tells us that it doesn't matter much whether we use a longer core with a lower width or vice versa as long as we make the track as wide as possible.

**Table 9.1:** Overview of core sizes used for the first and second versions of the micro-fluxgate

| Version | $l$ [mm] | $d$ [mm] | $T$ [mm] | thickness [$\mu$m] | Demagnetization | Sensitivity |
|---|---|---|---|---|---|---|
| 1 | 6.6 | 2.2 | 0.44 | 25 | $1.0 \times 10^{-3}$ | - |
| 2 | 8.0 | 1.75 | 0.6 | 25 | $1.1 \times 10^{-3}$ | +51 % |

```
function [D] = demagnetization(B, H, Hext)
    % B: Average B field in the core
    % H: Average H field in the core
    % Hext:  External H field
    mu0 = 4*pi*1e-7;
    D = (H-Hext)./(H-(B./mu0));
end

function [S] = sensitivity(T,D,m,l)
    % T: track width of the core
    % D: Demagnetization factor
    % m:  Relative permeability of the material
    % l:  length of the core
    S = sqrt((m-1)^2*(-1+D)^2*T^2*l^2*(3+(m-1)^2*D^2+(3*m-3)*D)/(3*(1+(m-1)*D)^3));
end
```

# Chapter 10

# Designing and Fabrication of the Second Version Micro-Fluxgate

The whole design of the second version of the chip was done by myself at NTUST. The technology of choice is TSMC D35. The technology is not very important for the fluxgate chip (which does not contain any transistors and only uses chip's metalization). This choice was motivated mainly by the most favorable schedule of tape-out and chip-out.

## 10.1 Layout

The design flow is similar to that used in the first version. At first, I drew the layout in KiCAD because that is more convenient than using chip layout EDA tools. The size and spacing of bonding pads are the same as in the first version. The main difference is the shape of the core. Due to the much narrower space on the internal side of the core, placing the excitation coils on the rounded ends would not be practical. Instead, the excitation coil is placed at the ends of straight segments. The device has 20 turns of excitation coil and 60 turns of sensing coil.

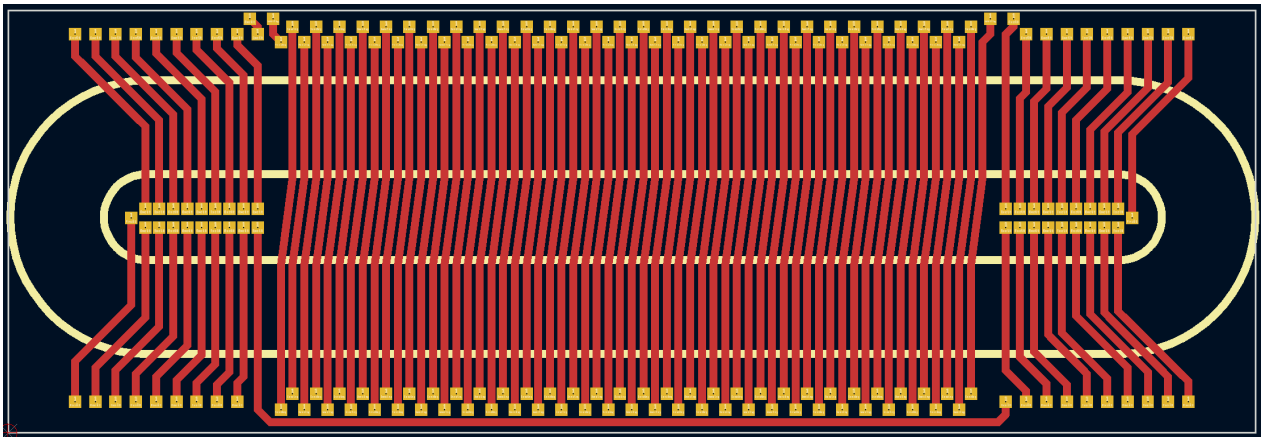

**Figure 10.1:** Layout of Micro-Fluxgate version 2 (pads and metal)

### 10.1.1 Chip Layout

The Cadence Virtouso EDA tool was used to design a proper layout in the given technology. These tools were provided by TSRI in a virtual machine environment called EDA Cloud. Details about the technology are confidential to the TSMC and TSRI, so I cannot go into much detail. No data are allowed to be exported from the remote virtual machine to my computer, so it was not possible to get images of the layout.

Instead of attempting to directly convert polygons from the KiCAD layout to Cadence (as done with the first version), I only copied the positions of bonding pads and drew the metal patch from scratch. The D35 technology provides 4 metal layers. The top two were used in parallel for the connection. Design rules limit the maximum width of metal. The limit is around half of the intended width, so each connection uses two parallel paths (figure 10.4b). A standard library cell was used for the bonding pads. Metal 1, Metal 2, and Poly layers were partially filled by rectangles to meet the minimum density rule.

The core was designed with regards to the same 25 $\text{mm}^2$ size as the first version. However, due to the different position of the excitation coil, there is no padding needed at the ends of the core. The final dimensions of the chip are thus smaller:

$$8 \text{ mm} \times 2.7 \text{ mm} = 21.6 \text{ mm}^2$$

## 10.2 Simulation

Simulation was done using a similar setup as in the case of the first version. The only difference is the shape and position of the coils.

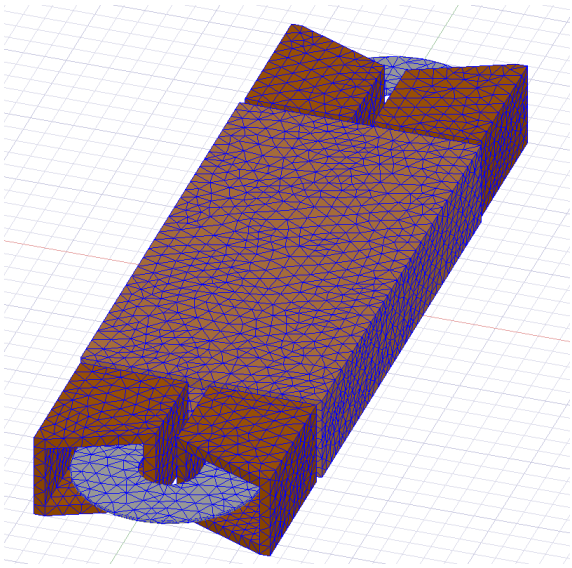

**Figure 10.2:** Simulation model of Microfluxgate version 2

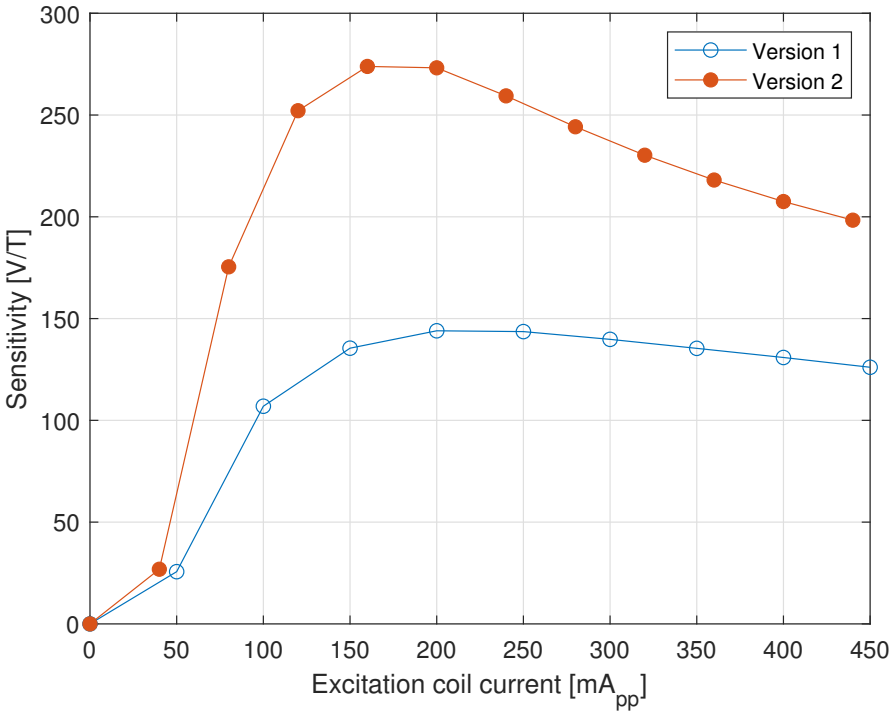


**Figure 10.3:** Simulation results of version 2 compared to version 1

### 10.2.1 Simulation Results

The result shows a 90% increase in sensitivity. While this is partially thanks to the increase of pickup coil turns from 50 to 60, around 60% increase can be attributed to the optimized core. The decrease of optimal excitation current corresponds to expectations given the higher number of excitation coil turns.

**Table 10.1:** Comparison of micro-fluxgate version 1 and 2 simulated sensitivity at 100 kHz excitation

| Version | Chip area [mm$^2$] | $N_{excit}$ | $N_{pickup}$ | $I_{excit}$ [mA] | Sensitivity [V/T] | [V/T/turn] |
|---|---|---|---|---|---|---|
| 1 | 24.3 | 30 | 50 | 200 | 145 | 2.9 |
| 2 | 21.6 | 40 | 60 | 160 | 275 | 4.6 |

## 10.3 Assembly

The same company fabricated the core as in the case of the first version. This time, they used laser cutting instead of etching. The quality is similar, but the edges are rough in some parts (figure 10.4c).

The assembly process was successful this time. The bonding company suggested increasing the clearance between the core and pads on the outer side of the core in future versions.

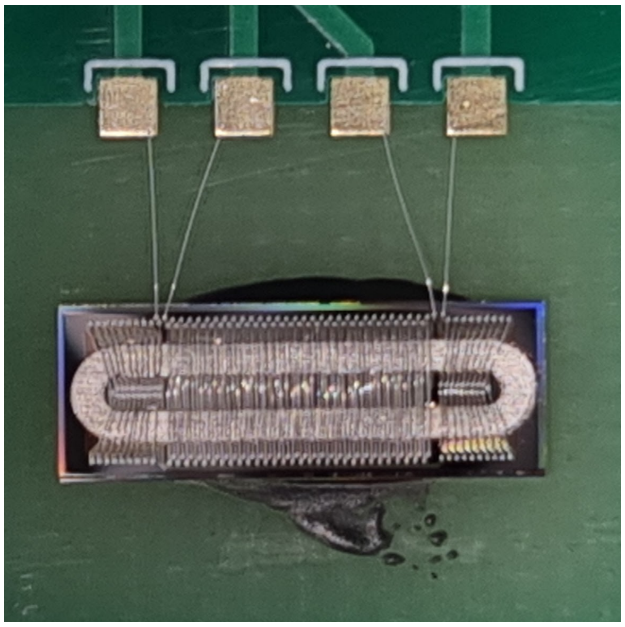

**(a) :** Assembled micro-fluxgate device

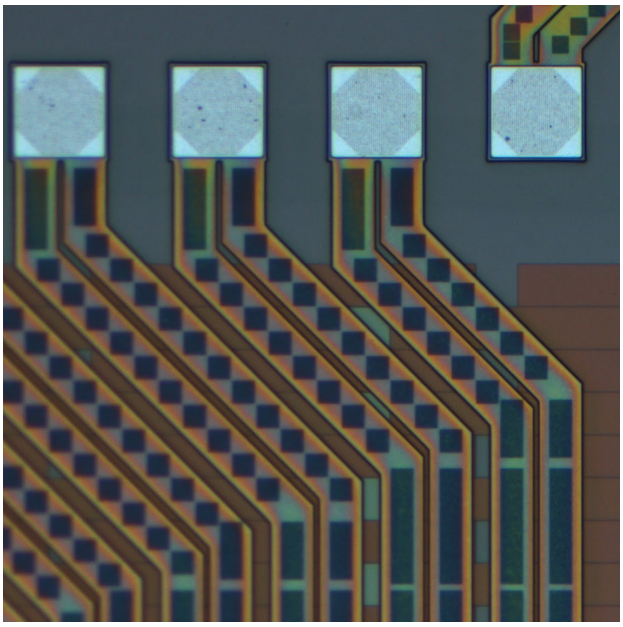

**(b) :** Bonding pads and metal paths

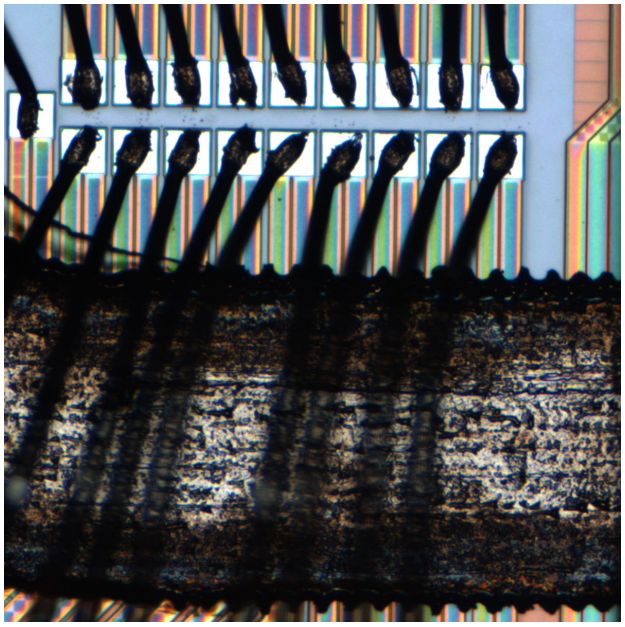

**(c) :** Core and wire bonding

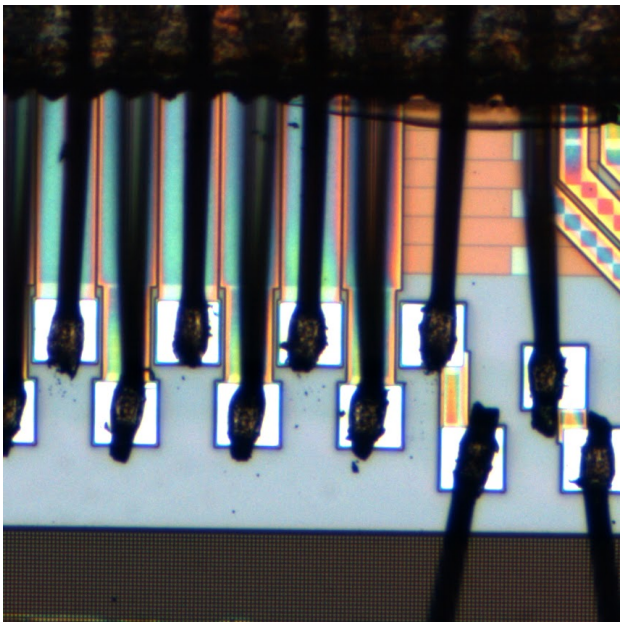

**(d) :** Wire bonding

**Figure 10.4:** Photos of micro-fluxgate version 2

# Chapter 11

# Measurements and Results of Micro-Fluxgate Version 2

Five devices were assembled. Three of them were covered in epoxy for protection, and two were left uncovered. Resistances of sensing and excitation coils were measured as a basic test of functionality:

**Table 11.1:** Resistance measurements of coils

| Resistance | Uncovered | | Covered in epoxy | | |
|---|---|---|---|---|---|
| Excitation coil | 20.4 Ω | 20.3 Ω | 20.7 Ω | ∞ | ∞ |
| Sensing coil | 59.0 Ω | 59.0 Ω | 60.1 Ω | ∞ | ∞ |

The two uncovered devices are operating correctly. Only one of the three epoxy-covered devices was functional, and it failed two weeks later. It is likely that the epoxy has partially delaminated from the PCB by thermal or mechanical stress and damaged the bonding wires.

## 11.1 Coil power dissipation and temperature

According to simulations, the optimal sensitivity can be expected at an excitation current around 200 mA peak-peak. This corresponds to an RMS value of around 70 mA. Power dissipation will be around 100 mW. Higher current may be needed at higher frequencies. A test was performed using DC current to estimate coil temperature based on the resistance of the (aluminium) wires. The linear temperature coefficient of aluminium's resistivity is 0.00429 [31].

**Table 11.2:** Excitation coil temperature depending on current

| RMS Current [mA] | 0 | 116.6 | 170.1 |
|---|---|---|---|
| Voltage [V] | 0 | 3.0 | 5.6 |
| Power [mW] | 0 | 347 | 947 |
| Resistance [Ω] | 20.3 | 25.5 | 32.7 |
| Temperature above ambient [°C] | 0 | 60 | 143 |

At the maximum tested DC current (corresponding to the RMS value of around 480 mA peak-peak sinewave), the power dissipation is almost 1 W, and the temperature reaches around 165°C. However,

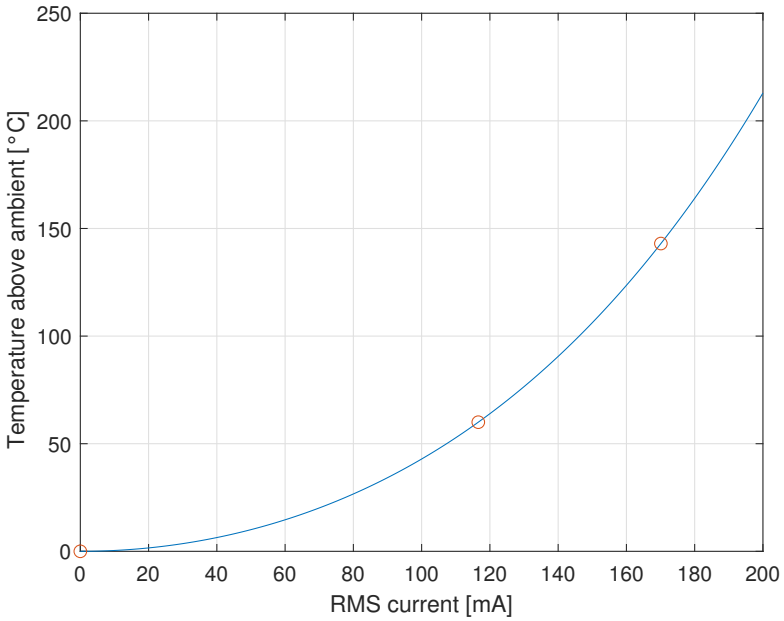


**Figure 11.1:** Excitation coil temperature

the realistic range of operating current is significantly less than the tested maximum. At 117 mA RMS (330 mA peak-peak sinewave), the coil temperature is around 80°C, which is acceptable.

Interpolating the measured points is a challenging task. It can be generally stated that the temperature is linearly proportional to dissipated power. Power can be calculated as $I = RI^2$, suggesting a quadratic relation between current and temperature. However, this assumes constant resistance, which is clearly not the case here. Because of the increasing resistance, the real trend grows faster than the second power. The interpolation in figure 11.1 uses a four-order polynomial. The two measured data points were mirrored in even symmetry to get enough points for the interpolation.

## 11.2 Measurement Setup

The measurement requires placing the fluxgate sensor in a known magnetic field. Helmholtz coil is typically used for this. No Helmholtz coil was available to me, so I constructed my own. It consists of a hollow styrofoam cylinder and two hand-wound coils, 20 turns each. The radius of the coils is 68 mm. Using the equation (7.2), the field inside is 264 $\mu$T/A. The coil is placed vertically (the field created by the coil is parallel to the vertical component of Earth's magnetic field). The vertical position can be set more reliably and repeatably than the north-south direction.

The vertical component of Earth's magnetic field at the laboratory location (Taipei) is 27.8 $\mu$T[27]. According to the sensor's output, the field is nullified by applying 140 mA to the Helmholtz coil. This would suggest that the conversion factor of the coil is slightly lower (200 $\mu$T/A). The similarity of the calculated and tested values rules out any mistake in using the equation (such a mistake would

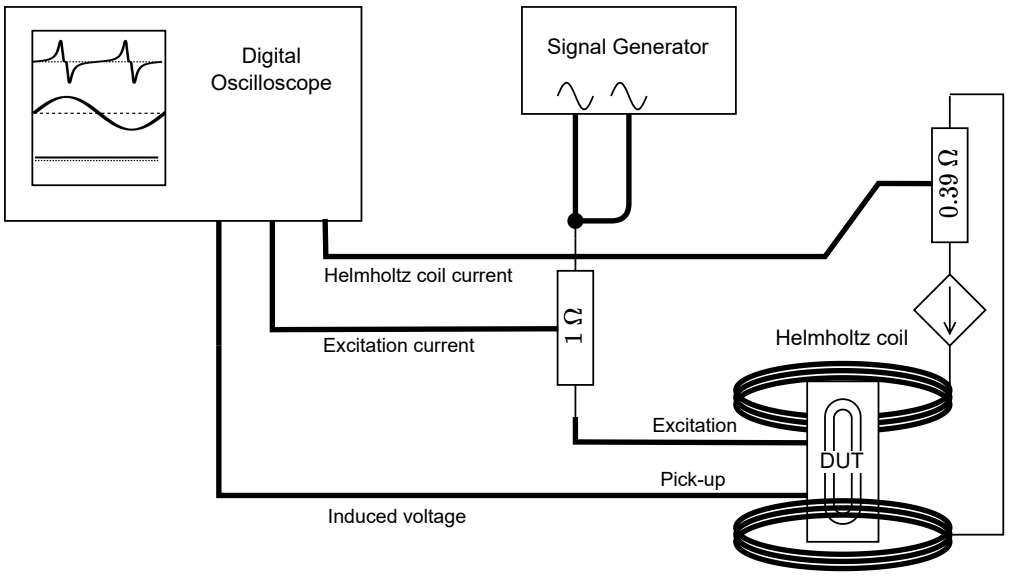


**Figure 11.2:** Setup for measuring sensitivity and linearity of a fluxgate (schematic)

more likely lead to twice or half the value). The calculated value is assumed to be more reliable than the magnetic field inside a building because it may be influenced by metal in its construction.

The excitation current, as well as the current in the Helmholtz coil, is measured using a shunt resistor by a digital oscilloscope. The induced voltage waveform is also captured by an oscilloscope, and the processing is then done digitally using the algorithm described in section 4.1.1. The instruments used are Tektronix AFG3022B, Tektronix DPO7254C, and Gwinstek GPS-3303.

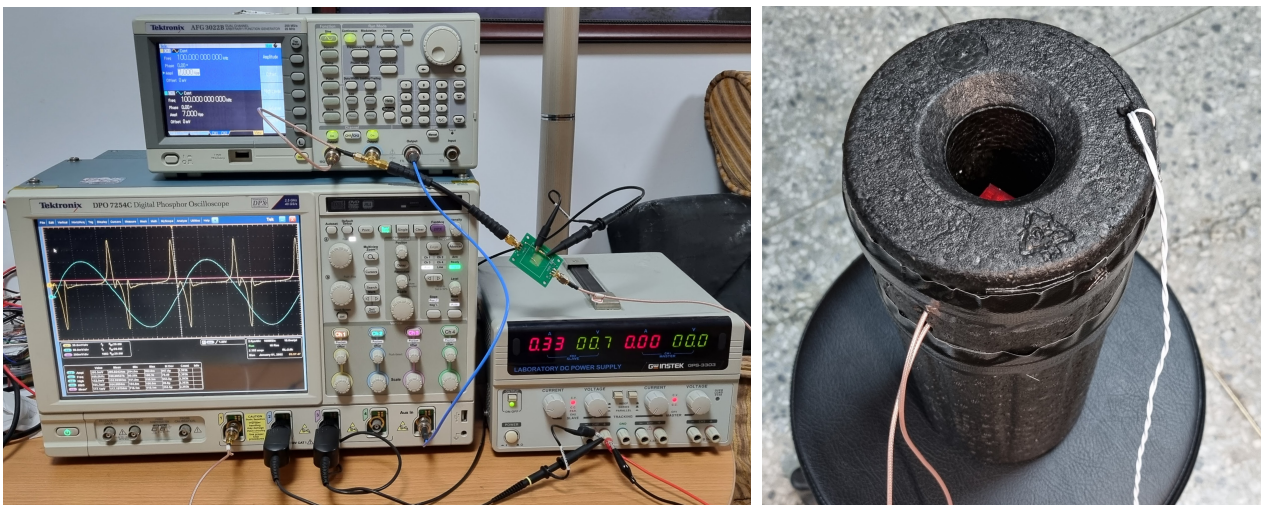

**(a) :** Instruments **(b) :** Helmholtz coil

**Figure 11.3:** Setup for measuring sensitivity and linearity of a fluxgate (photo)

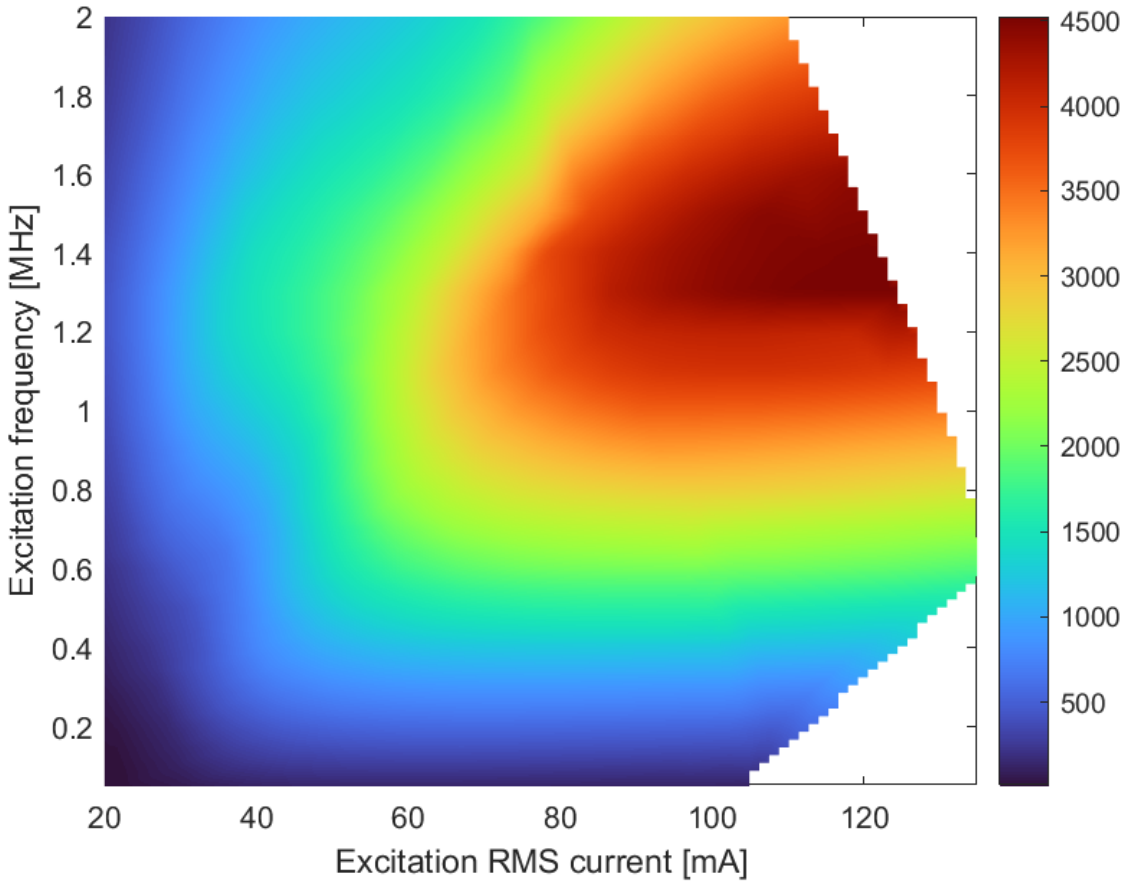


**Figure 11.4:** Sensitivity dependence on excitation current and frequency (sinewave excitation)

## 11.3 Sensitivity Measurement

Finding the highest sensitivity is a 2D optimization task. Figure 11.4 shows sensitivity evaluated at more than 400 points at different excitation signals ranging from 100 mA to 370 mA peak-peak current and 100 kHz to 2 MHz frequency. Maximum current reachable at high frequencies (top-right corner of the plot) is limited by the output impedance of the signal generator. The optimum is found at 1.3 MHz and 330 mA with a sensitivity of 4440 V/T. Measurement was done in 50 $\mu$T field.

The sensitivity grows linearly until around 1.3 MHz, where the maximum occurs. After 1.4 MHz, the sensitivity begins to decrease. This is because of parasitic capacitance and eddy currents in the core [30]. The current needed for maximum sensitivity increases with the frequencies. This is likely also caused by the eddy currents, as briefly explained in [8]. Comparison of low and high-frequency waveforms in figure 11.6 show that the higher harmonics are significantly suppressed at 1 MHz frequency. The output signal mainly contains the second harmonics only, which suggests that a resonance occurs on the sensing coil thanks to the parasitic capacitance. This effect is positive, as it increases sensitivity.

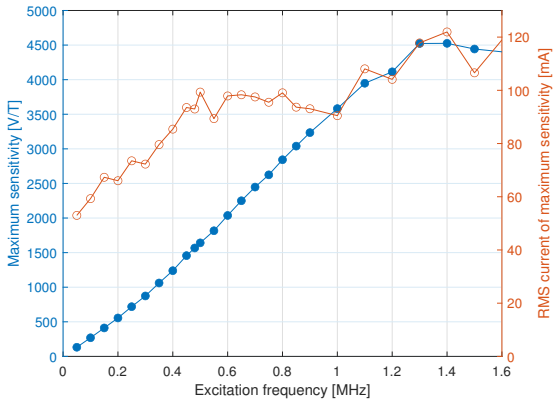


**(a) :** Slice along points of maximum sensitivity

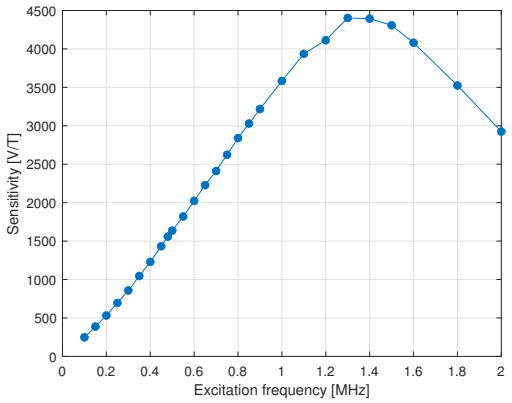


**(b) :** Slice at 100 mA RMS (280 $mA_{pp}$)

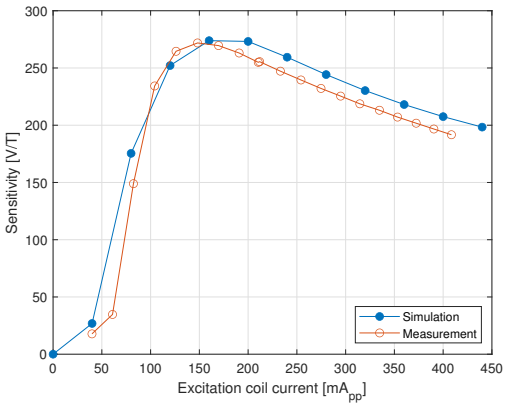


**(c) :** Slice at 100 kHz compared to simulation

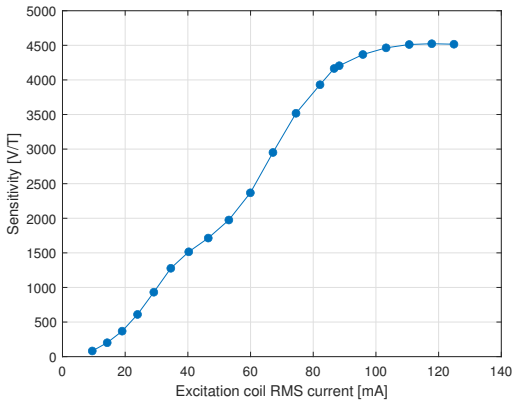


**(d) :** Slice at 1.3 MHz

**Figure 11.5:** Slices through the 2D sensitivity plot (figure 11.4)

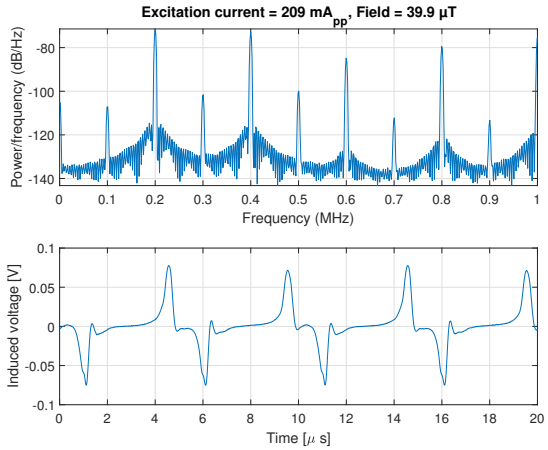


**(a) :** 100 kHz

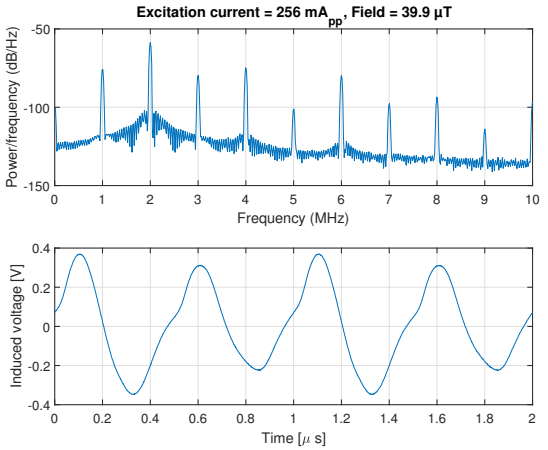


**(b) :** 1 MHz

**Figure 11.6:** Spectrum and time domain of induced voltage (sinewave excitation)

## 11.4 Linearity

Linearity was evaluated at the point of maximum sensitivity. The linear range is ±200 $\mu$T with non-linearity less than 0.5 % of the range. There is an abrupt change in linearity at −28 $\mu$T, where the current in the Helmholtz coil changed direction (figure 11.7b). Changing the direction required mechanically changing connections, which influenced the measured values slightly.

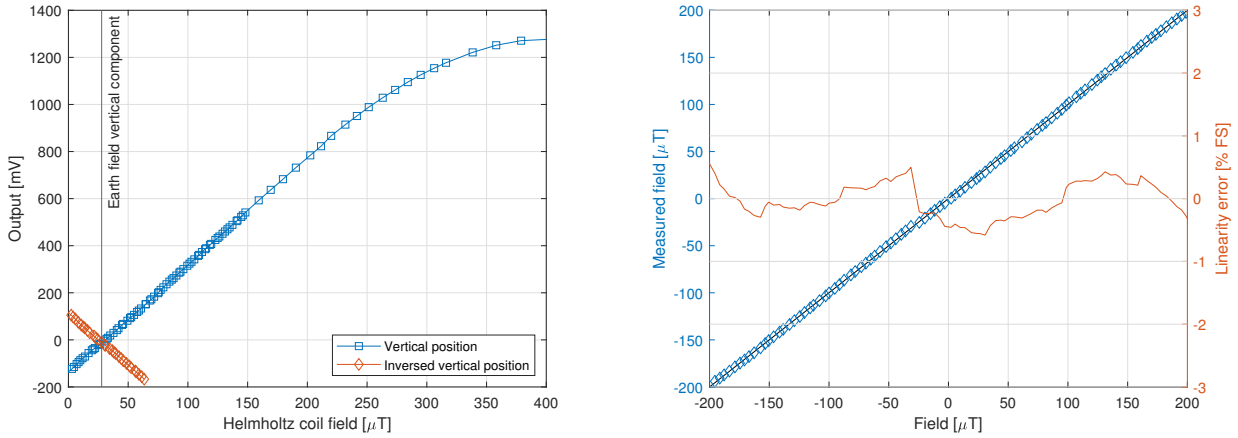


**(a) :** Wide range

**(b) :** Linear range

**Figure 11.7:** Linearity at 1.3 MHz 330 $mA_{pp}$ sinewave excitation

### 11.4.1 Offset

Precisely measuring the offset would require magnetic shielding. Such equipment was not available to me at the time. To get an approximate value of offset, I used the following approach:

1. Measure output signal at various low fields (as in linearity measurement)
2. Position the Helmholtz coil with the sensor inside upside-down and flip the direction of current in the Helmholtz coil.
3. Repeat the measurement in the inverted position (orange graph in figure 11.7a)
4. Interpolate both measurements by linear
5. Calculate the field generated by the Helmholtz coil at which the output transitions zero
6. The offset is half of the difference between the zero-crossing of normal and inverted position

The offset evaluated by this method is 2.4 $\mu$T.

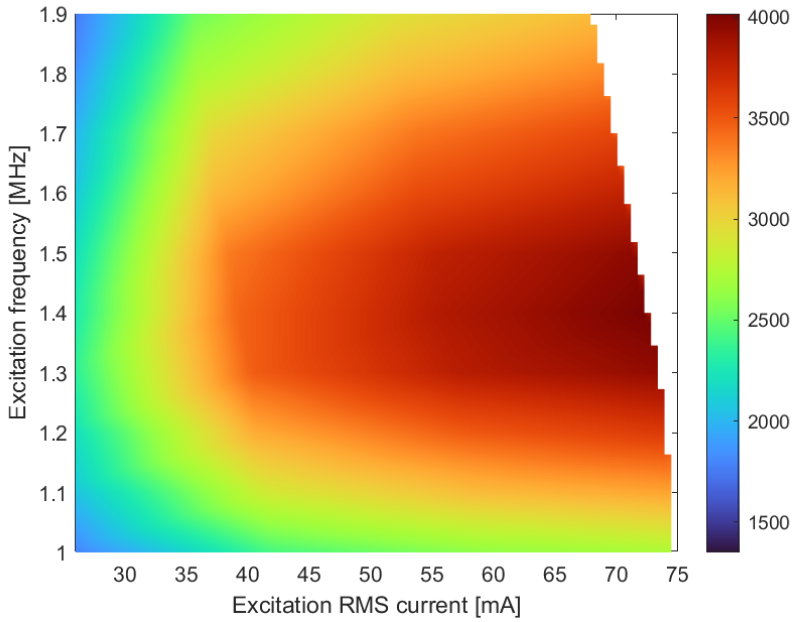


**Figure 11.8:** Sensitivity dependence on excitation current and frequency (20% duty pulse excitation)

## 11.5 Pulse Excitation

The pulse excitation method, introduced in [14] to reduce power consumption, was also briefly tested. As shown in figure 11.8, using 20% duty cycle pulses can achieve sensitivity comparable to the sinewave excitation while reducing RMS current by almost half. Non-linearity is less than 1% in $\pm 150$ $\mu$T rance, which is worse than in the case of sinewave excitation.

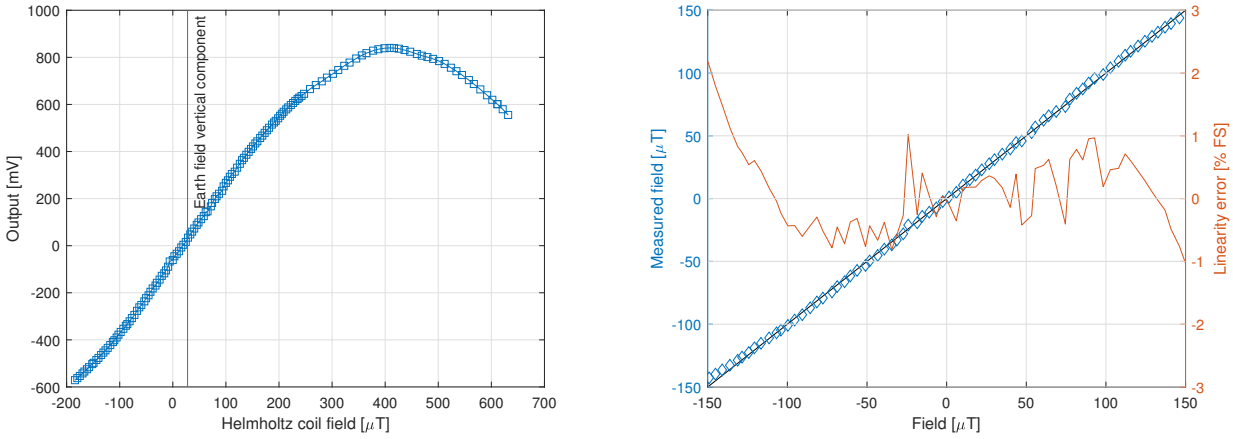


**(a) :** Wide range **(b) :** Linear range

**Figure 11.9:** Linearity at 1.4 MHz 70mA$_{\mathrm{RMS}}$ 20% duty pulse excitation

# Chapter 12

# Conclusion

Despite the failure of the first version of micro-fluxgate, the second version was successful. Totaly five devices were assembled. While the placement of the metal core and the wire bonding were successful, three of those devices were damaged by epoxy covering the chip. The remaining two devices were left without epoxy cover and remain functional to this date (2 months after fabrication at the time of writing this).

The chip has dimensions of 8 mm × 2.7 mm = 21.6 mm$^2$. The device uses a "racetrack" shaped core made of VITROVAC 6025 F amorphous metal. The length and width of the core are 8 mm × 1.75 mm. The excitation coil has 40 turns in total, and the sensing coil has 60 turns.

Measurements were performed using available instruments. Sensitivity, linearity, and offset were measured. Equipment for the measurement of noise characteristics was not available to me. In open-loop operation, the sensor achieves a sensitivity of 4440 V/T, which is higher than other micro-fluxgate sensors. Especially compared to designs that use planar sensing coils. The open-loop linearity range is ±200 $\mu$T with less than 0.5% nonlinearity in this range. Offset was evaluated as 2.4 $\mu$T. However, specialized equipment (magnetic shielding, lock-in amplifier) would be required to measure the offset precisely.

**Table 12.1:** Comparison of measured parameters to other works in this field

| | This work | Jian Lei[24] | Lei Guo[22] | DRV425[17] | Lu[16] |
|---|---|---|---|---|---|
| Sensitivity [V/T] | 4440 | 327 | 1985 | 250 | 7 |
| per turn [V/T/turn] | 74 | 13 | - | - | 0.01 |
| Linearity | 0.5 % | 5 % | - | - | 2 % |
| in range [$\mu$T] | 200 | 300 | 1000 | - | 400 |
| Excitation frequency [kHz] | 1300 | 100 | 500 | 500 | 1000 |
| Excitation current [mA] | 110 | 150 | 70 | - | 60 |
| Power dissipation [mW] | 340 | 34 | - | - | 36 |
| Offset [$\mu$T] | 2.4 | - | - | 2 | - |
| Size [$mm \times mm$] | 2.7×8 | 3×4 | 2.7×7.3 | 4×4 | 1.75×3.5 |
| area [mm$^2$] | 21.6 | 12 | 19.7 | 16 | (2×) 6.1 |

The optimal sensitivity requires around 110 mA RMS current. At this current, the power dissipation is 340 mW, and the coil heats around 60°C above ambient temperature. Pulse excitation was briefly tested as a method of reducing power consumption. Results show that reducing the power consumption by half should be possible while maintaining the sensitivity. However, properly determining the optimal pulse excitation signal is beyond the scope of this work, and further research may lead to even better results.

## 12.1 Achieved Objectives

All objectives of this thesis were accomplished successfully. A few of the most important achievements can be highlighted:

- Simulation model was developed to accurately predict the performance of the micro-fluxgate sensor using FEM transient simulation. Properties of the material were measured and processed carefully to avoid glitches in the simulation. Simulation model accuracy was verified by measuring an upscaled model of the proposed fluxgate structure and later compared to measurements of the micro-fluxgate. The model accurately predicted the sensitivity of the sensor as well as the excitation current required to reach the optimal sensitivity.
- Magnetostatic FEM simulation was used to optimize the demagnetization factor of the core. The sensor using the proposed optimized shape of the core exhibited 90% higher sensitivity than the original design (according to simulation at 100 kHz excitation).
- Two versions of the micro-fluxgate chip were designed. The latter of them was successfully fabricated and assembled. Measurement shows satisfying performance.

## 12.2 Issues for Further Research

Additional suggestions, which are beyond the scope of this thesis, can be proposed for further research:

- Investigate why the epoxy-covered micro-fluxgate chips fail and find a solution. While the non-covered chips work flawlessly so far, it can be expected that they will fail in a few months due to oxidation.
- Perform more advanced measurements, which were not possible yet due to a lack of specialized instruments. This includes noise characteristics, perming error, more precise offset measurement, and stability of offset and gain.
- More profound research into pulse excitation is needed to optimize the device's power consumption. Different duty cycles and shapes of pulses can be tested.
- Use a parallel capacitor on the sensing coil to increase sensitivity using resonance.

# Bibliography


[1] P. Ripka. "Review of fluxgate sensors". In: *Sensors and Actuators A: Physical* 33.3 (June 1992), pp. 129–141.

[2] T. M. Liakopoulos and C. H. Ahn. "Micro-fluxgate magnetic sensor using micromachined planar solenoid coils". In: *Sensors and Actuators A: Physical* 77.1 (Sept. 1999), pp. 66–72.

[3] Ugur Topal and Hava Can. "Design of Ring Core Fluxgate Magnetometer as Attitude Control Sensor for Low and High Orbit Satellites". In: *Journal of Superconductivity and Novel Magnetism* 28 (Jan. 2015). DOI: 10.1007/s10948-014-2788-5.

[4] J. Lenz and A. S. Edelstein. "Magnetic sensors and their applications". In: *IEEE Sensors Journal* 6.3 (June 2006), pp. 631–649.

[5] Kaixin Yuan et al. "Ring-Core Fluxgate Sensor for High Operation Temperatures up to 220 °C". In: *Micromachines* 13.12 (2022). ISSN: 2072-666X. DOI: 10.3390/mi13122158. URL: https://www.mdpi.com/2072-666X/13/12/2158.

[6] Pavel Baranov, Vitalia Baranova, and Nesterenko Tamara. "Mathematical model of a fluxgate magnetometer". In: *MATEC Web of Conferences* 158 (Jan. 2018), p. 01006. DOI: 10.1051/matecconf/201815801006.

[7] Mattia Butta. "Orthogonal Fluxgate Magnetometers". In: vol. 19. Sept. 2017, pp. 63–102. ISBN: 978-3-319-34068-5. DOI: 10.1007/978-3-319-34070-8_3.

[8] J. Kubík. *Printed Circuit Board Fluxgate Sensors*. 1st ed. Prague: Shaker Verlag, 2009. ISBN: 978-3-8322-7740-6.

[9] J. Kubík and P. Ripka. "Racetrack fluxgate sensor core demagnetization factor". In: *Sensors and Actuators A: Physical* 143.2 (2008), pp. 237–244. ISSN: 0924-4247. DOI: https://doi.org/10.1016/j.sna.2007.10.066. URL: https://www.sciencedirect.com/science/article/pii/S0924424707008084.

[10] Chih-Cheng Lu et al. "High-Sensitivity Low-Noise Miniature Fluxgate Magnetometers Using a Flip Chip Conceptual Design". In: *Sensors* 14.8 (2014), pp. 13815–13829. ISSN: 1424-8220. DOI: 10.3390/s140813815. URL: https://www.mdpi.com/1424-8220/14/8/13815.

[11] S. Kawahito et al. “A fluxgate magnetic sensor with micro-solenoids and electroplated permalloy cores”. In: *Sensors and Actuators A: Physical* 43.1 (1994), pp. 128–134. ISSN: 0924-4247. DOI: https://doi.org/10.1016/0924-4247(93)00679-X. URL: https://www.sciencedirect.com/science/article/pii/092442479300679X.

[12] Shoji Kawahito et al. “High-resolution micro-fluxgate sensing elements using closely coupled coil structures”. In: *Sensors and Actuators A: Physical* 54.1 (1996), pp. 612–617. ISSN: 0924-4247. DOI: https://doi.org/10.1016/S0924-4247(97)80024-6. URL: https://www.sciencedirect.com/science/article/pii/S0924424797800246.

[13] P. Ripka et al. “Micro-fluxgate sensor with closed core”. In: *Sensors and Actuators A Physical* A91 (Feb. 2001), pp. 65–69. DOI: 10.1016/S0924-4247(01)00481-2.

[14] P. Ripka et al. “Pulse excitation of micro-fluxgate sensors”. In: *IEEE Transactions on Magnetics* 37.4 (2001), pp. 1998–2000. DOI: 10.1109/20.951033.

[15] Chih-Cheng Lu et al. “Design, Fabrication, and Characterization of a 3-D CMOS Fluxgate Magnetometer”. In: *Magnetics, IEEE Transactions on* 47 (Nov. 2011), pp. 3752–3755. DOI: 10.1109/TMAG.2011.2158409.

[16] Chih-Cheng Lu et al. “Hybrid Microfluxgate and Current Transformer Sensor”. In: *IEEE Transactions on Magnetics* 58.8 (2022), pp. 1–5. DOI: 10.1109/TMAG.2022.3157052.

[17] Texas Instruments. *DRV425 Fluxgate Magnetic-Field Sensor*. Revised March 2016. Originally published October 2015. Texas Instruments. Mar. 2016. URL: https://www.ti.com/product/DRV425.

[18] Vojtech Petrucha and David Novotný. “Testing and application of an integrated fluxgate sensor DRV425”. In: *Journal of Electrical Engineering* 69 (Dec. 2018), pp. 418–421. DOI: 10.2478/jee-2018-0064.

[19] Martijn F. Snoeij et al. “Integrated Fluxgate Magnetometer for Use in Isolated Current Sensing”. In: *IEEE Journal of Solid-State Circuits* 51.7 (2016), pp. 1684–1694. DOI: 10.1109/JSSC.2016.2554147.

[20] Mahdi Kashmiri et al. “27.9 A 200kS/s 13.5b integrated-fluxgate differential-magnetic-to-digital converter with an oversampling compensation loop for contactless current sensing”. In: *2015 IEEE International Solid-State Circuits Conference - (ISSCC) Digest of Technical Papers*. 2015, pp. 1–3. DOI: 10.1109/ISSCC.2015.7063140.

[21] Martijn F. Snoeij et al. “Integrated Fluxgate Magnetometer for Use in Isolated Current Sensing”. In: *IEEE Journal of Solid-State Circuits* 51.7 (2016), pp. 1684–1694. DOI: 10.1109/JSSC.2016.2554147.

[22] Lei Guo et al. “Wide Linearity Range and Highly Sensitive MEMS-Based Micro-Fluxgate Sensor with Double-Layer Magnetic Core Made of Fe–Co–B Amorphous Alloy”. In: *Micromachines* 8.12 (2017). ISSN: 2072-666X. DOI: 10.3390/mi8120352. URL: https://www.mdpi.com/2072-666X/8/12/352.

[23] Lei Chong. “Improved performance of the micro planar double-axis fluxgate sensors with different magnetic core materials and structures”. In: *Microsystem Technologies* (July 2015).

[24] Jian Lei, Chong Lei, and Yong Zhou. "Analysis and comparison of the performance of MEMS fluxgate sensors with permalloy magnetic cores of different structures". In: *Measurement* 46.1 (2013), pp. 710–715. ISSN: 0263-2241. DOI: https://doi.org/10.1016/j.measurement.2012.09.009. URL: https://www.sciencedirect.com/science/article/pii/S0263224112003582.

[25] ANSYS, Inc. *Ansys Maxwell*. 2023. URL: https://www.ansys.com/products/electronics/ansys-maxwell (visited on 11/22/2023).

[26] F Primdahl et al. "The fluxgate ring-core internal field". In: *Measurement Science and Technology* 13.8 (July 2002), p. 1248. DOI: 10.1088/0957-0233/13/8/312. URL: https://dx.doi.org/10.1088/0957-0233/13/8/312.

[27] C. C. Finlay et al. "International Geomagnetic Reference Field: the eleventh generation". In: *Geophysical Journal International* 183.3 (2010), pp. 1216–1230. DOI: 10.1111/j.1365-246X.2010.04804.x.

[28] F. N. Fritsch and R. E. Carlson. "Monotone Piecewise Cubic Interpolation". In: *SIAM Journal on Numerical Analysis* 17 (1980), pp. 238–246.

[29] VACUUMSCHMELZE GMBH & Co. KG. *Soft Magnetic Materials and Semi-finished Products*. PHT-001. 2002.

[30] P. Ripka. *Magnetic sensors and magnetometers, second edition*. Norwood, MA: Artech House, 2021.

[31] *Resistance and Resistivity*. Accessed: 2023-11-07. HyperPhysics. URL: http://hyperphysics.phy-astr.gsu.edu/hbase/Tables/rstiv.html (visited on 11/07/2023).

# Abbreviations

| | |
|---|---|
| COB | Chip on board |
| CTU | Czech Technical University |
| DUT | Device under test |
| EDA | Electronic design automation |
| FEM | Finite element method |
| NTUST | National Taiwan University of Science and Technology |
| PCB | Printed circuit board |
| TSRI | Taiwan Semiconductor Research Institute |
| TSMC | Taiwan Semiconductor Manufacturing Company |
| UMC | United Microelectronics Corporation |

# Appendix A

## Raw Measurement Data of Material's B-H Curve

**Table A.1:** B-H Curve of VITROVAC 6025 F

| H [A/m] | B[T] | Used for interpolation |
|---|---|---|
| 0.000 | 0.000 | Yes |
| 7.742 | 0.080 | No |
| 15.541 | 0.163 | No |
| 22.780 | 0.247 | No |
| 30.217 | 0.326 | Yes |
| 37.900 | 0.394 | Yes |
| 45.785 | 0.455 | Yes |
| 64.802 | 0.526 | Yes |
| 84.735 | 0.575 | Yes |
| 102.066 | 0.585 | Yes |
| 118.944 | 0.591 | Yes |
| 135.319 | 0.596 | Yes |
| 151.749 | 0.599 | No |
| 167.981 | 0.602 | No |

# Appendix B

## List of Digital Attachments

1. Racetrack Core Demagnetization Factor
   - Ansys EM setup for simulating the demagnetization factor of a racetrack core
   - Python script for generating racetrack core dimensions for parametric simulation
   - MATLAB code for processing the results
2. BH Curve Measurement
   - Measurements of the BH-loop of the VITROVAC 6025 F core (Macro-sized racetrack)
   - MATLAB code for processing results and interpolating the curve for simulations
3. KiCAD Designs
   - Metal and bonding layout of micro-fluxgate version 1
   - Metal and bonding layout of micro-fluxgate version 2
4. Transient Simulation
   - Ansys EM setup for transient simulation of a fluxgate
     - Macro and Micro v1 (change core size in design parameters)
     - Micro v2
   - Raw results
5. Results Evaluation
   - Preprocessed measurement and simulation data in MATLAB (.mat) format
   - MATLAB code for processing the data
   - MATLAB code for pre-processing raw data
   - MATLAB code for processing coil temperature measurement
   - Raw measurement data (available only on CD, not online, due to large size)